

REPORT DOCUMENTATION PAGE			Form Approved OMB NO. 0704-0188		
<p>The public reporting burden for this collection of information is estimated to average 1 hour per response, including the time for reviewing instructions, searching existing data sources, gathering and maintaining the data needed, and completing and reviewing the collection of information. Send comments regarding this burden estimate or any other aspect of this collection of information, including suggestions for reducing this burden, to Washington Headquarters Services, Directorate for Information Operations and Reports, 1215 Jefferson Davis Highway, Suite 1204, Arlington VA, 22202-4302. Respondents should be aware that notwithstanding any other provision of law, no person shall be subject to any penalty for failing to comply with a collection of information if it does not display a currently valid OMB control number. PLEASE DO NOT RETURN YOUR FORM TO THE ABOVE ADDRESS.</p>					
1. REPORT DATE (DD-MM-YYYY) 03-12-2015		2. REPORT TYPE Final Report		3. DATES COVERED (From - To) 15-Sep-2010 - 30-Sep-2015	
4. TITLE AND SUBTITLE Final Report: Flowfield Characteristics on a Retreating Rotor Blade			5a. CONTRACT NUMBER W911NF-10-1-0398		
			5b. GRANT NUMBER		
			5c. PROGRAM ELEMENT NUMBER 611102		
6. AUTHORS Narayanan Komerath, Vrishank Raghav, Nandeesh Hiremath, Dhwanil Shukla			5d. PROJECT NUMBER		
			5e. TASK NUMBER		
			5f. WORK UNIT NUMBER		
7. PERFORMING ORGANIZATION NAMES AND ADDRESSES Georgia Tech Research Corporation 505 Tenth Street NW Atlanta, GA 30332 -0420			8. PERFORMING ORGANIZATION REPORT NUMBER		
9. SPONSORING/MONITORING AGENCY NAME(S) AND ADDRESS (ES) U.S. Army Research Office P.O. Box 12211 Research Triangle Park, NC 27709-2211			10. SPONSOR/MONITOR'S ACRONYM(S) ARO		
			11. SPONSOR/MONITOR'S REPORT NUMBER(S) 56045-EG.28		
12. DISTRIBUTION AVAILABILITY STATEMENT Approved for Public Release; Distribution Unlimited					
13. SUPPLEMENTARY NOTES The views, opinions and/or findings contained in this report are those of the author(s) and should not be construed as an official Department of the Army position, policy or decision, unless so designated by other documentation.					
14. ABSTRACT The aerodynamics of a rotor become uncertain when the rotor is in edgewise flight at advance ratios approaching unity. The retreating blade encounters reverse flow over significant portions of the span. Traditional approaches have attempted to make yaw corrections to 2-dimensional airfoil aerodynamics. This project used stereo particle image velocimetry on a 2-bladed rotor at advance ratios of 0.7, 0.85 and 1.0, focusing on rotor azimuths 240, 270 and 300 degrees. These complemented load measurements and tuft visualization on the same blade used as a fixed wing in forward and backward sweep in forward and reversed flow. SPIV was also used on the blade held fixed at					
15. SUBJECT TERMS Dynamic stall, Radial flow, Reverse Flow, Stereo PIV, Particle Image Velocimetry, Vortex, Sharp Edge, Flow Separation					
16. SECURITY CLASSIFICATION OF:		17. LIMITATION OF ABSTRACT	15. NUMBER OF PAGES	19a. NAME OF RESPONSIBLE PERSON	
a. REPORT	b. ABSTRACT			c. THIS PAGE	Narayanan Komerath
UU	UU	UU		19b. TELEPHONE NUMBER 404-894-3017	

Report Title

Final Report: Flowfield Characteristics on a Retreating Rotor Blade

ABSTRACT

The aerodynamics of a rotor become uncertain when the rotor is in edgewise flight at advance ratios approaching unity. The retreating blade encounters reverse flow over significant portions of the span. Traditional approaches have attempted to make yaw corrections to 2-dimensional airfoil aerodynamics. This project used stereo particle image velocimetry on a 2-bladed rotor at advance ratios of 0.7, 0.85 and 1.0, focusing on rotor azimuths 240, 270 and 300 degrees. These complemented load measurements and tuft visualization on the same blade used as a fixed wing in forward and backward sweep in forward and reversed flow. SPIV was also used on the blade held fixed at discrete yaw attitudes. The results vindicated a vortex flow model for reverse flow aerodynamics. Soon after 180 degrees azimuth, a strong vortex forms under the sharp edge of the blade, similar to that on the leeward side of a delta wing or strake at angle of attack. By 240 degrees the vortex is strong, similar to that on a forward-swept delta wing, with the highest dynamic pressure near the root. As the yaw decreases, the vortex bursts. By 270 degrees, the vortex is burst and detached. It convects with the blade, and is seen under the blade at 300 degrees. The pressure distribution under the blade is explained using vortex interactions. Three-dimensional separation over the blunt edge does not generate periodic shedding in these experiments. Extraction of static pressure from the velocity field is explored, and gives useful results.

Enter List of papers submitted or published that acknowledge ARO support from the start of the project to the date of this printing. List the papers, including journal references, in the following categories:

(a) Papers published in peer-reviewed journals (N/A for none)

Received

Paper

- 04/08/2015 23.00 Vrishank Raghav, Narayanan Komerath. Advance ratio effects on the flow structure and unsteadiness of the dynamic-stall vortex of a rotating blade in steady forward flight, *Physics of Fluids*, (02 2015): 0. doi: 10.1063/1.4906803
- 04/08/2015 22.00 M. Mayo, V. Raghav, N. Komerath. Vortex flow hypothesis for a yawed rotor blade in reverse flow, *Proceedings of the Institution of Mechanical Engineers, Part G: Journal of Aerospace Engineering*, (09 2014): 0. doi: 10.1177/0954410014537471
- 08/19/2014 15.00 Narayanan Komerath, Vrishank Raghav. Instability of the radial flow over a rotating disk in a separated edgewise stream, *Physics of Fluids*, (11 2013): 1. doi:
- 08/19/2014 16.00 V. Raghav, M. Mayo, R. Lozano, N. Komerath. Evidence of vortex-induced lift on a yawed wing in reverse flow, *Proceedings of the Institution of Mechanical Engineers, Part G: Journal of Aerospace Engineering*, (11 2013): 0. doi: 10.1177/0954410013511597
- 08/24/2013 5.00 Vrishank Raghav, Narayanan Komerath. Radial Flow on Rotor Blades in Dynamic Stall, *Journal of the American Helicopter Society*, (04 2013): 1. doi:

TOTAL: 5

Number of Papers published in peer-reviewed journals:

(b) Papers published in non-peer-reviewed journals (N/A for none)

Received Paper

TOTAL:

Number of Papers published in non peer-reviewed journals:

(c) Presentations

Number of Presentations: 0.00

Non Peer-Reviewed Conference Proceeding publications (other than abstracts):

Received Paper

04/08/2015 24.00 Dhwanil Shukla, Vrishank Raghav, Sorin Pirau, Nandeesh Hiremath, Narayanan Komerath. Effects of advance ratio and radial location on the vortex structure on a rotating blade in reverse flow, Proceedings of the American Helicopter Society 71st Annual Forum . 03-MAY-15, . . . ,

08/20/2014 18.00 Vrishank Raghav, Narayanan Komerath. Dynamic stall life cycle on a rotating blade in steady forward flight, Proceedings of the American Helicopter Society Forum. 22-MAY-14, . . . ,

08/24/2013 6.00 Vrishank Raghav, Narayanan Komerath. Investigation of Radial Flow on a Rotating Disk at Low Advance Ratios, AIAA Aerospace Sciences Meeting. 15-JAN-12, . . . ,

08/24/2013 7.00 Kevin Goal, Vrishank Raghav, Narayanan Komerath. Quantitative Measurements on Wall Formation by Particles in an Acoustic Resonator, AIAA Aerospace Sciences Meeting. 15-JAN-12, . . . ,

08/29/2011 2.00 Vrishank Raghav, Phillip Richards, Narayanan Komerath, Marilyn Smith. An Exploration of the Physics of Dynamic Stall, AHS Specialists' Meeting on AeromechanicsSan Francisco, CA. 31-JAN-10, . . . ,

TOTAL: **5**

Number of Non Peer-Reviewed Conference Proceeding publications (other than abstracts):

Peer-Reviewed Conference Proceeding publications (other than abstracts):

<u>Received</u>	<u>Paper</u>
04/08/2015 21.00	Michael Mayo, Vrishank Raghav, Natasha Barbely, Brandon Liberi , Narayanan Komerath. Flow Structure On A Retreating Rotor Blade At High Advance Ratios, IMECE2014-37593, Proceedings of ASME 2014 International Mechanical Engineering Congress & Exposition IMECE 2014, Montreal, Canada. 14-NOV-14, . . . ,
04/15/2015 26.00	Dhwanil Shukla, Nandeesh Hiremath, Vrishank Raghav, Narayanan Komerath. DYNAMIC EFFECTS IN THE REVERSE FLOW VELOCITY FIELD, Proceedings of the ASME-JSME-KSME Joint Fluids Engineering Conference 2015 AJK2015-FED, SEOUL, KOREA. 26-JUL-15, . . . ,
08/22/2015 27.00	Narayanan Komerath, Dhwanil Shukla, Nandeesh Hiremath. VORTICAL FEATURES OF A ROTOR BLADE IN REVERSED FLOW, IMECE 2015, International Mechanical Engineering Conference and Exposition, Houston, TX. 15-NOV-15, . . . ,
08/24/2013 8.00	Kevin Goal, Daniel Sun, Akshaya Srivastava, Narayanan Komerath. Dynamic Pitching Moment Measurement of a Wing Executing Pitch and Plunge Motion, AIAA 10th Annual International Energy Conversion Engineering Conference. 31-JUL-12, . . . ,
08/24/2013 12.00	Vrishank Raghav, Narayanan Komerath. Boundary Layer Measurements on a Rotating Disk, IMECE2013 ASME 2013 International Mechanical Engineering Congress & Exposition. 21-NOV-13, . . . ,
08/24/2013 11.00	Michael Mayo, Nicholas Motahari, Vrishank Raghav, Narayanan Komerath. Vortex Flow Hypothesis for Rotor Blades in Reverse Flow, IMECE2013 ASME 2013 International Mechanical Engineering Congress & Exposition. 21-NOV-13, . . . ,
08/24/2013 10.00	Natasha Barbely, Sorin Pirau, Narayanan Komerath. MEASUREMENTS OF WALL FORMATION FORCES IN AN ACOUSTIC RESONATOR, IMECE2013, ASME 2013 International Mechanical Engineering Congress & Exposition. 21-NOV-13, . . . ,
08/24/2013 9.00	Vrishank Raghav, Narayanan Komerath, Rafael Lozano. Aerodynamics of a Yawed Blade in Reverse Flow, IMECE 2012, ASME 2012 International Mechanical Engineering Congress & Exposition. 15-NOV-12, . . . ,
08/29/2011 4.00	Narayanan Komerath, Vrishank Raghav. Physics of Transient Stall on a Rotating Blade due to Blockage, Proceedings of the IMETI Conference, Orlando, FL. 19-JUL-11, . . . ,
TOTAL:	9

Number of Peer-Reviewed Conference Proceeding publications (other than abstracts):

(d) Manuscripts

<u>Received</u>	<u>Paper</u>
08/19/2014 14.00	Vrishank Raghav, Narayanan Komerath. An exploration of radial flow on a rotating blade in retreating blade stall , Journal of the American Helicopter Society (04 2013)
08/19/2014 17.00	Vrishank Raghav, Narayanan Komerath, Michael Mayo. Vortex flow hypothesis for a yawed rotorblade in reverse flow, Proc IMechE Part G: J AerospaceEngineering (05 2014)
08/20/2014 19.00	Narayanan Komerath, Vrishank Raghav. Advance ratio effects on the dynamic-stall vortex of a rotating blade in steadyforward ight, Physics of Fluids (08 2014)
08/20/2014 20.00	Vrishank Raghav, Narayanan Komerath. Dynamic-stall life cycle on a rotating blade in steady forward flight, Journal of the American Helicopter Society (04 2014)
08/24/2013 13.00	Vrishank Raghav, Michael Mayo, Rafael Lozano, Narayanan Komerath. Evidence of Vortex Induced Lift on a Yawed Wing in Reverse Flow, Journal of Aerospace Engineering (07 2013)

TOTAL: 5

Number of Manuscripts:

Books

Received Book

TOTAL:

Received

Book Chapter

TOTAL:

Patents Submitted

Patents Awarded

Awards

Vrishank Raghav, Georgia Tech Sigma Xi Outstanding PhD Thesis Award.

Vaibhav Kumar, Vertical Flight Foundation Undergraduate Fellowship, 2015.

Vaibhav Kumar, Georgia Tech President's Undergraduate Research Assistantship, 2015

Jackson Merkl, Georgia Tech President's Undergraduate Research Assistantship, 2015

Dhwanil Shukla, Vertical Flight Foundation Graduate Fellowship, 2015. Narayanan M. Komerath, AIAA/ASEE 2015 John Leland Atwood Award

Graduate Students

<u>NAME</u>	<u>PERCENT SUPPORTED</u>	Discipline
Vrishank Raghav	0.50	
Nandeesh Hiremath	0.50	
Dhwanil Shukla	0.50	
FTE Equivalent:	1.50	
Total Number:	3	

Names of Post Doctorates

<u>NAME</u>	<u>PERCENT SUPPORTED</u>
FTE Equivalent:	
Total Number:	

Names of Faculty Supported

<u>NAME</u>	<u>PERCENT SUPPORTED</u>	National Academy Member
Narayanan M. Komerath	0.08	
FTE Equivalent:	0.08	
Total Number:	1	

Names of Under Graduate students supported

<u>NAME</u>	<u>PERCENT SUPPORTED</u>	Discipline
Brandon Liberi	0.00	
Jackson Merkl	0.00	
Vaibhav Kumar	0.00	
Nicholas Motahari	0.00	
Ryan McMullen	0.00	
FTE Equivalent:	0.00	
Total Number:	5	

Student Metrics

This section only applies to graduating undergraduates supported by this agreement in this reporting period

The number of undergraduates funded by this agreement who graduated during this period: 4.00

The number of undergraduates funded by this agreement who graduated during this period with a degree in science, mathematics, engineering, or technology fields:..... 4.00

The number of undergraduates funded by your agreement who graduated during this period and will continue to pursue a graduate or Ph.D. degree in science, mathematics, engineering, or technology fields:..... 3.00

Number of graduating undergraduates who achieved a 3.5 GPA to 4.0 (4.0 max scale):..... 2.00

Number of graduating undergraduates funded by a DoD funded Center of Excellence grant for Education, Research and Engineering:..... 0.00

The number of undergraduates funded by your agreement who graduated during this period and intend to work for the Department of Defense 1.00

The number of undergraduates funded by your agreement who graduated during this period and will receive scholarships or fellowships for further studies in science, mathematics, engineering or technology fields:..... 2.00

Names of Personnel receiving masters degrees

<u>NAME</u>	
Nandeesh Hiremath	
Michael Mayo	
Rafael Lozano	
Total Number:	3

Names of personnel receiving PHDs

<u>NAME</u>	
Vrishank Raghav ShankarGowda	
Total Number:	1

Names of other research staff

<u>NAME</u>	<u>PERCENT SUPPORTED</u>
FTE Equivalent:	
Total Number:	

Sub Contractors (DD882)

Inventions (DD882)

Scientific Progress

Please See Attachment

Technology Transfer

GITEACG-ADLR-2015123001

FLOWFIELD CHARACTERISTICS ON A RETREATING ROTOR BLADE

Narayanan M. Komerath, Vrishank S. Raghav, Nandeesh Hiremath, Dhwanil Shukla
Daniel Guggenheim School of Aerospace Engineering
Georgia Institute of Technology, Atlanta, GA 30332-0150
Performing Organization: Georgia Tech Research Corporation

December 3, 2015

Disclaimer

The contents of this report are not to be construed as the opinions or official positions of the United States Government or its agencies.

Acknowledgments

The experiments reported in this report were performed at the John J. Harper Low Speed Wind Tunnel at the School of Aerospace Engineering, Georgia Institute of Technology. The work was funded initially as part of an exploration on radial flow effects on retreating rotor blades, monitored by Dr. Frederick Ferguson. This was then supplemented with a 1-year extension focused on reverse flow, monitored by Dr. Bryan Glaz, and then by Dr. Matthew Munson.

Contents

1	Introduction and Synopsis	1
1.1	Project History	1
1.2	Introduction to Reverse Flow	2
1.3	Prior Work on Reverse Flow	4
1.4	Vortex Flow Model for Reverse Blade Aerodynamics	8
1.5	Evolution of the Vortex Flow Model	10
2	Experimental Methods	18
2.1	Wind Tunnel	18
2.2	Instrumentation and data processing	19
2.3	Stereoscopic-PIV instrumentation	20
2.4	Accuracy estimates	21
2.5	Tip Path Plane (TPP) and Blade Vertical Motion	23
3	Fixed Wing Results	25
3.1	Polhamus suction analogy for yawed rotor blade	26
3.2	Flow and test conditions	26
3.3	Error analysis	28
3.4	Aerodynamic loads	28
3.4.1	Lift	28
3.4.2	Predictions using Polhamus suction analogy	30

3.4.3	Drag and pitching moment	30
3.5	Surface flow visualization	32
3.5.1	Forward yaw $Re = 1.7 \times 10^5$	33
3.5.2	Backward yaw $Re = 1.7 \times 10^5$	36
3.5.3	$Re = 3.0 \times 10^5$ and $\alpha = 195^\circ$	36
3.5.4	Flow topology	36
3.6	Yawed Rotor Blade Held Stationary	41
3.6.1	Instrumentation	41
3.6.2	Flow and Test Conditions	43
3.6.3	Data Acquisition/Processing	44
3.6.4	Averages flow field results	44
3.7	Exploratory Measurements Under the Rotating Blade	46
3.7.1	Implications	49
4	Rotor Blade Results	60
4.1	Averaged flow field data	60
4.1.1	Azimuth 240 deg.	61
4.1.2	Azimuth 300 degrees	63
4.2	Pressure Coefficient Contours	64
4.3	Interpretation of Results	64
4.4	Surface Pressure Contours	67
4.5	Vortex core profile	68
4.6	Blunt Edge Flowfield	68
4.7	Aspect Ratio Effects	69
5	Conclusions	80

List of Figures

1.1	Variation of the extent of the reverse flow region on the retreating blade, with advance ratio μ	3
1.2	Hypotheses considered for explaining reverse flow aerodynamics: the bottom one is our vortex-flow hypothesis	5
1.3	Rotor blade used in fixed-wing mode	11
1.4	Test section as viewed from upstream, showing stereo PIV system looking at bottom of the retreating blade	12
1.5	Schematic of top-view of the rotor disk (not to scale), for stereo PIV .	13
1.6	Lift curve slopes in forward and reverse sweep for a blade held as a fixed wing. From [1]	14
1.7	Movement of center of pressure on a fixed wing in reverse flow, with yaw and angle of attack, at chord Reynolds number of 300K. From [1]	15
1.8	Surface tuft behavior shows clear evidence of a vortex and vortex bursting on a wing in reverse flow at 45 degree forward yaw and 15 degrees angle of attack. From [1]	16
1.9	Sharp-edge vortex captured using stereo PIV at r/R of 0.5 under a rotating blade at 240 deg. azimuth, for several advance ratios. From [2]	16
1.10	A simplified artist's conception of the SEV at 240 degrees, as it might be for a blade of larger aspect ratio. Note that the vortex starts at about r/R of 0.7, and grows inward. The dynamic pressure of the relative flow is highest near the root, but the vortex may also burst near the root because of the obstruction due to the hub.	17

2.1	Side view of the rotor setup in the wind tunnel, where x_b and z_b are blade fixed coordinates)	20
2.2	Measurement Regions	22
2.3	Blade vertical speeds in m/s for different advance ratios in the reverse flow regime	24
3.1	Lift curve slopes at various Ψ and Re (Ψ negative for backward yaw)	29
3.2	Lift predictions using the Polhamus model for a yawed blade in reverse flow	31
3.3	Drag and pitching moment data for regular and reverse flow cases	32
3.4	Variation of chordwise center of pressure location with α at various Ψ	33
3.5	Tuft visualization at $Re = 1.7 \times 10^5$	34
3.6	Tuft visualization at $Re = 3.0 \times 10^5$ and $\alpha = 195^\circ$	37
3.7	Proposed Flow Topologies for a Rotor Blade in Reverse Flow	38
3.8	Proportion of blade area occupied by the different flow regimes as a function of angle of attack at $Re = 1.7 \times 10^5$	40
3.9	Topology of vortex flow over a fixed wing in reverse flow, with forward and reverse sweep. From Raghav et al. [3]	42
3.10	Photo of the Stereo PIV setup	51
3.11	Test section as viewed from upstream	52
3.12	Static Blade at $\Psi = 30^\circ$, $\alpha = 191.2^\circ$, $Re = 0.63 \times 10^5$	52
3.13	Static Blade at $\Psi = 30^\circ$, $\alpha = 191.2^\circ$, $Re = 0.63 \times 10^5$	53
3.14	Static Blade at $\Psi = 30^\circ$, $\alpha = 195^\circ$, $Re = 1.70 \times 10^5$	53
3.15	Radial flow on static blade at $\Psi = 30^\circ$, $\alpha = 192^\circ$, $Re = 0.63 \times 10^5$	54
3.16	Radial flow under rotating blade at $\mu = 0.8$, yaw=240, $r/R=0.5$	54
3.17	Vorticity Contours Under Rotating Blade At $\Psi = 240^\circ$, $\mu = 0.8$, and $\Omega = 20.93rad/s$ which yields $\alpha = 192^\circ$ and $Re = 0.63 \times 10^5$ at $r/R = 0.5$	55
3.18	Vorticity Contours Under Rotating Blade At $\Psi = 270^\circ$, $\mu = 0.8$, and $\Omega = 20.93rad/s$ which yields $\alpha = 196^\circ$ and $Re = 0.635 \times 10^5$ at $r/R = 0.5$	55
3.19	Yaw = 240, $r/R = 0.5$, $\mu = 0.6$, Local Reynolds No. = 1.14×10^5	56

3.20	Yaw = 240, $r/R = 0.5$, $\mu = 0.8$, Local Reynolds No. = $1.52 * 10^5$, Observed approximate circulation at vortex = $0.75m^2/s$	57
3.21	Yaw = 240, $r/R = 0.5$, $\mu = 1.0$, Local Reynolds No. = $1.89 * 10^5$, Observed approximate circulation at vortex = $1.44m^2/s$	58
3.22	Radial variation of velocity field at a fixed advance ratio of 0.85, at 240 degrees azimuth	59
4.1	Streamline plots from SPIV near the sharp edge of the blade at different r/R at $\psi = 240$ and $\mu = 0.85$	61
4.2	Streamline plots at r/R of 0.6 at $\psi = 240$ and $\mu = 0.85$	62
4.3	Streamline plots from SPIV near the sharp edge of the blade at different r/R at $\psi = 270$ and $\mu = 0.85$	63
4.4	Streamline plots at r/R of 0.6 at $\psi = 270$ and $\mu = 0.85$	70
4.5	Streamline plots from SPIV near the sharp edge of the blade at different r/R at $\psi = 300$ and $\mu = 0.85$	71
4.6	Streamline plots at r/R of 0.6 at $\psi = 300$ and $\mu = 0.85$	72
4.7	Contours of static pressure coefficient in the flow field generated from the SPIV data by assuming constant stagnation pressure. Azimuth 240, $r/R=0.5$, $t=0.85$	73
4.8	Contours of static pressure coefficient on the blade generated from the SPIV data by assuming constant stagnation pressure. Azimuth 270, $t=0.85$	73
4.9	Viscous shear stress coefficient along a streamline through the sharp- edge vortex, as a measure of the loss in stagnation pressure.	74
4.10	Various models for reversed flow on rotor blades.	74
4.11	Static pressure contours obtained from the interpolated velocity field, at $\psi = 240$ for different advance ratios	75
4.12	Static pressure contours obtained from the interpolated velocity field, at $\psi = 270$ for different advance ratios	76
4.13	Static pressure contours obtained from the interpolated velocity field, at $\psi = 300$ for different advance ratios	77
4.14	Velocity profile across the vortex at Azimuth 270	78

4.15 Flow Behavior Around the Blunt Edge. Qualitative pictures from initial SPIV data	78
4.16 Streaklines and radial velocity contours at the Blunt Edge, for $r/R=0.4$, at $\mu = 0.7$ at 240 and 270 deg.	79

List of Tables

2.1	High advance ratio facility rotor specifications	19
2.2	Test matrix for experiments	21
2.3	Summary of velocity uncertainty estimates	21
2.4	Blade Motion Amplitude and Phase	23
3.1	Test matrix for experiments	27
3.2	Summary of errors	28
3.3	Rotor Parameters	43
3.4	Test Matrix For Experiments	44

Summary

The nature of the flow around a rotating blade in reverse flow is described, integrating results from fixed and rotating wing experiments. The highly 3-dimensional flow phenomena do not conform to expectations based on 2-dimensional airfoil aerodynamics. The same NACA0013 blade was used both as a fixed wing, and then as a rotor blade in a low-speed wind tunnel. Fixed-wing results from load measurements and flow visualization showed that the sharp-edge vortex (SEV) is a primary feature when the blade is yawed either forward or backward in reverse flow. The aerodynamic loads are better modeled using the Polhamus leading edge suction analogy, with vortex-induced lift and pitching moment making significant contributions. Surface tuft visualization on the blade operated as a fixed wing, strengthened the evidence for such vortices, including their bursting where they encountered adverse pressure gradient near the blade root. Particle image velocimetry was performed in the wind tunnel with the blade held at discrete settings of yaw and pitch corresponding to expected rotor blade positions. The presence of a strong SEV was confirmed by velocity field data. The blade was next operated as one of 2 blades of a teetering rotor, and stereo Particle Image Velocimetry data were acquired at azimuths 240 (forward yaw), 270 (zero yaw) and 300 (backward yaw) degrees. At 240 degrees, the vortex-induced pressure gradient induces an inward radial flow overcoming centrifugal effects, but away from the vortex, outward radial flow was evident. A strongly three-dimensional and attached SEV is evident under the blade at 240 degrees azimuth. This detaches and convects with the flow, remaining close to the blade by 270 degrees. The vortex seen at 300 degrees is clearly detached, but growth of the core diameter corresponding to vortex bursting, causes strong suction under the blade. The flow around the blunt edge is again strongly 3-dimensional, so that the expectation of 2-D flow separation was debunked. Some evidence of intermittent separation is seen, but the azimuth-resolved, ensemble-averaged flow is mostly attached around the blunt edge. Preliminary static pressure contours were derived from the measured 3-component velocity field using a simple Bernoulli equation conversion in this incompressible flow, with the effect of

unsteady pitch and plunge being minor. These pressure data enabled interpretation of the surface pressure field, and the relative roles of vortex-induced suction and radial stress. In summary, it is apparent that the reverse flow regime should be modeled and analyzed as a case of SEV formation under the very sharply swept blade immediately after 180 degrees azimuth. The SEV evolves as the sweep decreases with azimuth increasing. In the regime before 240 degrees, an attached, strengthening SEV may be expected. At some moderate sweep (azimuth beyond 240 degrees in our case) the vortex bursts and detaches from the surface. Thereafter it convects with the blade, but induces strong pressure effects on the blade surface even as far as 300 degrees azimuth. The blunt edge flow is highly 3-dimensional, and has much less flow separation and unsteadiness than might be predicted from 2-dimensional airfoil aerodynamics.

Nomenclature

b	span of the blade, m
c	chord of the blade, m
k	reduced frequency
R	blade tip radius, m
Re	chord Reynolds number
r	radial location, m
U_∞	freestream velocity, m/s
U_e	effective velocity, m/s
U_r	radial velocity, m/s
U_T	blade tip speed, m/s
u	velocity in x direction, m/s
v	velocity in y direction, m/s
w	velocity in z direction, m/s
x	chordwise, referred to the blade, m
y	vertical, referred to the blade, m
z	radial, referred to the blade, m
Γ	circulation, m^2/s
μ	advance ratio
Ω	rotor angular velocity, rad/s
ω	vorticity, $1/s$
ψ	azimuthal angle, deg

Chapter 1

Introduction and Synopsis

1.1 Project History

The retreating side of a helicopter rotor in forward flight poses several performance-limiting phenomena. The most famous of these is the dynamic stall problem. In order to balance the rolling moments between the two sides of the rotor, the blade pitch is increased as the blade moves through the retreating part of the disc. This results in substantial portions of the blade experiencing stall. Where the pitch rate is high, the blade retains dynamic lift well past the static stall angle of attack, and then experiences dynamic stall, with sharp excursions in pitching moment. The precise timing of the different phases of dynamic stall have proven to be challenging to predict. Some of the difficulties stem from the fact that rotor dynamic stall is far from being a 2-dimensional phenomenon. Hence experiments and computations with non-rotating pitching, plunging blades miss some significant physical phenomena that are of importance in the rotating case. Rotation causes several effects. One is the obvious variation of the onset velocity from root to tip. The second is the occurrence of strong radial flow along the blade surface.

This project started with a study of the radial flow on rotor blades in dynamic stall. From basic expectations, radial flow should have very strong effects on blade lift according to the expectation of monotonically increasing radial stress. In fact it does not have such strong visible effects. This was the central mystery, and the challenges in its resolution included those of capturing the velocity field in the dynamic stall flowfield. We showed that the radial jet layer immediately above the surface in the stalled regime, breaks up into discrete vortical shear layer structures with some

consistent frequency. A similar phenomenon occurs in the canonical problem of flow induced over a spinning disk, when the disk has edgewise flow at an angle of attack superposed. From such studies, the frequency and strength of the discrete structures could in principle be predicted, and this could in turn bring closure to the 3-D dynamic stall problem. We also performed stereo Particle Image Velocimetry (SPIV) capture of the 3-component, phase-resolved, ensemble-averaged (meaning the periodic component of the) velocity field of the 2-bladed NACA0013 teetering rotor in dynamic stall, from inception of stall through reattachment, at several radial stations. This is an extensive and unprecedented knowledge base. Our project on this problem was completed with the doctoral thesis of Vrishank Raghav [4] in 2014. Beyond that work, the rotor used in the dynamic stall work was operated under conditions where reverse flow occurred. In this problem the interesting phenomena are under the blade. This report focuses on the reverse flow problem. This chapter is used both as an Introduction and as a Synopsis, summarizing the significant results from both the dynamic stall radial flow, and the reverse flow studies. The rest of this report goes into detail on the reverse flow experiments.

1.2 Introduction to Reverse Flow

Where the advance ratio (μ , the ratio of flight speed to rotor tip speed) begins to approach unity, reversed flow occurs on large portions of the retreating blade of a rotor disc in edgewise flight, as shown in Figure 1.1. This can occur on helicopter rotors at high flight speed, the slowed rotor of an autogiro or compound helicopter, and on a wind turbine encountering a gust from the side. The aerodynamics of the blade in the reversed-flow regime pose several uncertainties. For instance, the center of pressure shifts suddenly from around the 25% to 75% of the chord as measured from the leading edge on the inboard parts of the blade span that first experience reverse flow, while remaining near 0.25% on the outboard parts. The lift direction switches from up to down on the reversed flow part. These induce both a quasi-steady change in bending and twisting moments on the blade, and vibratory loads as this happens through part of every rotor revolution. These loads may drive rotors into instability. High and fluctuating drag is expected because of the separation around the blunt edge of the blade. With the advent of rotorcraft employing counter-rotating, co-axial rotors, operation in the reverse flow regime is becoming increasingly common.

This report integrates results from an experimental study of the flowfield and aerodynamics of rotor blades in reverse flow. As summarized in Figure 1.2, prior approaches to reverse flow were from a two-dimensional airfoil / high aspect ratio wing viewpoint,

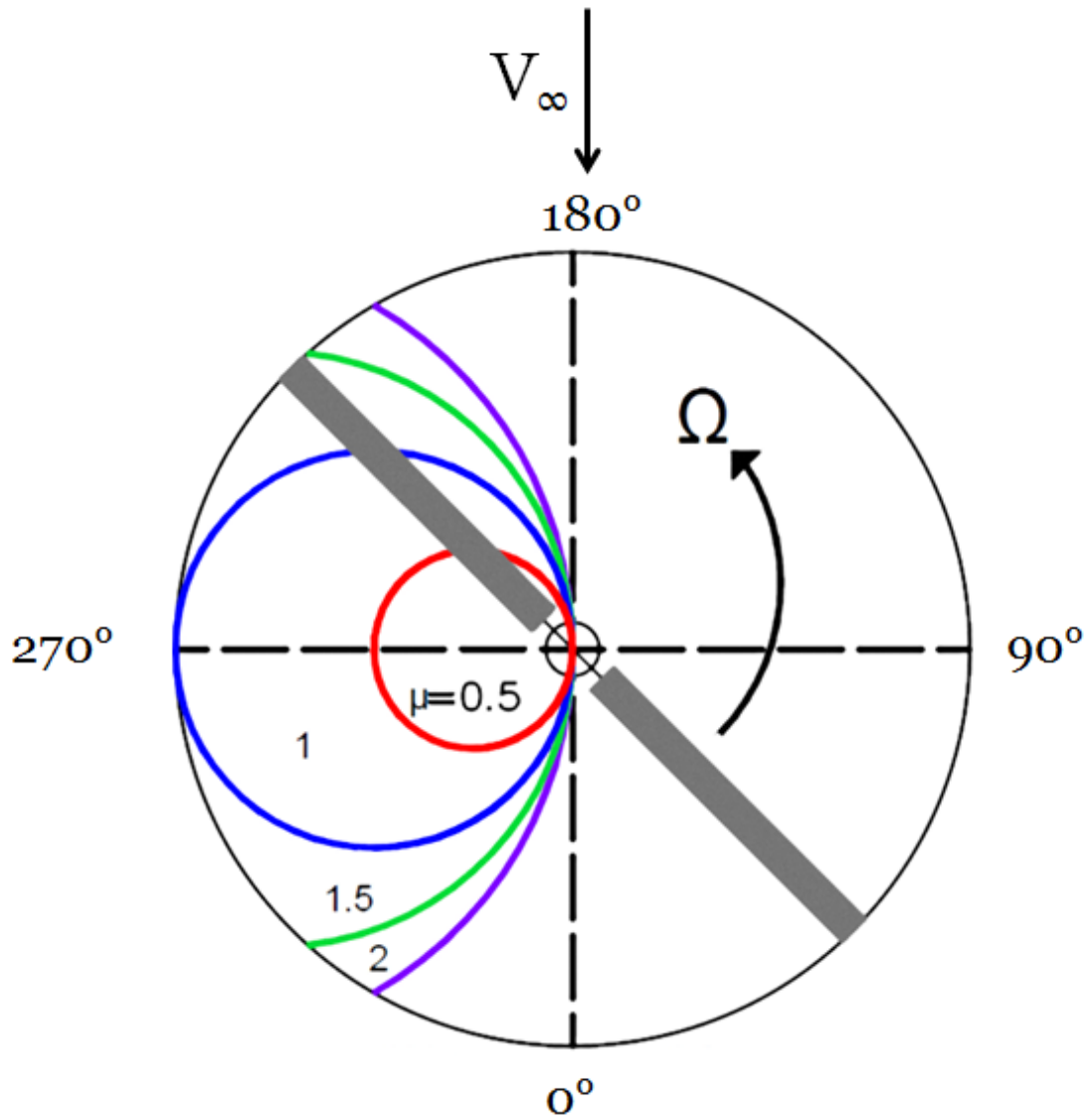


Figure 1.1: Variation of the extent of the reverse flow region on the retreating blade, with advance ratio μ

applying yaw and aspect ratio corrections to 2D airfoil data. Such models predict that the region below the blade features a dead 2-D recirculation zone, and the blunt base has massive separation with vortex shedding. Even when sweep corrections are applied, history effects are not captured. We argued that the formation and evolution of a strong 3-dimensional (helical) vortex early on the retreating blade side, would be key to the entire problem. At azimuths well before 240 degrees, the sharp edge of the blade resembles the edge of a highly forward-swept wing, causing a strongly helical vortex to form, with significant axial flow in its core. As azimuth increases the yaw decreases, and the subsequent evolution of the vortex bears much similarity to the observed phenomena on delta wings. We explored this hypothesis that the genesis of the aerodynamic loads was best viewed through the perspective of vortex flows occurring on sharp-edged swept wings at angle of attack. A rectangular untwisted NACA0013 rotor blade of (semi-span) aspect ratio 3.47 was used as a fixed wing in a wind tunnel, operated through a large variation in yaw and smaller variations in angle of attack, in both the forward and reverse-facing orientations. With the root cutout included during operation as a rotor blade, this corresponds to an aspect ratio beyond 8 in airplane wing terms. The phenomena in reverse flow are dominated by the sharp-edge vortex which is generated along the sharp edge of the blade. This vortex is three-dimensional with high values of axial velocity. It originates at the tip in the case of the forward quadrant, and at the root in the aft quadrant of the rotor. This flowfield does not conform to 2-D airfoil aerodynamics, nor to the high-aspect-ratio 'corrections' derived from Prandtl's lifting line theory approximations, even for a full-scale rotor blade. The experiment here aims to reveal the detailed flow phenomena, as opposed to producing scale-model results. The rotor radius of 2.13m was limited by the 2.74m width and 2.13m height of the wind tunnel where the rotor is operated. The larger chord enables the Reynolds number based on chord to go well above the laminar regime. It enables better resolution in capturing the velocity and eventually the pressure distributions on the blade.

1.3 Prior Work on Reverse Flow

The advance ratios experienced by the rotor blades of modern helicopters such as the Sikorsky X2 and Eurocopter X³ can exceed 0.8 [5, 6]. Here, advance ratio is defined as the ratio of forward flight speed to the rotational tip speed of the rotor. At these high advance ratios, significant sections of the retreating blade experience reverse flow, characterized by the freestream hitting the geometric trailing edge of the blade first and traveling toward the geometric leading edge. The resultant flow field is not well

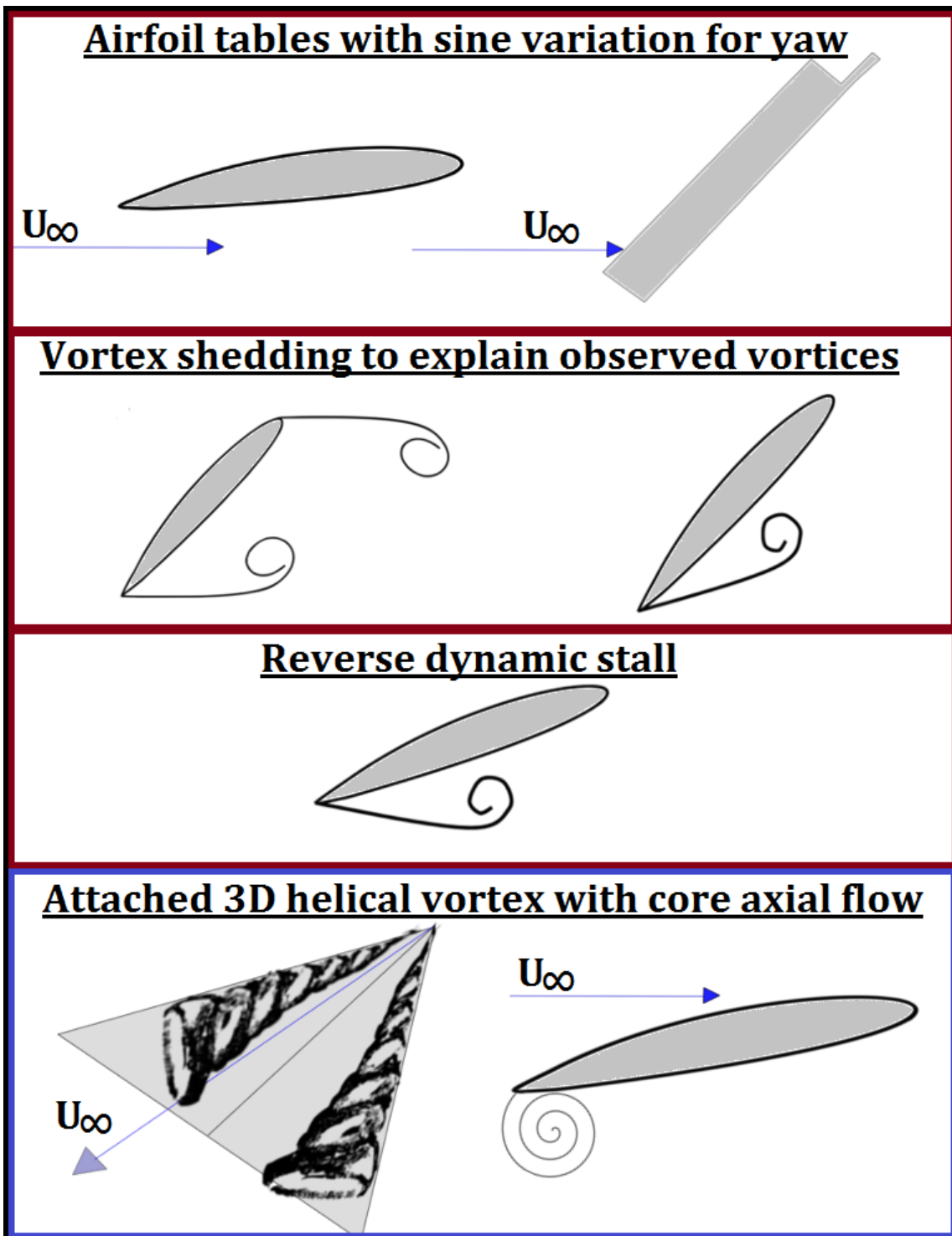


Figure 1.2: Hypotheses considered for explaining reverse flow aerodynamics: the bottom one is our vortex-flow hypothesis

understood and is characterized by early flow separation, negative lift, and periodic vortex shedding [7]. Reverse flow is a major limiter in the design of high-speed rotorcraft. Helicopter designs that attempt to mitigate the effects of reverse flow date back to the early 1970's. Fairchild Republic Division's [8] Reverse Velocity Rotor concept featured a negative pitch angle on the retreating blade in order to achieve a positive angle of attack in the reverse flow regime and airfoils with blunt leading and trailing edges. The more recent Sikorsky X2 Technology Demonstrator [9] has coaxial rotors based on the Advancing Blade Concept [10] platform and also features blunt trailing edge airfoil sections near the blade root.

As rotor advance ratio rises, the region of reverse flow on the rotor disk expands, reaching the blade tip at 270° azimuth at an advance ratio $\mu \sim 1$. Prior work has been surveyed in [2] and is summarized here by permission of the authors (we). The most basic method was to take airfoil data [7, 11–14] from 2D wind tunnel tests in the region around 180 degrees angle of attack, and correct for yaw with a sinusoidal correction, and if needed an aspect ratio correction. At the next level, with experiments revealing evidence of vortices in the flowfield, 'vortex shedding' was postulated; both from the blunt edge when using NACA0012 type airfoils with blunt leading edges, and from the sharp edge as from a thin flat plate held at negative angle of attack [7]. Karman vortex street analogues were also developed. These models have recently been adapted to include unsteady pitching effects, again from airfoil experimental data. Other studies with unswept airfoils have modeled the sharp-edge flow as a diffused, separated shear layer, with the blunt edge shedding vortices. Others have postulated a 'reverse-chord dynamic stall' process [6], explaining the occurrence of sharp pitching moments as well as strong vortices seen in the flowfield in experiments.

Wheatley et al. [15] performed force measurements on a Pitcairn PCA-2 autogyro rotor at various pitch settings and advance ratios up to $\mu = 0.7$ and found a negative correlation between lift coefficient and advance ratio. Charles et al. [16] tested a UH-1D rotor at advance ratios up to $\mu = 1.1$ and found that rotor performance predictions broke down at $\mu > 0.5$. They also observed flapping instability and a long transient response to control input at $\mu = 1.1$. MacCloud et al. [17] performed tests on a teetering rotor with a NACA 0012 airfoil at advance ratios up to 1.0 and observed a drop in lift coefficient at high advance ratios. Harris et al. [18] performed correlations studies on these early datasets in 2008 and concluded that OVERFLOW-2 could not accurately predict lift, drag and pitching moments for reverse airfoils and could not be recommended for use at an advance ratio beyond 0.35. Recent work includes [18–24]. The survey by Quackenbush [19], though intended for computations, captures many of the phenomena to be expected from the geometry, and even shows

a sharp-edged vortex. Harris [18] summarizes high advance ratio rotorcraft flight experience. Niemiec [23] and Carter [24] describe airfoils intended for the reversed-flow regime. Uncertainties in lift, drag, pitching moment, blade bending and twist, and rotor stability are cited in [25, 26]. Slowed compound rotorcraft with other lifting surfaces are reported in [8, 15–17, 27–33], and modern designs in [5, 34].

A recent study on a slowed UH-60A rotor performed by Datta et al. [6] showed evidence of reverse chord dynamic stall and large pitch-link load impulses on the retreating side of the rotor disc at advance ratios near unity. Kottapali [35] made initial attempts to predict the blade loads from this study using CAMRAD II, but they showed serious issues at $\mu > 0.8$. Predictions made by Yeo [36] using CAMRAD II showed fair airload and structural load correlation. Potsdam et al. [20] performed coupled CFD and comprehensive analysis on this dataset and predicted unconventional wake patterns and a lower surface vortex on the retreating blade, attributing that to dynamic stall. Pitching moment predictions on the advancing and retreating sides were not encouraging. Lee *et al* performed time-averaged force measurements and flow visualization on various airfoil sections in reverse flow and found a drag jump at $\alpha = 180^\circ$ due to the unsteady formation and convection of a large vortex in the wake. Lind et al. [7] also conducted reverse flow studies on static sharp and blunt trailing edge airfoils. They found that the large, negative angles of attack of the inboard section of a rotor in reverse flow causes flow separation and the onset of vortex shedding. It was suggested that the use of a blunt-trailing edge airfoil with a relatively linear lift curve slope would be ideal for the reverse flow regime. However, Lind et al. did not study the reverse flow aerodynamics of static yawed airfoils or finite wings.

In summary, the past approaches to the rotor reverse flow problem, have focused, as in the case of dynamic stall decades earlier, on the 2-D airfoil model. The 270-degree point is taken as the starting point for analyses, where the blade has no yaw. To explain the vortical structures reported by experimenters, computational researchers have focused on pitching and plunging airfoils, even venturing into 'reverse dynamic stall'. The presumption appears to have been that the rest of the retreating blade sector can be analyzed as perturbations of the 270-degree case, with yaw corrections applied.

1.4 Vortex Flow Model for Reverse Blade Aerodynamics

We suggested that approaches derived from airfoil aerodynamics were not at all appropriate for reverse flow, even less than for dynamic stall. Our view of reverse flow starts when the rotor blade is just past 180 degrees azimuth. The sharp trailing edge of the blade is now like a highly-swept strake or wing leading edge at (negative) angle of attack. It generates a strong, tight vortex. The rest of the retreating blade sector sees this vortex evolving in various ways, as discussed below. This hypothesis was first presented by Michael Mayo, then a first-year MS student, at the first round of the Lichten Competition in January 2013 at Georgia Tech. He encountered a hostile environment. In the year following that, Michael Mayo and his team at our laboratory pursued the vortex flow hypothesis. This model has now been clearly proven, and explains all observed phenomena. In contrast, models based on 2-D aerodynamics fail to predict even the situation at 270 degrees.

Our hypothesis of sharp-edge vortex flow is shown at the bottom of Figure 1.2. We postulated that the flow around and under a sharp, yawed edge behaves similarly to that around and over a sharp-edge delta wing or other highly swept wing at angle of attack. A strong, coherent, helical sharp-edged vortex is formed. Where this encounters an adverse pressure gradient, as near a hub, it can 'burst' and lift away from the surface. The vortex-induced lift and pitching moment can be computed using Polhamus' suction analogy [37,38], as well as nonlinear models for vortex flows at higher angles of attack.

A digression into 3-dimensional aerodynamics is appropriate here. The aerodynamics of a general lifting surface [39] can be represented in a potential flow analysis. The potential flowfield is a solution to the Laplace equation, a statement of mass conservation. The velocity field at any point is the superposition of the velocities 'induced' by each of the 'singularities' used to represent the lifting surface, such as sources, sinks, doublets or vortex loops whose individual flowfields are each a solution of the Laplace equation. In unsteady flow, vorticity in the wake is also represented. The strength of each "singularity" is found from the condition of zero normal velocity or the kinematic velocity of the surface. The solution of the set of equations representing the surface points has two important regimes of simplification: high aspect ratio (Prandtl's Lifting Line) and very low aspect ratio (slender wing theory). Prandtl's lifting line approach realizes that gradients of flow properties along the chord of a high-aspect ratio wing are much greater than those along the span. This is used to approximate chordwise variation by a vortex. The spanwise

variation of strength of this 'bound vortex' is accompanied by streaming vorticity whose 'strength' is the negative of the gradient of the vortex strength of the lifting line. This leads to a model of a high-aspect ratio wing as a lifting line (bound vortex), strong tip vortices, and an inboard vortex sheet. The bound vorticity strength at any spanwise section is related to 2D airfoil aerodynamics.

At the other extreme is Slender Wing Theory for thin triangular wings of extremely small aspect ratio. Spatial derivatives along the freestream direction are much less than those across the freestream. The domain of influence affecting properties at a given cross-section, is limited to local conditions and those upstream: downstream influence is negligible. The resulting pressure distribution has a sharp negative peak along the high-swept leading edges of the wing. R.T. Jones [40] developed an analogue between the aerodynamics of a given cross-section of a slender wing at angle of attack in steady flow, and an airfoil executing plunge motion in still fluid. The 'non-circulatory lift' experienced by the latter is equated to the rate of change of momentum of the 'apparent mass' of a cylinder of fluid of diameter equal to the chord, and unit length along the span. For a triangular wing (meaning swept leading edge) this rate of change of momentum arises for an uncambered wing in steady flow, from the sweep. With this formulation, the pressure distribution over the leeward surface of a slender wing may be calculated from potential flow. As angle of attack increases and sweep decreases, the pressure distribution deviates from the ideal slender wing prediction and evolves into that for a leading edge vortex above a swept edge.

Polhamus' suction analogy [38] is that the suction on the leeward side of a swept wing at angle of attack corresponds to the rate of change of momentum of the flow which is forced to curl around the edge and stay attached. The dependence on local properties is consistent with the slender-wing approximation to general lifting surface theory starting with the assumption that chordwise derivatives on a slender wing would be much lower than spanwise derivatives. This approximation also leads to R.T. Jones' slender wing theory, from where the spanwise load distribution, and the distribution of pressure coefficient can be derived. The C_p distribution has a sharp negative peak near the sharp edge. At α , or at lower sweep for the same α , the peak moves away from the edge as the attached flow is replaced by first an attached vortex and then a detached vortex. Thus our recommended approach will transition from Polhamus' analogy to slender wing theory and then to its modified form where there is first an attached and then a detached vortex.

For a delta wing at a given angle of attack, as wing sweep decreases, the vortex gets weaker (core expands). Burst and liftoff (detachment) occur faster. As the retreating rotor blade moves from 181 deg. (sharp edge at the highest forward sweep of 89 deg.

into the 240 deg. (sweep of 50 deg.) regime, the SEV is well formed and attached in the reverse flow zone. As the blade moves towards 270 deg., surely the sweep angle becomes too low to sustain an attached SEV, so there is detachment, and as we will see, bursting. The burst, detached vortex, however, convects with the mean flow, so that at high advance ratios near 1, *the vortex remains close to the blade despite being detached*. The presence of this vortex all the way to 300 degrees appears to inhibit formation of a new backward-sweep vortex, though one may form at azimuths higher than 300 deg., after the vortex has convected away from the blade.

1.5 Evolution of the Vortex Flow Model

Our wind tunnel experiments [1, 41, 42] have proceeded from fixed-wing airloads (Figure 1.3) and tuft visualization, to Particle Image Velocimetry (PIV) under a blade held fixed as part of a rotor in a wind tunnel [43], and then to stereo PIV with the rotor at high μ , as shown in Figure 1.4 and 1.5. These showed the presence and dominant role of the sharp-edge vortex. Mayo et al. [1] used the Polhamus suction analogy [37, 38] and the measured lift curve slopes (Figure 1.6) to predict lift on the static yawed blade in the reverse flow regime and found good correlation at yaw angles representative of a slender delta wing. The movement of the center of pressure with changing angle of attack and sweep in the reverse flow regime is illustrated in Figure 1.7 from [1]. Tuft behavior in forward yaw versus backward yaw showed stark differences in flow topology. A sample is shown in Figure 1.8 from [1].

Figure 1.9 shows these SEVs at r/R of 0.5, at advance ratios 0.7, 0.85 and 1.0 (they are all at the same radial station), much as on a slender delta wing. The structures are seen at different r/R as well, as shown in our prior papers. Later experiments showed vortex 'bursting' at inboard stations. Figure 1.10 attempts to present a simplified representation of what is seen in Figure 1.9. In [44] we explored the velocity field under the rotor using SPIV, and then reconstructed the static pressure on the blade using the incompressible Bernoulli equation. In the following chapters, the experiments and results are discussed in more detail.

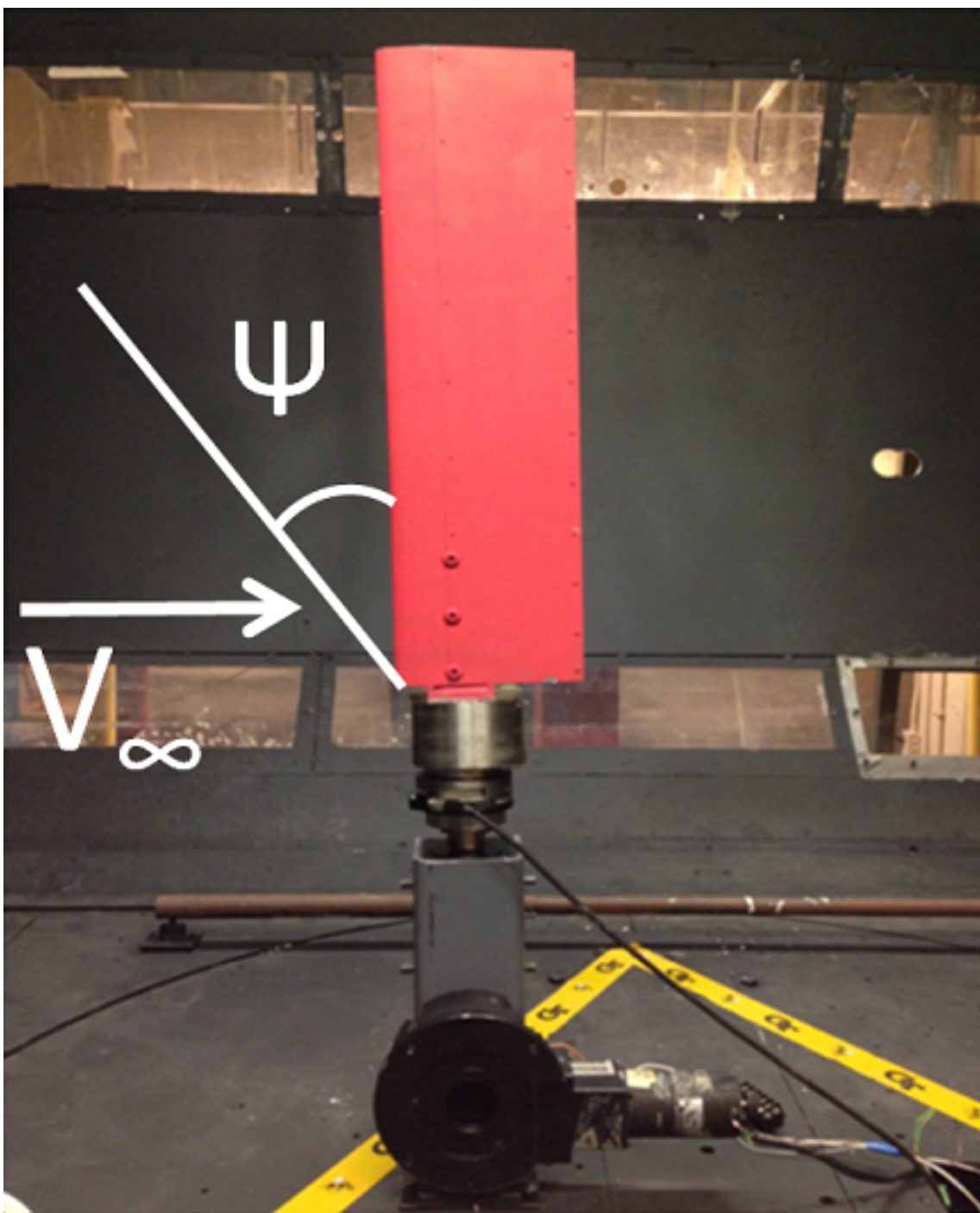


Figure 1.3: Rotor blade used in fixed-wing mode

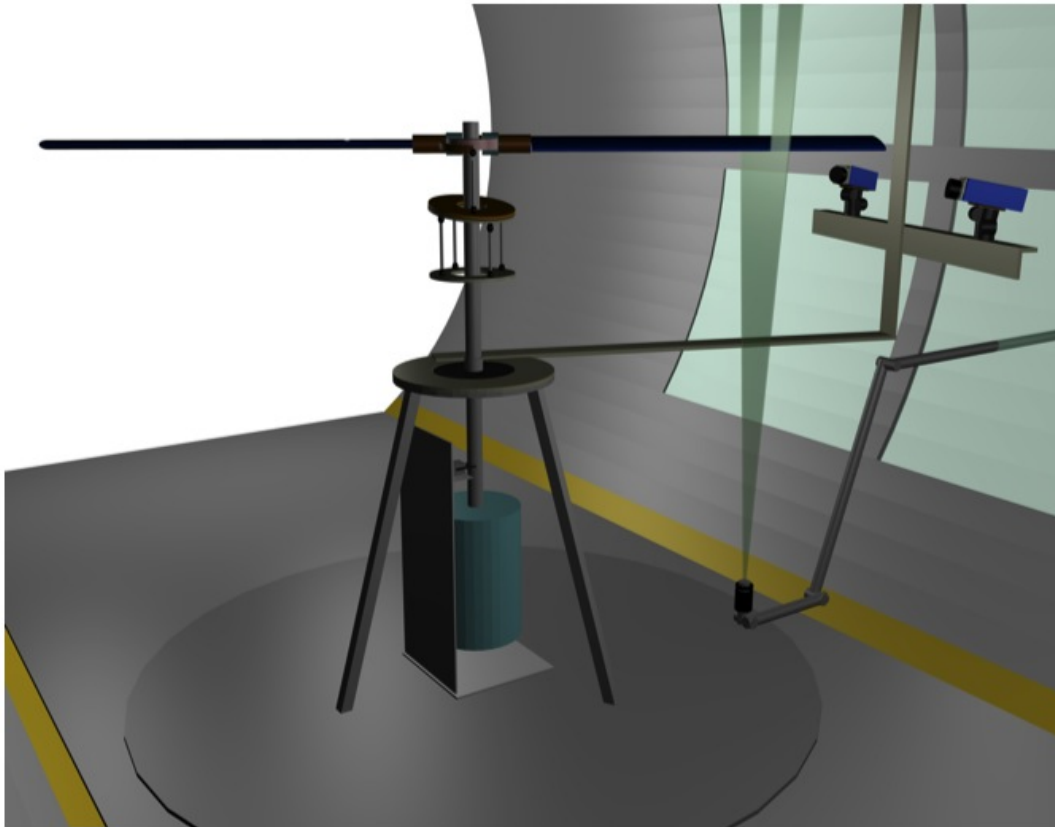


Figure 1.4: Test section as viewed from upstream, showing stereo PIV system looking at bottom of the retreating blade

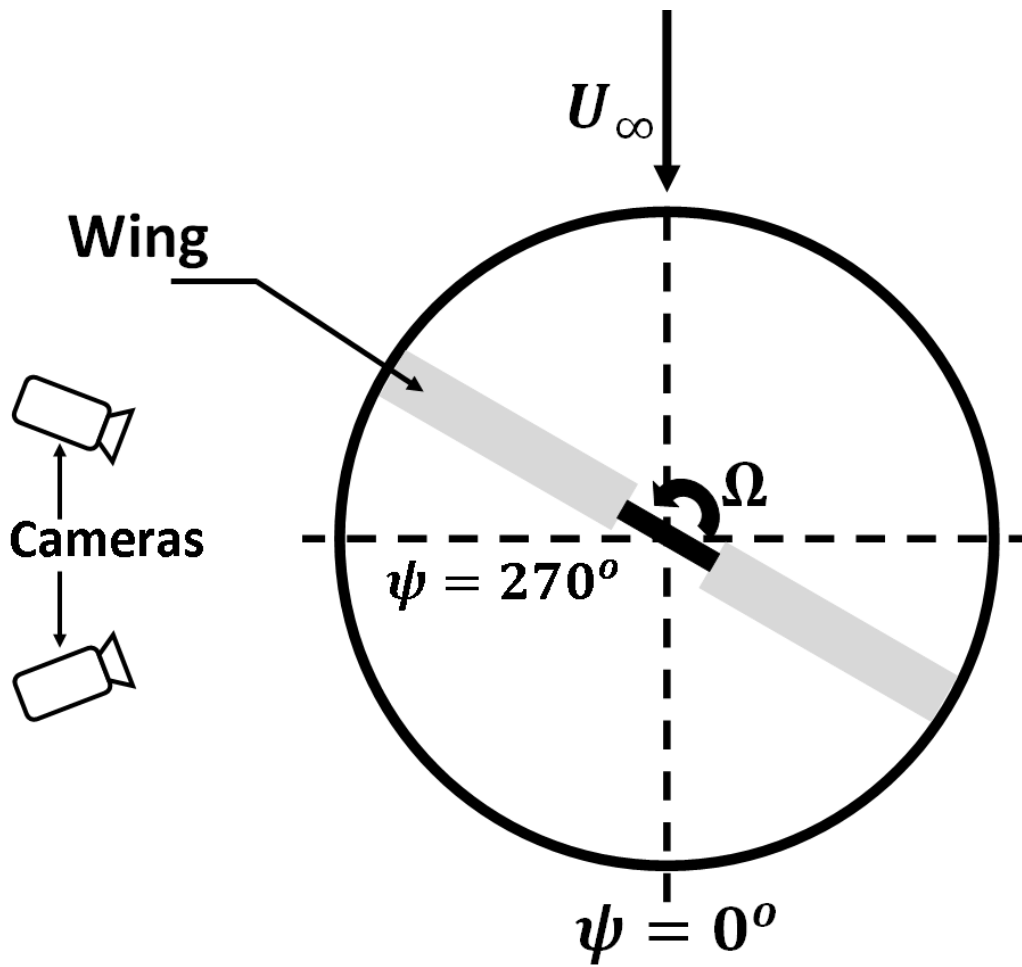


Figure 1.5: Schematic of top-view of the rotor disk (not to scale), for stereo PIV

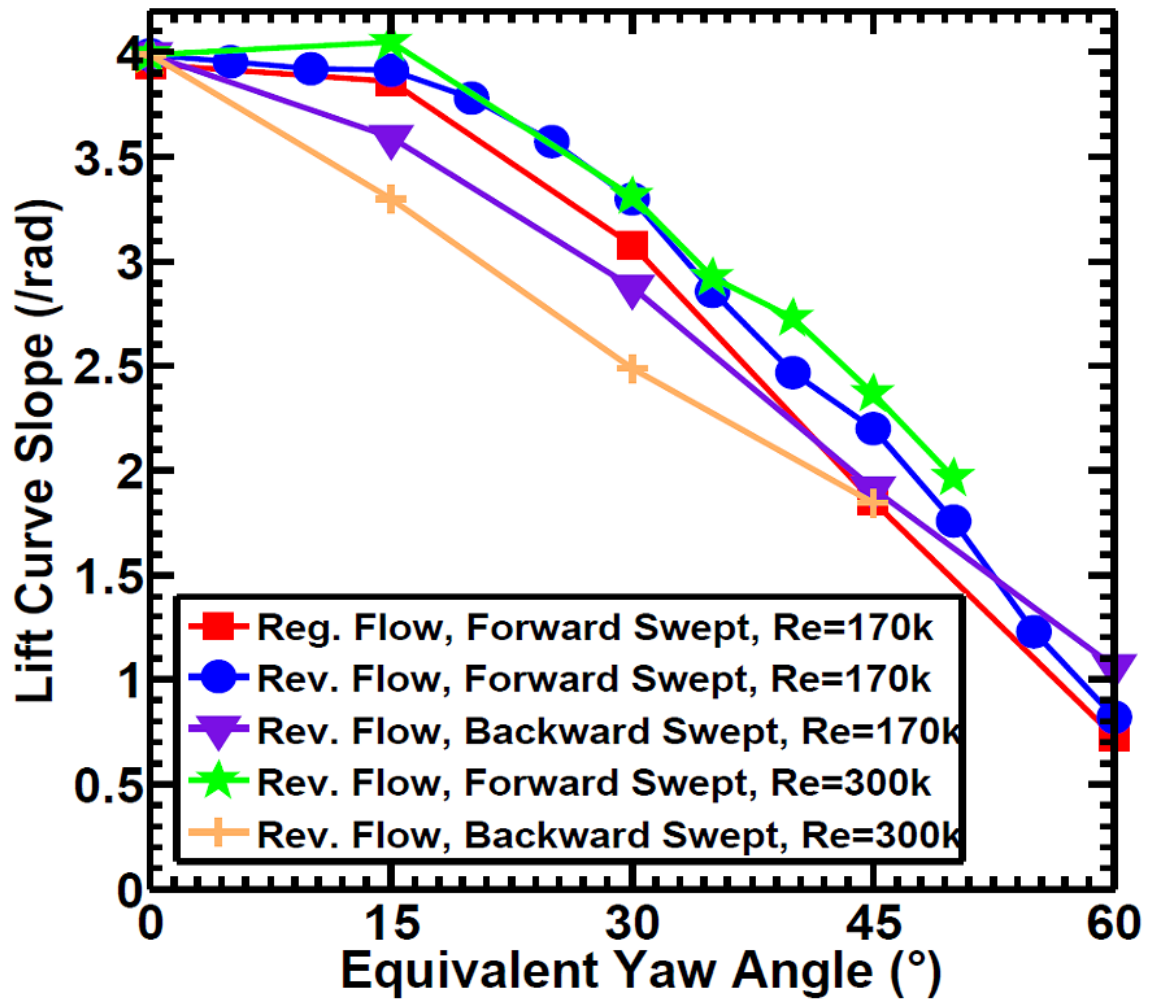


Figure 1.6: Lift curve slopes in forward and reverse sweep for a blade held as a fixed wing. From [1]

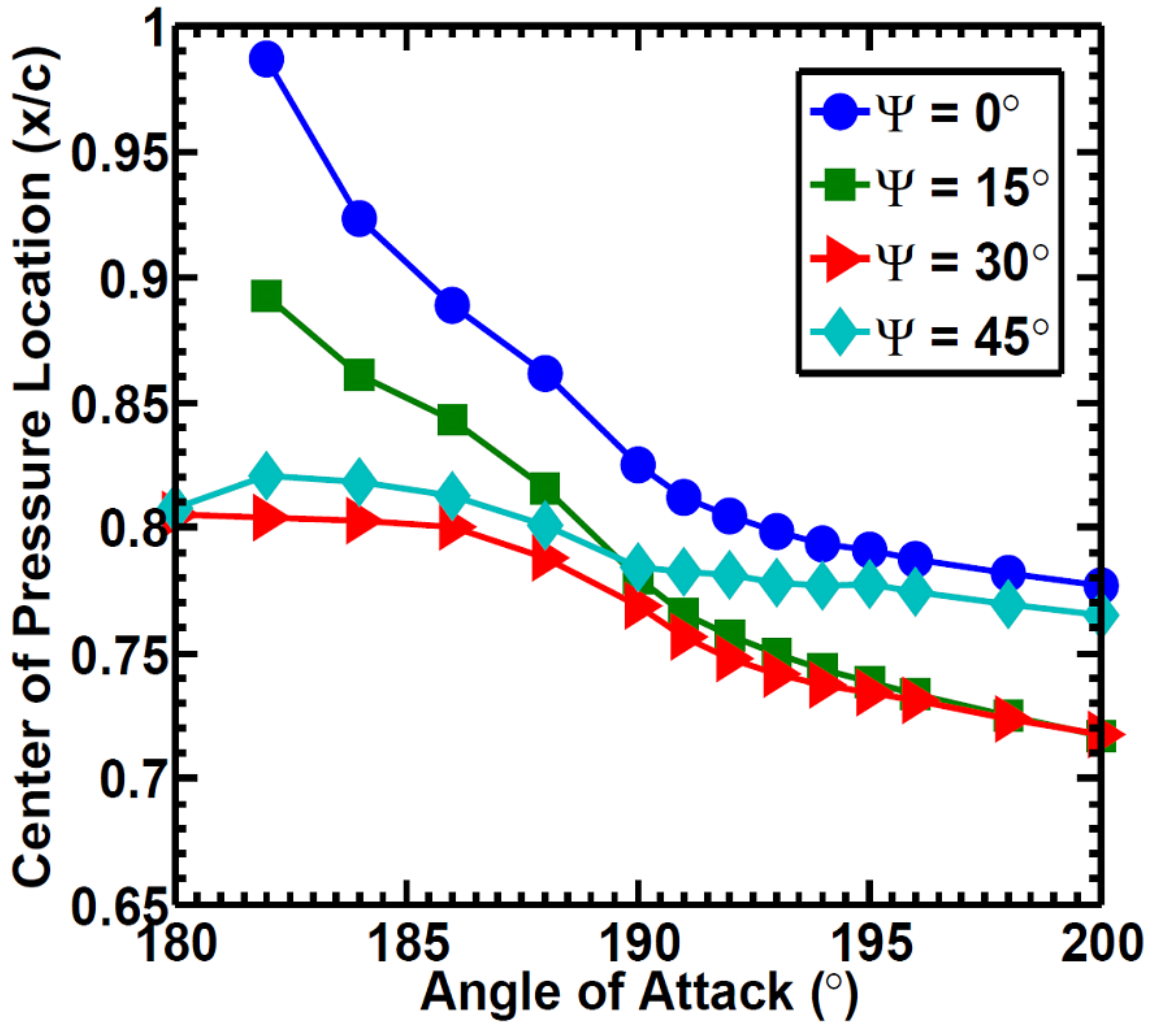


Figure 1.7: Movement of center of pressure on a fixed wing in reverse flow, with yaw and angle of attack, at chord Reynolds number of 300K. From [1]

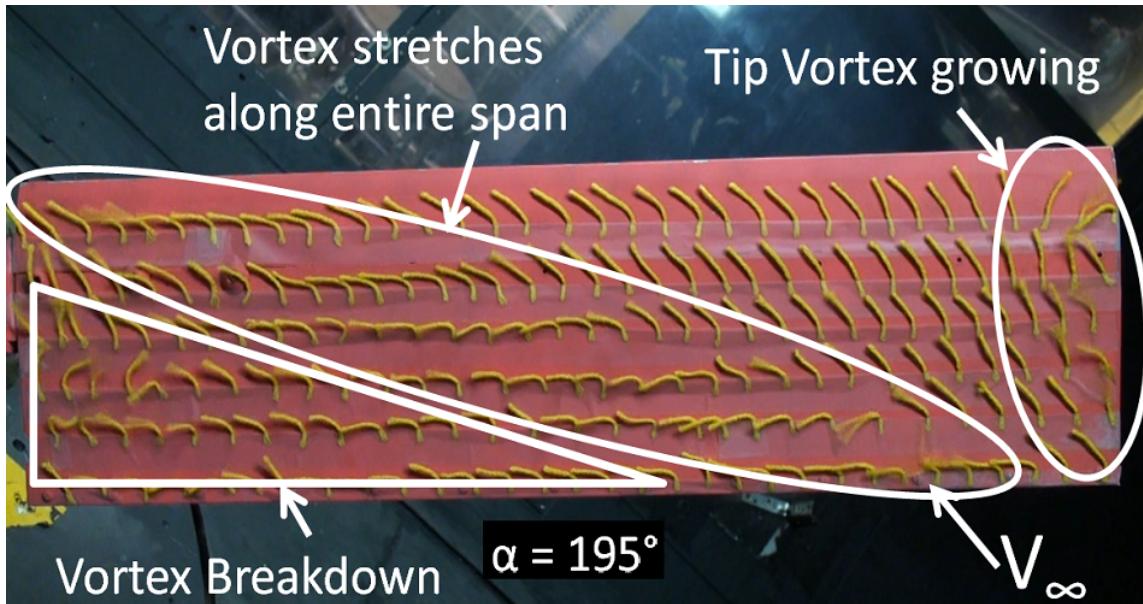


Figure 1.8: Surface tuft behavior shows clear evidence of a vortex and vortex bursting on a wing in reverse flow at 45 degree forward yaw and 15 degrees angle of attack. From [1]

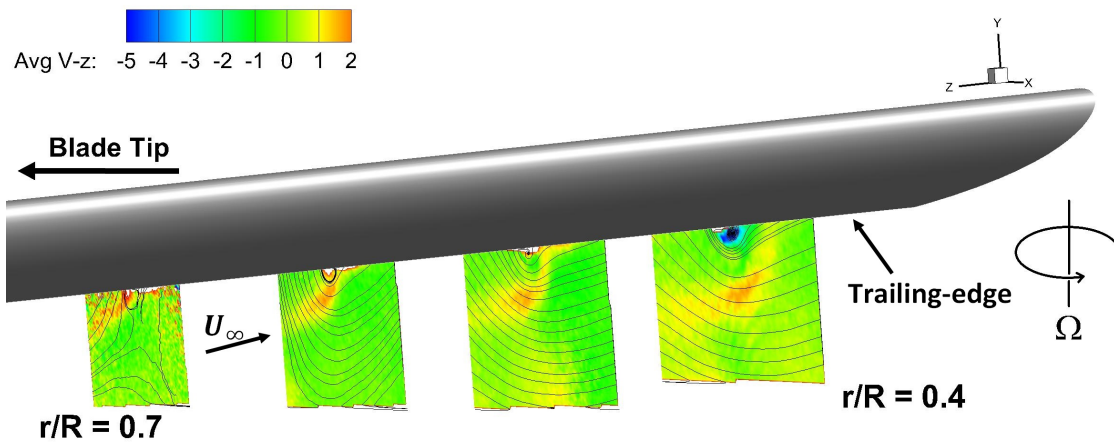


Figure 1.9: Sharp-edge vortex captured using stereo PIV at r/R of 0.5 under a rotating blade at 240 deg. azimuth, for several advance ratios. From [2]

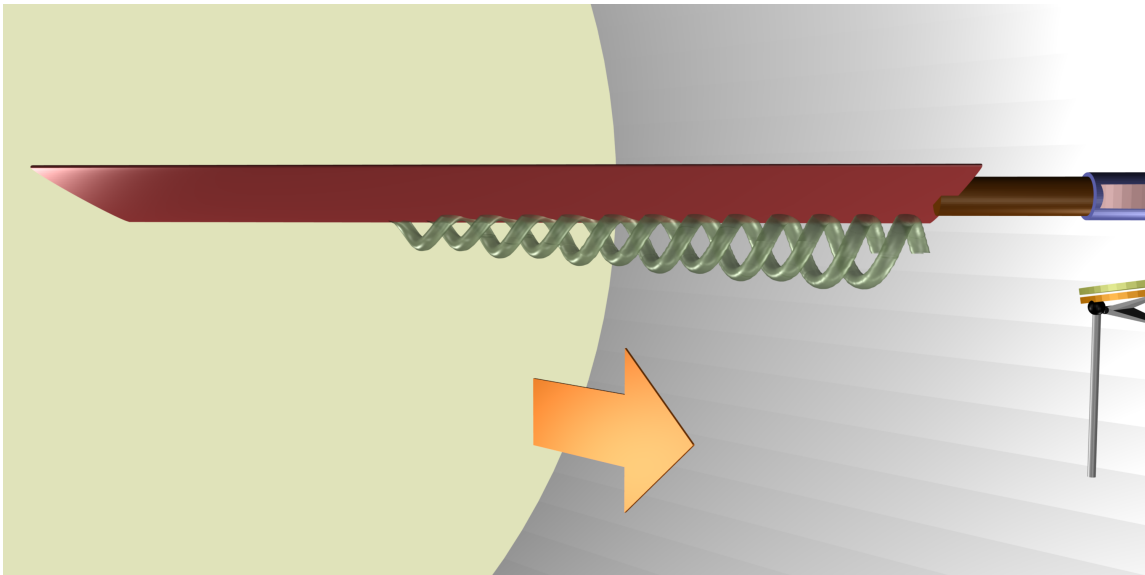


Figure 1.10: A simplified artist's conception of the SEV at 240 degrees, as it might be for a blade of larger aspect ratio. Note that the vortex starts at about r/R of 0.7, and grows inward. The dynamic pressure of the relative flow is highest near the root, but the vortex may also burst near the root because of the obstruction due to the hub.

Chapter 2

Experimental Methods

2.1 Wind Tunnel

Experiments were performed in the 2.13m×2.74m John Harper wind tunnel at our institution. The untwisted rectangular blade has a NACA 0013 planform. The rotor used in the rotating experiments has two such blades attached to a teetering rotor hub actuated by a 3.73 kW motor. Figure ?? shows the fixed wing and rotor setups with the laser sheet used for stereo PIV. Please refer to [3, 43] for further detail.

The same blade was used in fixed-wing experiments over a wide range of yaw and angle of attack in both forward-facing and reverse flow, with 6-DOF load measurements and tuft visualizations conducted. The blade was then mounted on the rotor, and held stationary at discrete values of yaw corresponding to rotor azimuths of 240, 270 and 300 degrees, at angles of attack in the range of those encountered in the rotor tests. Here it is noted that the angle of attack calculation is approximate. In actual rotating mode, the local section angle of attack will vary. This is because the inflow will vary due to the wake influence. and the local relative velocity due to rotation. Only an expected average value can be set in fixed-wing mode. Particle image velocimetry was used to study the flowfield under the blade in reverse flow. These are compared with results obtained later under the rotating blade.

2.2 Instrumentation and data processing

A NACA 0013 untwisted rectangular blade with an aspect ratio $AR = 3.49$, a chord $c = 0.178$ m, and a span $b = 0.622$ m was set up as shown in Fig. 2.1. Stepper motors were used to control pitch and yaw. A 6-DOF load cell was used to measure aerodynamic loads. A 5Hz low pass digital filter removed noise, and a calibration matrix converted the filtered voltage values into forces and moments. Raghav et al. [3] further details the instrumentation and data processing. This blade is part of the 2-bladed teetering rotor system already used in forward flight experiments in this tunnel, and also used in experiments at high advance ratios. Thus the aspect ratio and root structure of the blade were dictated by the requirements of the rotor experiments, and it was essential to use the same in these fixed-wing experiments for a valid comparison with rotating-blade aerodynamics. A high torque stepper motor with a resolution of 0.1° was used to control angle of attack, α , and a high torque stepper motor with a resolution of 1° was used to control yaw angle, Ψ . The motors were controlled by the ν Drive NI motion controller. A picture of the rotor blade setup inside the wind tunnel is shown in Fig. 2.1.

In rotating mode, the collective pitch angle was 7° and the longitudinal cyclic angle was -8° . This results in a 15° pitch at $\Psi = 270^\circ$. The phase locked SPIV measurements on the rotating rotor blade were acquired at advance ratios of $\mu = 0.7, 0.85, 1.0$ and a rotor angular velocity $\Omega = 200rpm(20.94rad/s)$. Measurements were gathered at radial locations of $r/R = 0.4, 0.5, 0.514, 0.6, 0.7$ and at azimuthal angles $\Psi = 240^\circ, 270^\circ, 300^\circ$ equivalent to $\Psi_{static} = 30^\circ, 0^\circ, -30^\circ$ for the static blade in prior work [1, 42]. Table 3.4 summarizes the flow and test conditions.

Table 2.1: High advance ratio facility rotor specifications

Parameter	Value
Blade span, chord (m)	0.622,0.178
Aspect ratio, solidity	3.49,0.0895
Radius, floor height(m)	0.889,1.3
Precone, max TPP tilt $^\circ$	1.6,16
Maximum collective, cyclic $^\circ$	10,6.5

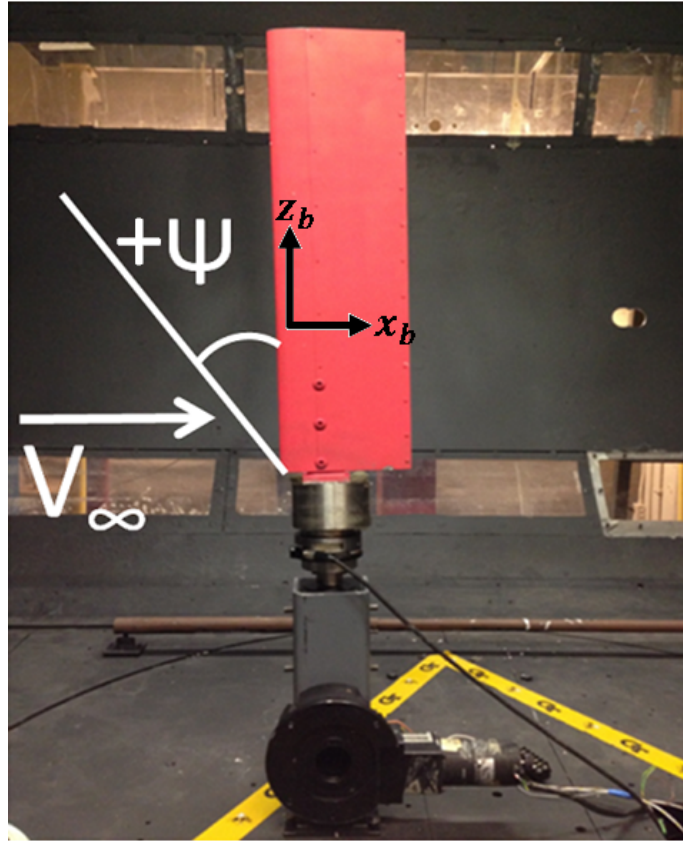


Figure 2.1: Side view of the rotor setup in the wind tunnel, where x_b and z_b are blade fixed coordinates)

2.3 Stereoscopic-PIV instrumentation

Stereoscopic-PIV (SPIV) was used to investigate the 3D flow field under the rotating blade. A double-cavity Nd:YAG laser delivered 200 mJ, 5ns pulses at up to 14 double-pulses per second. One velocity field was accessible per rotor revolution, synchronized to the same blade. The light sheet was 2 mm thick. Seeding with approximately $10\mu\text{m}$ droplets came from a Laskin-nozzle aerosol generator. The blade was coated with matte black paint to minimize laser reflections from the lower surface. Surface scattering was masked during velocity vector computations. A series of 100 phase-locked image pairs (implying over 100 revolutions, or 30 seconds at 200 rpm) was acquired at each measurement location using two LaVision PRO-X 2M cameras with 50 mm, f/8 lenses, 1600×1200 pixel resolution and pixel size of

Table 2.2: Test matrix for experiments

Azimuthal angle (Ψ°)	Radial position (r/R)	station	Advance Ratio (μ)
240°	0.4, 0.5, 0.6, 0.68		0.7, 0.85, 1.0
270°	(0.7 for $\Psi = 240^\circ$)		
300°			

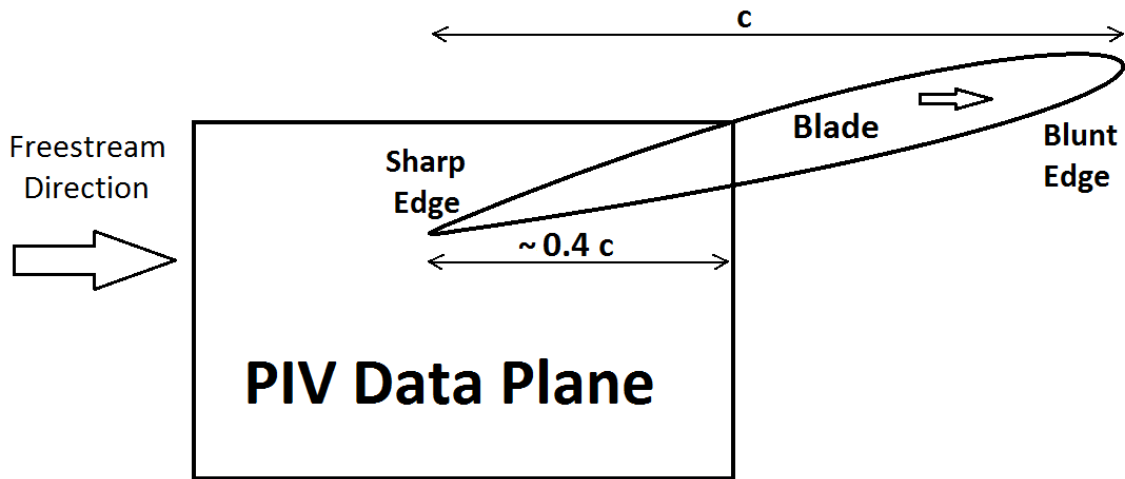
$7.4 \times 7.4 \mu\text{m}^2$. The stereo angle between camera optical axes varied between 20° and 39° for different radial locations. The particle size in the camera image ranged from 1.76 pixels to 2.81 pixels. LaVision DaVis 8.0 software was used to compute velocities from spatial cross-correlation between the images. An interrogation window overlap of 50% and a second interrogation pass with a reduced window size were used to increase the signal-to-noise ratio of the correlation peak. The first and second passes used interrogation windows of 64×64 and 32×32 pixels. This yielded a spatial resolution between velocity vectors of $1.4 \text{ mm} - 2.2 \text{ mm} \sim 0.008c - 0.012c$. An allowable range of vector magnitudes and a median filter were specified to reduce noise at the edges of the field of view. Figure 2.2 shows a velocity measurement window and the orientation of pressure contour plots.

2.4 Accuracy estimates

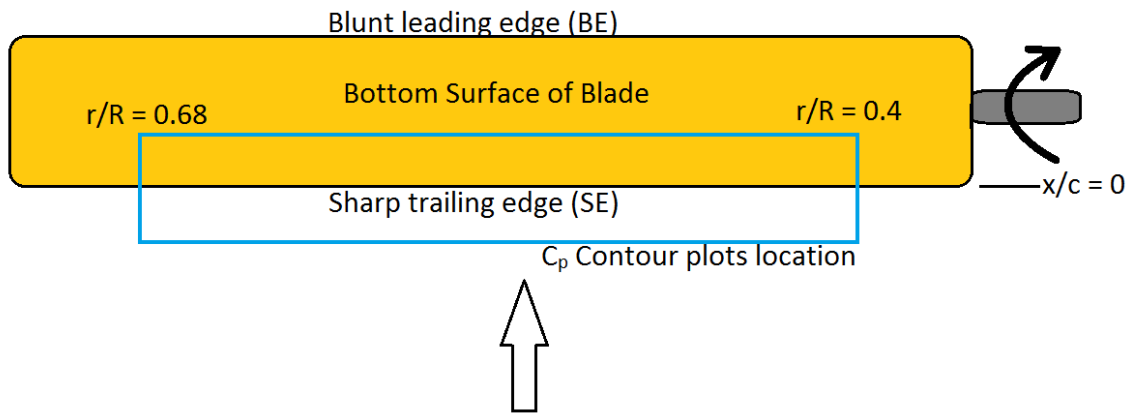
Estimates are repeated from [4, 43] by permission, and summarized in Table 2.3.

Table 2.3: Summary of velocity uncertainty estimates

Type	Error
In-plane random error	0.074–0.252 px
In-plane bias error	0.01 m/s
In-plane measurement error ($\%U_p$)	0.2%–0.96%
Out-of-plane measurement error ($\%W_p$)	0.29%–1.57%



(a) Approximate region where SPIV results are captured



(b) Bottom surface C_p contour region

Figure 2.2: Measurement Regions

Table 2.4: Blade Motion Amplitude and Phase

Advance Ra- tio (μ)	Amplitude deg. (r/R)	A, Phase, deg (ϕ)
0.7	3.38°	-31.1°
0.85	3.47°	-20.18°
1.0	3.73°	-7.7°

2.5 Tip Path Plane (TPP) and Blade Vertical Motion

The lateral and longitudinal tilt of the TPP were measured using two video cameras calibrated against a grid-board. The results were first shown in [2]. The vertical velocity of the blade at each station was calculated from phase-shifted sinusoidal fits with the measured values at 0-180 and 90-270. At each μ and r/R, blade speed variation with azimuth is given by:

$$w = A\left(\frac{\pi}{180}\right)\left(\frac{r}{R}\right)\Omega\cos(\psi - \phi) \quad (2.1)$$

A and ϕ are given in Table 2.4. The curve fits are accurate to well under 0.5 percent error, and the measurement error is discussed above, uncertainty in fitting with only two points precludes converting velocity data to true blade-fixed coordinates. The blade vertical speed in Figure 2.3, found by differentiating the curve fit for position, can be on the order of 1m/s as μ rises. TPP orientation does not agree with textbook speculations. This is not surprising because of the uncertain aerodynamics in the reverse flow region. In converting to 'blade-fixed' coordinates to clarify vortical structures, only the predetermined constants arising from free stream speed and blade section tangential speed are subtracted.

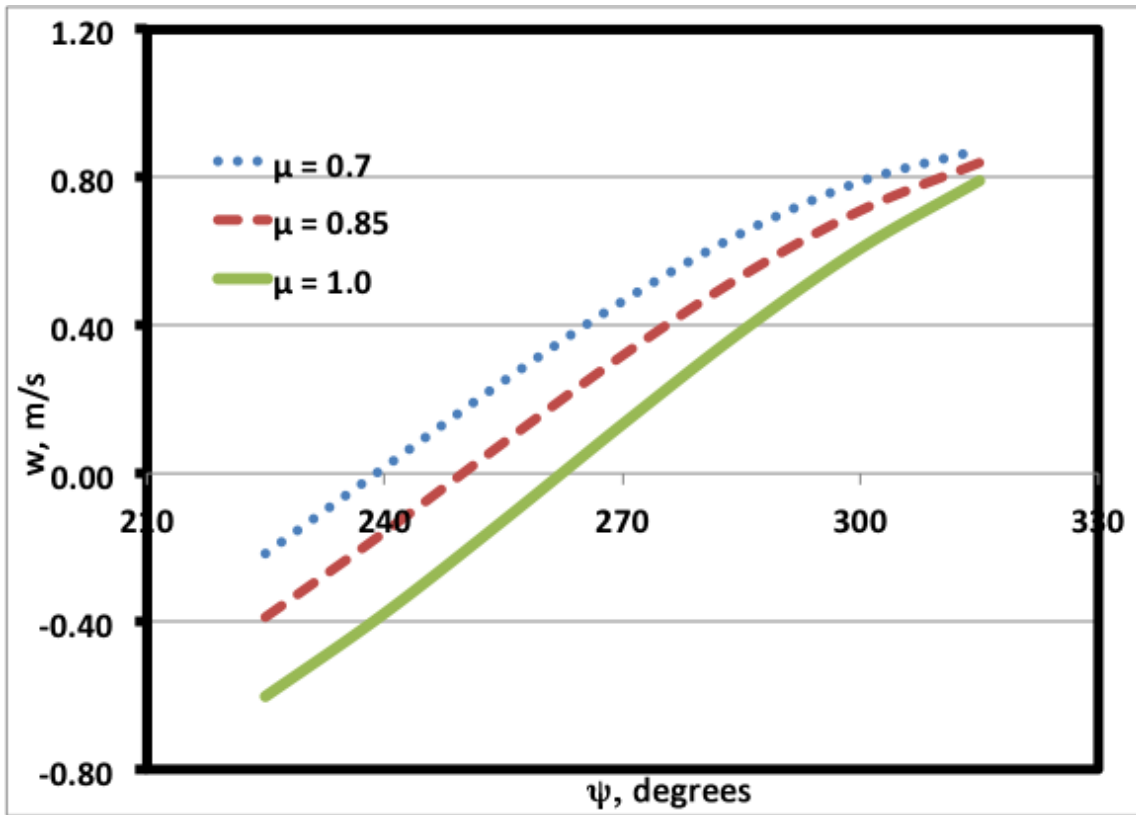


Figure 2.3: Blade vertical speeds in m/s for different advance ratios in the reverse flow regime

Chapter 3

Fixed Wing Results

In this chapter we pursue the hypothesis that the sharp trailing edge of a reverse flow blade develops an attached vortex in a similar manner to a sharp-edged delta wing. Lift, drag and pitching moment data for a static yawed blade in reverse flow are acquired using a load cell and the lift measurements are compared to predictions made with an adaptation of the Polhamus model. Surface tuft flow visualization confirms the presence of an attached span-wise vortex on the blade. Surface flow behavior is used to explain the behavior of observed aerodynamic loads, and correlations are made to previous results found in the literature. Vorticity transport analysis is used to justify the surface flow behavior variation with yaw angle and angle of attack.

The first step in this process was the exploratory wind tunnel study performed by Raghav et al. [3] on reverse flow over a static yawed wing. They found evidence of vortex-induced lift. Load cell measurements showed higher lift curve slopes for reverse flow test cases when compared to regular flow cases at the same yaw angles, and tuft visualization confirmed the existence of an attached vortex on the rotor blade in reverse flow. In that Note we presented a hypothesis that vortex lift similar to that on the swept leading edge of a delta wing, may be a strong phenomenon both in the case of the yawed reversed-flow static blade, and in the case of the retreating rotor blade.

In this chapter we present results from further analysis from these experiments, and further experiments over a range of yaw angles. In addition, the vortex flow hypothesis from the previous study is pursued and expanded by using the Polhamus suction analogy [37] for delta wing lift to predict reverse flow lift curves. Drag polars, pitching moments and chordwise center of pressure movement are also analyzed in

addition to flow visualization analysis at various yaw angles and Reynolds numbers. Use of a static yawed wing allows rotational effects to be decoupled from the already complex behavior of the reverse flow region. The wing used in this study is part of a two-bladed rotor used in dynamic stall research by Raghav [3]. The flow regime is limited to that of low Mach number and moderate chord Reynolds numbers.

3.1 Polhamus suction analogy for yawed rotor blade

The Polhamus suction analogy [37] is adapted for the case of a yawed wing in reverse flow as shown in Equation 3.1. The predictions are presented in the results and discussion section.

$$C_L = K_p \cdot \sin\alpha \cdot \cos^2\alpha + \left(K_p - K_p^2 \frac{1}{\pi e AR} \right) \frac{1}{\cos\Psi} \cdot \cos\alpha \cdot \sin^2\alpha \quad (3.1)$$

The terms on the right-hand side correspond to the lift generated by potential flow and the leading-edge vortex respectively. K_p depends only on the plan-form shape and gives the lift-curve slope from small-perturbation theory for small angles of attack. In this paper, K_p will be set equal to the lift-curve slope of the rotor blade in regular flow for each yaw angle being examined. The delta wing sweep angle Λ is equivalent to the yaw angle Ψ , of the blade used in this work. Oswald's efficiency factor e is calculated using Shevell's method [45].

3.2 Flow and test conditions

The experiments were performed at two Reynolds numbers of 1.7×10^5 and 3.0×10^5 at yaw angles ranging from $\Psi = -60^\circ$ (backwards yaw) to $\Psi = 60^\circ$ (forwards yaw). The test cases are summarized in Table 3.4 and described below:

1. The first test validated the experimental method [3] by comparing results for regular flow against published data.
2. The second test acquired lift, drag and pitching moment data for the rotor blade in reverse flow at two Reynolds numbers and various yaw angles. Angle of attack(α) resolution was lower in the linear region of the lift curves and higher near the stall region.

Table 3.1: Test matrix for experiments

Test	Flow Type	Data Acquired	Ψ and α	$Re(\times 10^5)$
1	Regular Flow	Validation	$0^\circ \leq \Psi \leq 60^\circ, 0^\circ \leq \alpha \leq 30^\circ$	1.7
2	Reverse Flow	Lift, Drag, Pitching Moment	$-60^\circ \leq \Psi \leq 60^\circ, 180^\circ \leq \alpha \leq 210^\circ$	1.7, 3.0
3	Reverse Flow	Flow Visualization	$\Psi = \pm 30, \pm 45, 180^\circ \leq \alpha \leq 220^\circ$	1.7, 3.0

- The third test consisted of surface flow visualization using tufts at two Reynolds numbers and various yaw angles. The rotor blade was pitched through the angle of attack range in increments of 5° .

Dynamic pressure was measured using a Barotron pressure transducer connected to a Pitot-static probe in the test section. Reynolds numbers were set at 170,000 and 300,000 by adjusting tunnel speed as gauged from the dynamic pressure, and ambient temperature and pressure measurements. Lift and drag were measured by setting the rotor at a desired Ψ , the wind tunnel to a speed corresponding to the desired Reynolds number, and stepping the blade through the desired angles of attack. A Ψ of 0° corresponds to the blade span being perpendicular to the freestream. If the rotor blade trailing edge is facing into the flow, then $\Psi = 0^\circ$ corresponds to a helicopter blade azimuth angle of 270° as seen in Fig. ???. Yaw angles above 60° were not used because an advance ratio greater than 2 would be necessary to achieve reverse flow in this region of a helicopter rotor disc. Reverse flow conditions were achieved by rotating the rotor blade 180° so that the trailing edge faced into the flow. In this paper, $\alpha = 180^\circ$ corresponds to the sharp trailing edge of the blade facing into the flow with no angle of attack, and $\alpha = 200^\circ$ would correspond to the the sharp trailing edge facing into the flow with 20° angle of attack. Reverse flow data were acquired in the range of $\Psi = -60^\circ$ (*backward sweep*) to $\Psi = 60^\circ$ (*forward sweep*) and at $\alpha = 180^\circ - 190^\circ$ in increments of 2° , at $\alpha = 190^\circ - 196^\circ$ in increments of 1° , at $\alpha = 198^\circ$, and at $\alpha = 200^\circ$. Data were acquired at α values greater than 200° when necessary to observe the stall region. The force and moment data presented are ensemble averaged data with approximately 300,000 samples taken at each α .

3.3 Error analysis

The total error in measurement of the aerodynamic load coefficients was computed to be $\pm 1.61\%$ in the worst case. The total error was computed using the individual errors of the parameters listed in Table 3.2. The ensemble averaged data are repeatable with a standard deviation within 4.5% of the measured average loads. The blade airfoil contour was measured at 18 different locations across the span of the blade to quantify the difference from NACA0013 coordinates. The root mean square error for the difference was less than 0.1% of the chord.

Table 3.2: Summary of errors

Parameter	Error Estimate
Density	0.03%
Velocity	0.04%
Reynolds number	± 470
Load cell calibration	$\pm 1.37\%$
Yaw angle	$\pm 0.05^\circ$
Angle of attack	$\pm 0.01^\circ$

3.4 Aerodynamic loads

3.4.1 Lift

Lift curve slopes for the reverse flow regime at positive and negative yaw angle and two different Reynolds numbers are shown in Fig. 3.1 along with forward yaw regular flow lift curve slopes at $Re = 1.7 \times 10^5$. Figure 2.1 defines the positive (forward) and negative (backward) yaw angles. Lift curve slopes were calculated using the linear region in the equivalent α range of $0^\circ - 10^\circ$. The occurrence of stall near $\alpha = 10^\circ$ in both regular and reverse flow regimes agrees with Lind et al. [7] for a NACA 0012 airfoil in regular and reverse flow and with NACA 0012 reverse flow data collected by Critzos et al. [12] in the Langley low-turbulence tunnel. Raghav et al. [3] showed that the regular flow lift curve slopes follow the $\cos^2\Psi$ fit predicted by cross-flow equivalence [46].

The lift curve slopes for the forward yaw reverse flow cases are slightly higher than the corresponding regular flow lift curve slopes, which suggests that there is an extra source of lift in the reverse flow regime. The difference in the regular and reverse flow lift curves seen in this study correlates well with the difference in lift coefficient seen by Bartlett [47] for beveled and rounded wings with sweepback angle. The lift curve slopes at $Re = 3.0 \times 10^5$ are slightly higher than the ones at $Re = 1.7 \times 10^5$, which suggests that Reynolds number does have an effect on aerodynamic loads for a rotor blade in the reverse flow regime. The difference between the two Reynolds numbers is small and even non-existent for certain yaw angles, which supports the suggestion made by Lind et al. [7] that the aerodynamic forces in reverse flow are less dependent on Reynolds number due to early separation. Reynolds number appears to have little if any effect on the forward yaw reverse flow lift curves. This is consistent with the negligible effect of Reynolds number on aerodynamic loads for sharp-edged delta wings [48].

The backward yaw lift curve slopes do not follow the expected $\cos^2\Psi$ fit, and Reynolds number does appear to have more effect on the lift curve slopes at $\Psi = -15^\circ$ and $\Psi = -30^\circ$ when compared to forward yaw angle cases. Possible explanations for this behavior are the different orientation of the mount and wingtip in the backward yaw case - this is further examined in the flow visualization section.

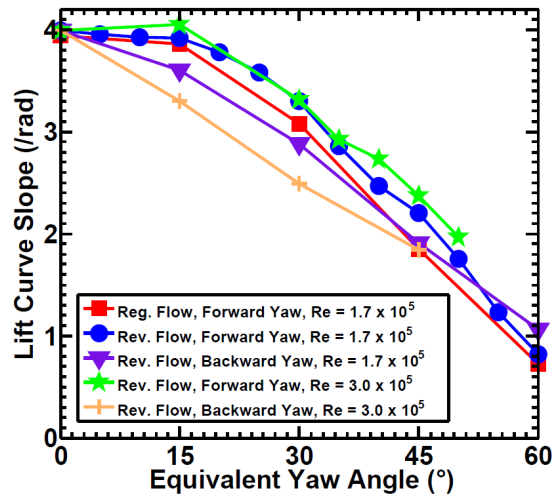


Figure 3.1: Lift curve slopes at various Ψ and Re (Ψ negative for backward yaw)

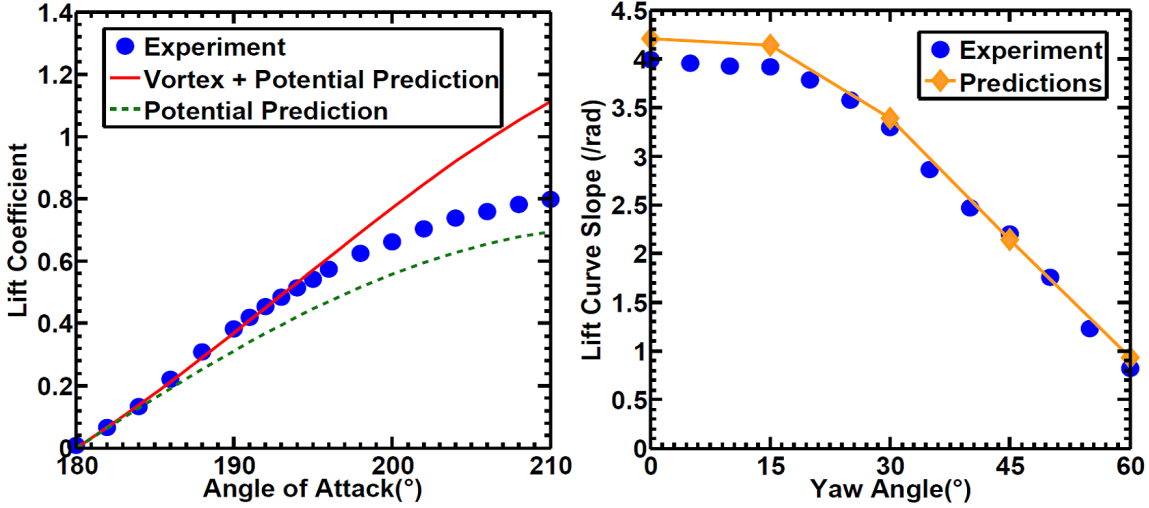
3.4.2 Predictions using Polhamus suction analogy

The Polhamus suction analogy described in section 3.1 was used to predict lift curves for the reverse flow rotor blade at $Re = 1.7 \times 10^5$ and forward yaw values of $\Psi = 0^\circ, 15^\circ, 30^\circ, 45^\circ$, and 60° . These yaw values were chosen because they allowed the K_P term in the vortex lift equation to be matched to the lift curve slopes obtained from the regular flow validation trials. Figure 3.2(a) compares the predictions made by the vortex lift model at $\Psi = 45^\circ$ and $Re = 1.7 \times 10^5$ to experimental data. The solid line is the prediction made using the full equation 3.1, and the dashed line is the prediction made using equation 3.1 with K_v (second term on the right hand side) set to zero. The dashed line corresponds to lift predicted by potential theory only. The full vortex lift model predicts the lift coefficient with good accuracy up until $\alpha = 195^\circ$, where the experimental lift curve begins to more closely follow the potential prediction. In reality, at higher angle of attack the vortex tends to burst [49] and the measured lift will decrease. However, the current mathematical model does not account for the vortex burst phenomenon. This is reconciled in the surface flow visualization section 3.5, where vortex burst is observed at higher angle of attack. It should be noted that the experimental lift curve is higher than the potential prediction well after diverging from the vortex model, which may signify that some vortex lift is being generated well after breakdown begins.

Lift curve slopes were calculated using the lift curve predictions generated by the vortex lift model and are compared to experimental data in Figure 3.2(b). The vortex lift predictions are fairly accurate for $\Psi \geq 30^\circ$. The over-prediction at lower Ψ stems from the fact that the Polhamus equation for low aspect ratio delta wings suffers at low Ψ values which correspond to the leading edge sweep of a high aspect ratio delta wing.

3.4.3 Drag and pitching moment

Drag polars for the regular and reverse flow regime at $\Psi = 30^\circ$ are shown in Figure 3.3(a). The drag polars at this Ψ are fairly representative of drag polars at other Ψ . The L/D ratios are higher in the regular flow cases. This agrees with results for delta wings, where a sharp-edged delta wing has a lower L/D than a delta wing with a rounded leading edge [50]. The regular flow L/D ratio at $\alpha = 10^\circ$ is almost twice as high as the corresponding reverse flow L/D. This result agrees with that discussed by Lind et al. [7] showing that a NACA 0012 airfoil in reverse flow would



(a) Lift curves for $\Psi = 45^\circ$ produced by vortex lift model and experiment
 (b) Lift curve slopes obtained from vortex lift model and experiment at $Re = 1.7 \times 10^5$

Figure 3.2: Lift predictions using the Polhamus model for a yawed blade in reverse flow

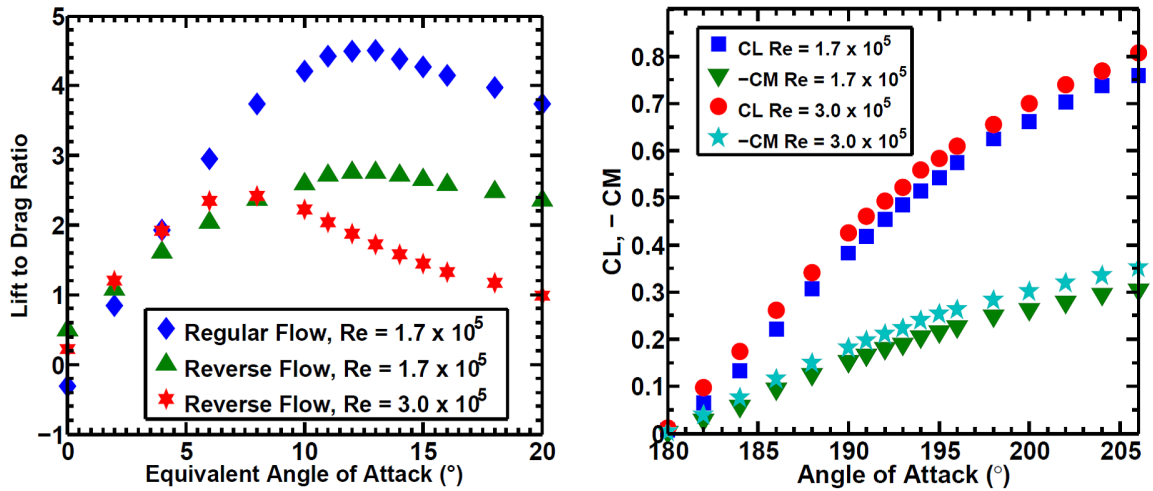
produce almost twice as much drag at the stall angle while still having the same $C_{L_{max}}$ as a regular flow airfoil.

The reverse flow pitching moments were proportional to lift in the linear region of the lift curve. A plot of C_L and C_M at $\Psi = 45$ for $Re = 1.7 \times 10^5$ and 3.0×10^5 is shown in Figure 3.3(b). The non-zero, negative pitching moment in the linear lift region suggests that the center of pressure was located closer to the effective leading edge (i.e., the sharp edge). The chordwise center of pressure was computed from the normal aerodynamic force using the lift and drag measurements as given by equation 3.2, and the measured pitching moment.

$$N = L \cos(\alpha) + D \sin(\alpha) \quad (3.2)$$

It should be noted that the resultant chordwise center of pressure location is an average over the span of the blade. The chordwise center of pressure locations for various forward yaw angles at $Re = 1.7 \times 10^5$ and $Re = 3.0 \times 10^5$ are shown in Figures 3.4(a) and 3.4(b) respectively. A 0.75c location on the plot corresponds to the quarter chord of the reverse airfoil. Data points derived from lift values lower than 0.3N were omitted due to high uncertainty.

Both plots show that at low Ψ , the center of pressure is even closer to the effective leading edge. A possible reason for this trend is discussed in the flow visualization section. The approximate $0.75c$ center of pressure location for both plots agrees with data collected by Datta [6]. For $Re = 1.7 \times 10^5$, the center of pressure locations start near $0.7c$ and move toward the effective leading edge as α is increased. Beyond the linear lift region, the center of pressure moves toward the effective trailing edge and eventually settles near $0.75c$ at $\alpha = 200^\circ$. The $Re = 3.0 \times 10^5$ cases show a different trend, with center of pressure locations that start closer to the effective leading edge and move toward the effective trailing edge as α is increased, eventually settling near $0.75c$. Reasons for the center of pressure movement will be discussed in the flow visualization section.



(a) Drag polars at $\Psi = 30^\circ$ ($\alpha = 180^\circ - 200^\circ$ for reverse flow cases)

(b) Variation of lift and pitching moment at $\Psi = 45^\circ$ (pitching moment negative about z_b axis)

Figure 3.3: Drag and pitching moment data for regular and reverse flow cases

3.5 Surface flow visualization

Surface flow visualization was performed using tufts attached to the suction side of the rotor blade. The tufts were 2.5 cm long pieces of yarn taped at 2.5 cm spacing, forming a grid over the entire suction side of the blade. A high definition camera was used to record the visualization. These experiments were performed at $Re =$

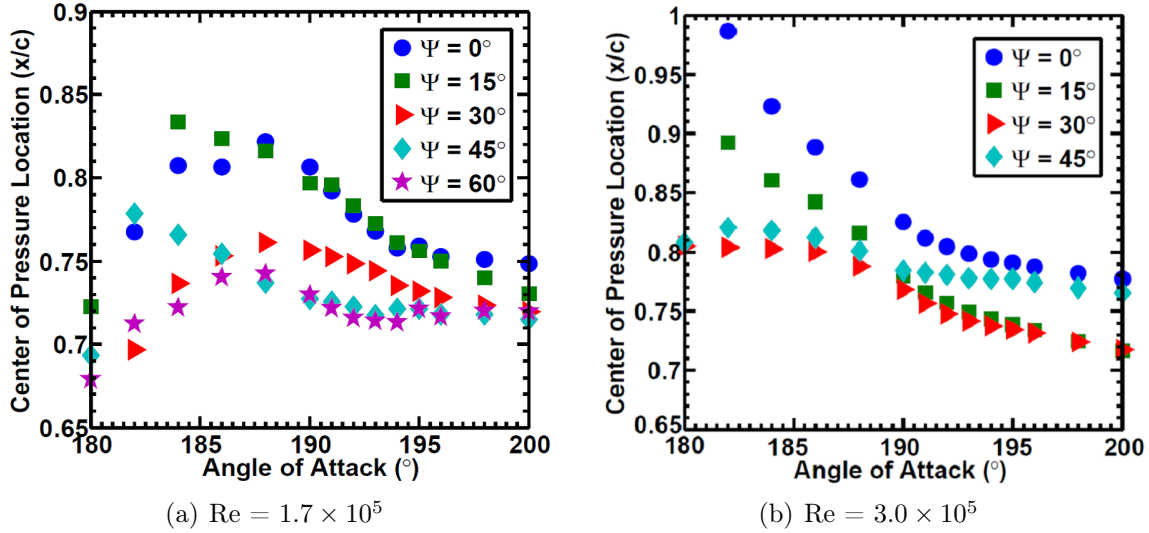


Figure 3.4: Variation of chordwise center of pressure location with α at various Ψ

1.7×10^5 and $Re = 3.0 \times 10^5$ at $\Psi = 30^\circ, 45^\circ, -30^\circ,$ and -45° . The blade was pitched through various α in increments of 5° . Reynolds number had little effect on the surface flow patterns. However, large differences in surface flow pattern were observed between forward and backward yaw cases. Hence only one Reynolds number case $Re = 1.7 \times 10^5$ is discussed in detail.

3.5.1 Forward yaw $Re = 1.7 \times 10^5$

A. $\Psi = 45^\circ$

Pictures of tuft flow visualization taken at $\Psi = 45^\circ$ and $Re = 1.7 \times 10^5$ are shown in Figures 3.6(a)– 3.6(d). At $\alpha = 185^\circ$ the tufts are mostly attached, but there are a few tufts at the effective leading edge moving in a clockwise, conical rotation pattern when looking from upstream. These rotating tufts are indicative of a leading edge vortex beginning to form. There are also some rotating tufts at the blade tip, indicating the existence of a tip vortex interacting with the freestream. As the blade is pitched to $\alpha = 190^\circ$, the leading edge vortex grows along the span. The rapid growth of the vortex as α increases from $5^\circ - 10^\circ$ correlates well with the large momentum deficit increase seen by Lind [7] for a NACA 0012 airfoil at $\alpha = 189^\circ$. In addition, there is a small region of the tufts exhibiting chaotic motion near the blade root, a characteristic of separated flow, indicating a

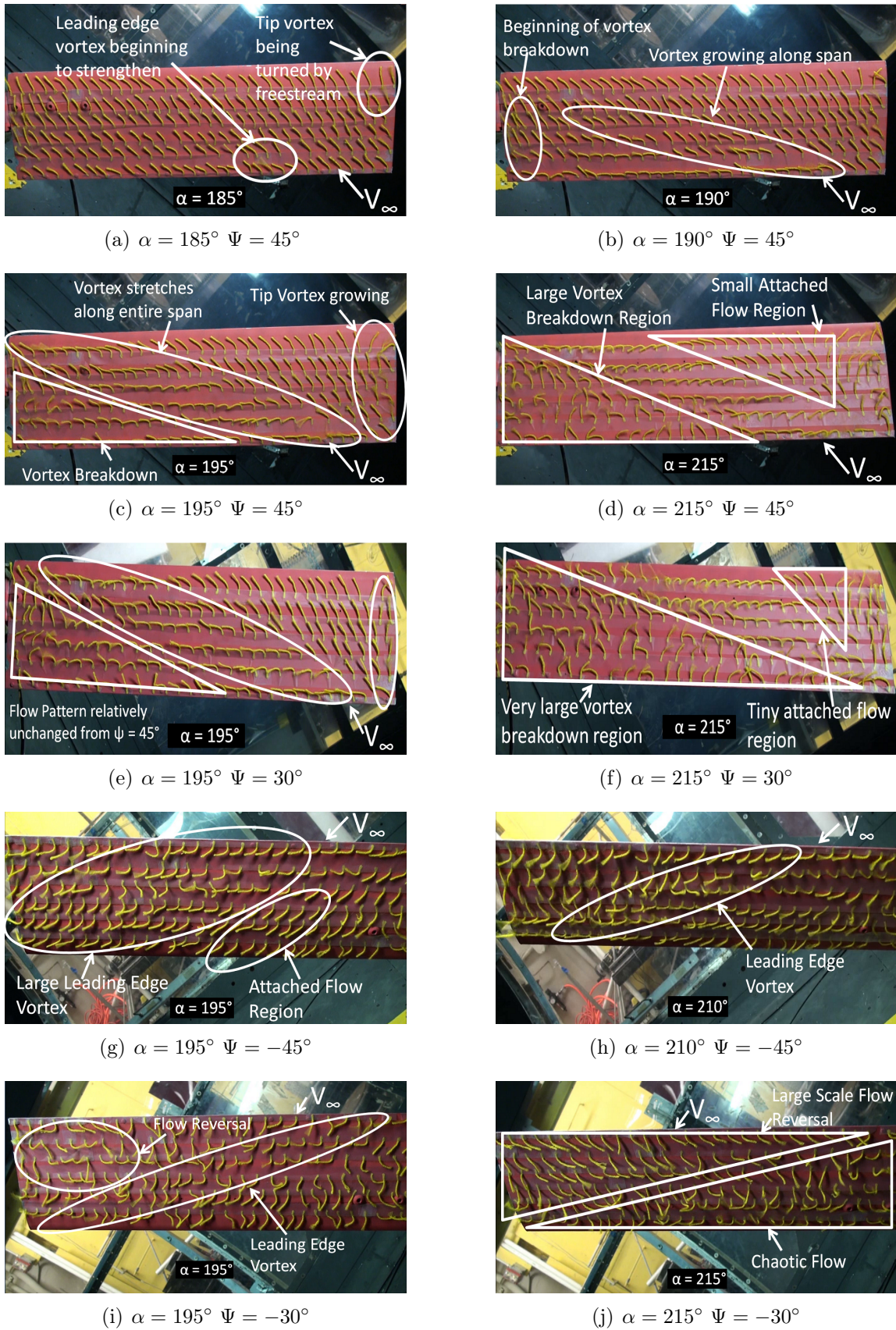


Figure 3.5: Tuft visualization at $Re = 1.7 \times 10^5$

vortex breakdown region. The vortex breakdown may be attributed to the adverse pressure gradient caused by the mount at the blade root. As the blade is pitched to $\alpha = 195^\circ$, the vortex breakdown region grows larger, which correlates well with the divergence of the experimental lift curve from vortex lift theory seen in Figure 3.2(a). By $\alpha = 215^\circ$, the leading edge vortex is almost completely broken down and there is only a small region of attached flow between the remnants of the leading edge vortex and the tip vortex region.

In the aerodynamic loads section we discussed the center of pressure on the yawed blade in reverse flow. The physical reasoning for the variation of the center of pressure with angle of attack is now reconciled with the flow visualization experiments. The growth of the leading edge vortex could explain the center of pressure movement seen in Figure 3.4(a). As the vortex becomes significant at $\alpha = 185^\circ$, the center of pressure would shift toward the location of the vortex at the effective leading edge. As the vortex grows along the span and reaches the effective trailing edge, the center of pressure would “follow” the mean position of the leading edge vortex toward the effective trailing edge, eventually settling near the 0.75c point. The vortex breakdown region is mainly confined to an area near the effective leading edge of the blade. The location of the vortex breakdown region near the effective leading edge could explain why the chordwise center of pressure appeared to be farther from the effective leading edge for higher Ψ cases in Figure 3.4(a) and Figure 3.4(b). The breakdown region would be expected to produce minimal or no lift, which would shift the chordwise center of pressure toward the effective trailing edge. The lower Ψ test cases would not develop a large vortex breakdown region because there would be less spanwise flow and a smaller adverse pressure gradient at the blade root, so the center of pressure would not be shifted as far toward the effective trailing edge.

It is worth noting that the position and shape of the attached span-wise vortex resembles that of the lower surface vortex predicted by Potsdam et al [20], which was attributed to ‘reverse-chord dynamic stall’. The similar vortex observed in this experiment on a static yawed blade suggests that the vortex predicted by Potsdam et al. may not be an artifact of rotation, or pitch rate. Based on prior flow visualization experiments Raghav et al. [3] proposed a flow topology for a blade in forward yaw in reverse flow regime.

B. $\Psi = 30^\circ$

Pictures of tuft flow visualization taken at $\Psi = 30^\circ$ and $Re = 1.7 \times 10^5$ are shown in Figure 3.5(e) and Figure 3.5(f). At $\alpha = 195^\circ$ the observed flow pattern is very similar to the one seen at $\Psi = 45^\circ$, but at $\alpha = 215^\circ$ a much larger vortex

breakdown region is observed. The attached flow region is also much smaller than the one observed for $\Psi = 45^\circ$. Reasons for these differences will be discussed in later sections.

3.5.2 Backward yaw $\text{Re} = 1.7 \times 10^5$

A. $\Psi = -45^\circ$

Pictures of tuft flow visualization taken at $\Psi = -45^\circ$ and $\text{Re} = 1.7 \times 10^5$ are shown in Figure 3.5(e) and Figure 3.5(f). At $\alpha = 195^\circ$ the tuft behavior suggests that a large leading edge vortex is present, and no significant signs of vortex breakdown are observed. Unlike the forward yaw $\Psi = 45^\circ$ case, mount obstruction does not impede the growth of the leading edge vortex by creating an adverse pressure gradient. A smaller adverse pressure gradient may be present at the rotor blade tip due to a tip vortex, but at this angle of attack it appears that the spanwise flow mostly negates the effect of any tip vortex. The attached flow region is fairly small, which is partly due to mount interference near the blade root. At $\alpha = 210^\circ$ the leading edge vortex more closely resembles the one seen at $\Psi = 45^\circ$.

B. $\Psi = -30^\circ$

Pictures of tuft flow visualization taken at $\Psi = -30^\circ$ and $\text{Re} = 1.7 \times 10^5$ are shown in Figure 3.5(e) and Figure 3.5(f). At $\alpha = 195^\circ$ a leading edge vortex is apparent, but it does not appear to have much strength. Some tufts near the blade tip signify a reversal of the expected span-wise flow direction. At $\alpha = 215^\circ$ the rotor blade planform can be evenly divided into two regions: a region where the flow appears to be fairly laminar but directed toward the root of the blade in opposition to the freestream flow, and a region of chaotic flow.

3.5.3 $\text{Re} = 3.0 \times 10^5$ and $\alpha = 195^\circ$

The flow patterns for the $\text{Re} = 3.0 \times 10^5$ test cases were essentially unchanged from the $\text{Re} = 1.7 \times 10^5$ cases, which is consistent with previous literature on sharp-edged delta wings [48].

3.5.4 Flow topology

Raghav et al. [3] proposed a flow topology for a static forward yawed blade in the reverse flow regime. The flow topology shows three distinct flow regimes – attached

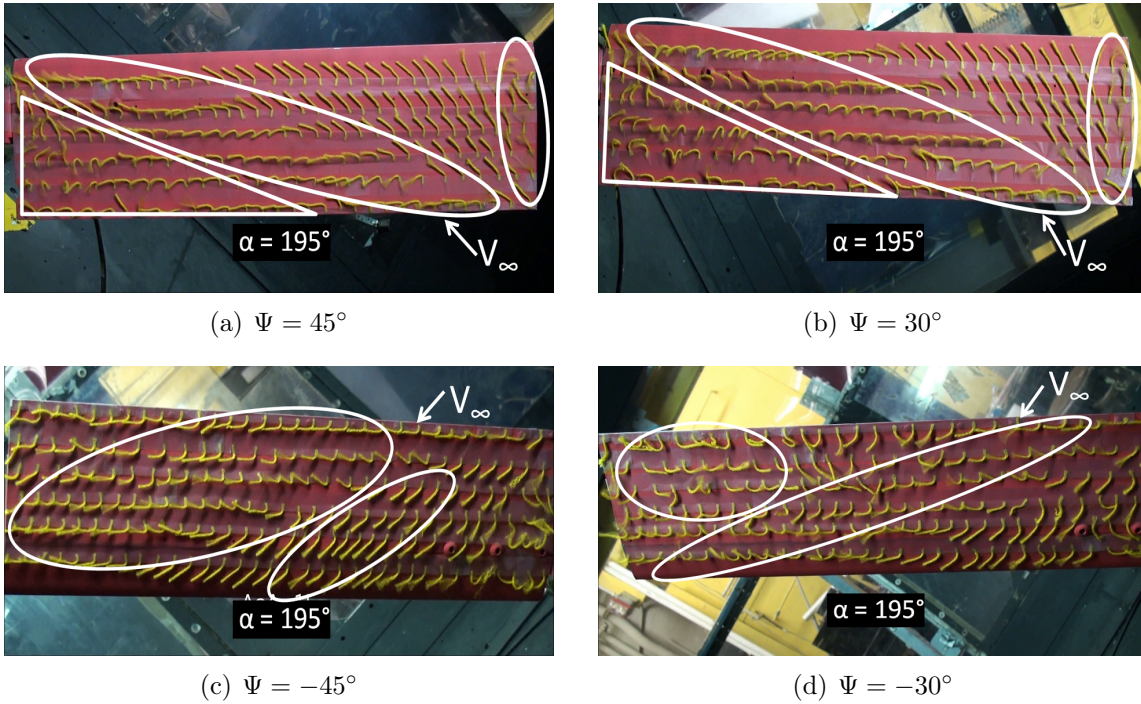


Figure 3.6: Tuft visualization at $Re = 3.0 \times 10^5$ and $\alpha = 195^\circ$

flow, vortex flow, and separated flow demarcated by the dashed lines (see Figure 3.7(a)). In this section, we present generalized flow topologies for a static backward yawed blade in the reverse flow regime (see Figures 3.7(b)–3.7(d)). Clearly, the surface flow topology for a backward yawed blade differs significantly from that for a forward yawed blade in reverse flow regime. Furthermore, unlike for a forward yawed blade the surface flow topology on a backward yawed blade also changes with yaw angle and angle of attack. At $\Psi = -30^\circ$ the surface flow topology consists of the familiar vortex and attached flow in addition to regions of span-wise flow in direction opposite to the expected span-wise flow. In the case of $\Psi = -30^\circ$ the flow topology also changes with angle of attack as observed from Figures 3.7(c)–3.7(d). The effect of yaw angle of the flow topology is observed by comparing Figure 3.7(b) to Figures 3.7(c)–3.7(d). At the time of this writing about the tuft visualization it was not clear what caused these flow topology variations at the various conditions. Global velocity field measurements, converted to static pressure distributions, did shine some light on this behavior in the rotor case.

In addition, proposed flow topologies for a rotor blade in backward yaw in the reverse

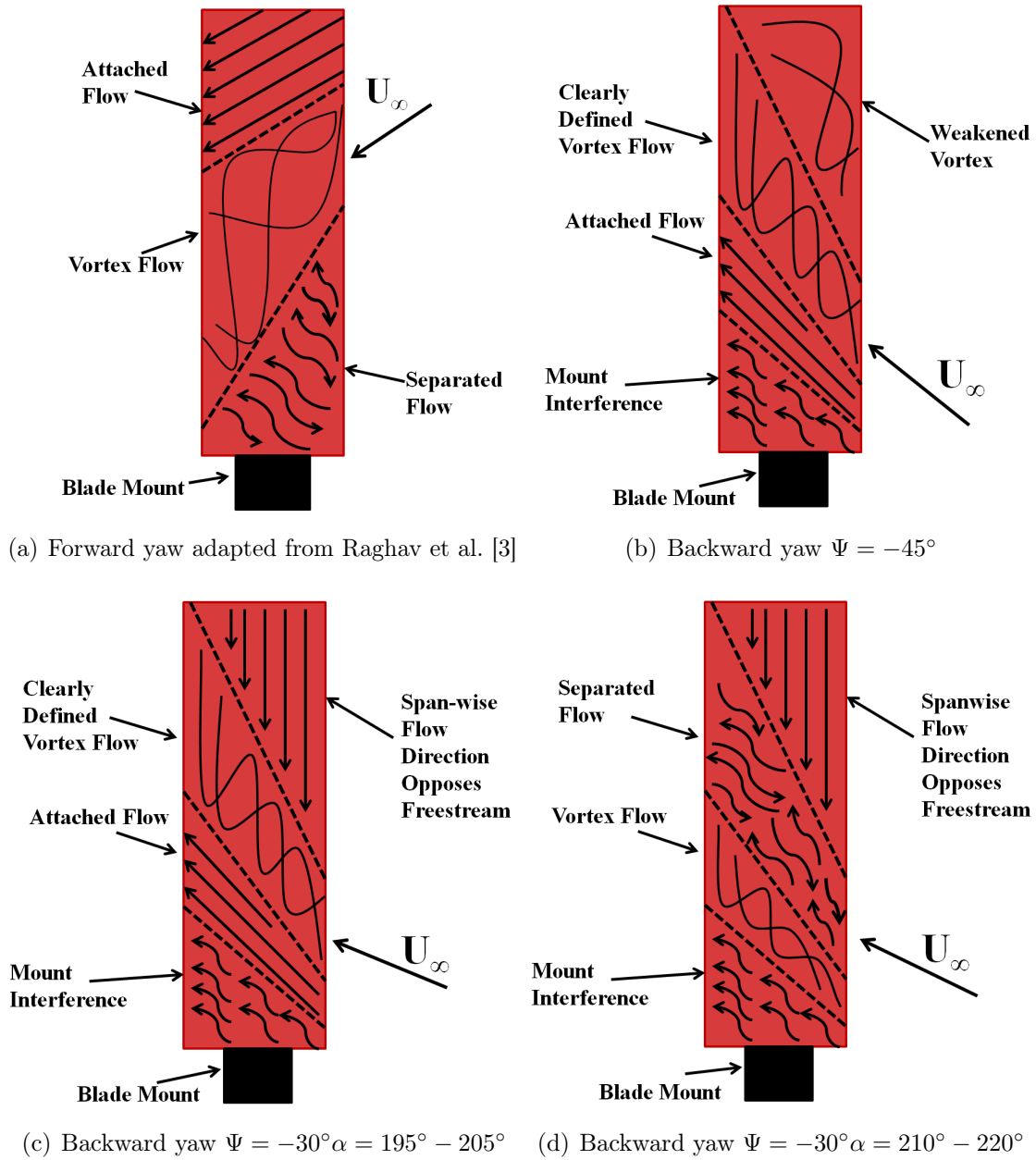


Figure 3.7: Proposed Flow Topologies for a Rotor Blade in Reverse Flow

flow regime are depicted in Figure 3.7(b)–3.7(d)

Given that the forward yaw flow topology regimes are fairly comparable over the range of yaw angles, it is amenable to be used for further analysis of the physics of the flow field. In this section we further analyze the variations in the flow topology for the forward yawed static blade at two different yaw angles as the angle of attack of the blade changes. We first present the variations in the area occupied by the different flow regimes with angle of attack followed by the analysis of the data.

The backward yaw flow topology shows some similarities to the forward yaw flow topology: there is a region of attached flow where the freestream flow first makes contact with the blade and a region of vortex flow immediately adjacent to it. A key difference between the two flow patterns is that the backwards yaw case has a region of fairly orderly flow bordering the far edge of the vortex flow region while the forward yaw topology features a region of chaotic, separated flow. In forward yaw the blade mount forms a strong adverse pressure gradient which may accelerate vortex breakdown, but in the backward yaw case the leading edge vortex does not encounter such an obstruction and is allowed to grow larger. It is important to note that the flow visualization observed at $\Psi = 30^\circ$ did not follow the prescribed flow pattern and showed a spanwise flow direction that opposed the freestream flow.

Figures 3.8(a) and 3.8(b) illustrate the variation of the area occupied by each flow regime as a function of angle of attack for forward yaw angles at $Re = 1.7 \times 10^5$. An insignificant portion of the blade area ($<10\%$) is typically occupied by the tip vortex interaction region and has not been presented in the figures. The salient features of each flow regime are clearly observed in the figures: *a)* for $\Psi = 30^\circ$ the attached and vortex flow regimes monotonously decrease with an increase in angle of attack, while the unattached flow increases with angle of attack. *b)* At $\Psi = 45^\circ$ the attached flow still exhibits a monotonous decrease with increase in angle of attack, however, the vortex and unattached flow regimes reach an equilibrium as angle of attack increases.

In order to further understand the behavior of the flow regimes with change in yaw angle and angle of attack, we shall consider the classical vorticity transport equation for an incompressible, barotropic fluid with conservative body forces [51]. The following equations are defined as per the blade fixed coordinate axes defined in Figure 2.1:

$$\frac{\partial \boldsymbol{\omega}}{\partial t} = -\mathbf{v} \cdot \nabla \boldsymbol{\omega} + \boldsymbol{\omega} \cdot \nabla \mathbf{v} + \nu \nabla^2 \boldsymbol{\omega} \quad (3.3)$$

where the term representing the diffusion of vorticity due to viscous effects, $\nu \nabla^2 \boldsymbol{\omega}$, can be neglected based on the argument that the Reynolds number is sufficiently high. In addition, for simplicity of the argument if we neglect the vortex stretching/tilting

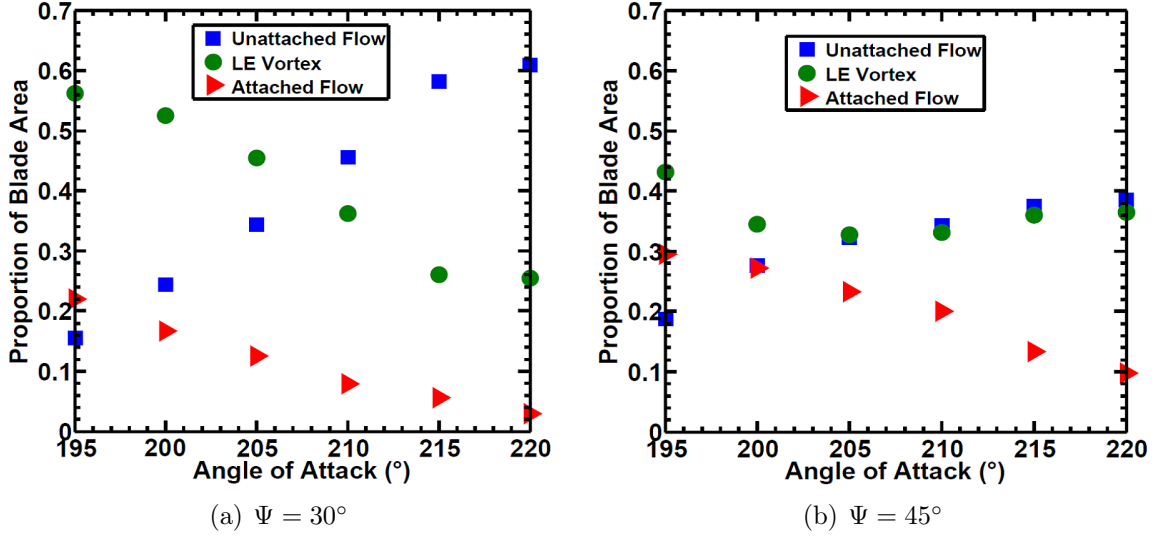


Figure 3.8: Proportion of blade area occupied by the different flow regimes as a function of angle of attack at $\text{Re} = 1.7 \times 10^5$

term, $\boldsymbol{\omega} \cdot \nabla \mathbf{v}$, we arrive at a balance between span-wise vorticity (ω_z) production and advection terms, such that:

$$\frac{\partial \omega_z}{\partial t} + u \frac{\partial \omega_z}{\partial x} + v \frac{\partial \omega_z}{\partial y} + w \frac{\partial \omega_z}{\partial z} = 0 \quad (3.4)$$

From the surface flow visualization it can be clearly observed that the tufts indicate a predominant span-wise velocity w , with negligible velocity in the x_b and y_b directions u and v . The only terms that remain in equation 3.4 are the vorticity production term and the advection term in the z_b direction, such that $\frac{\partial \omega_z}{\partial t} + w \frac{\partial \omega_z}{\partial z} = 0$. Considering this simplified vorticity transport equation, it can be postulated that for greater yaw angles, an equilibrium state can be achieved as long as the vorticity produced at the leading-edge is rapidly advected away in the span-wise direction. This argument is now used to justify the equilibrium state that is achieved at the greater yaw angle $\Psi = 45^\circ$ as observed in Figure 3.8(b) when compared to the lower yaw angle $\Psi = 30^\circ$ as observed in Figure 3.8(a). At $\Psi = 45^\circ$ the expected span-wise velocity is greater (by virtue of higher yaw angle) than at $\Psi = 30^\circ$ and hence the equilibrium state is easily achieved. It should be noted that equation 3.3 does not include the term that accounts for destruction of vorticity due to annihilation. The influence of annihilation on the reverse flow aerodynamics is yet to be ascertained from quantitative flow field

measurements.

3.6 Yawed Rotor Blade Held Stationary

Velocity field measurements using stereo particle image velocimetry are used to examine the sharp-edge vortex forming under a rotor blade in reverse flow. Comparisons with load measurements and surface tuft visualization show the similarities and differences between the rotor blade case and a swept wing in reverse flow. The fixed wing case is amenable to analysis using the Polhamus suction analogy, and exhibits vortex bursting. The rotor case shows the added effects of radial acceleration.

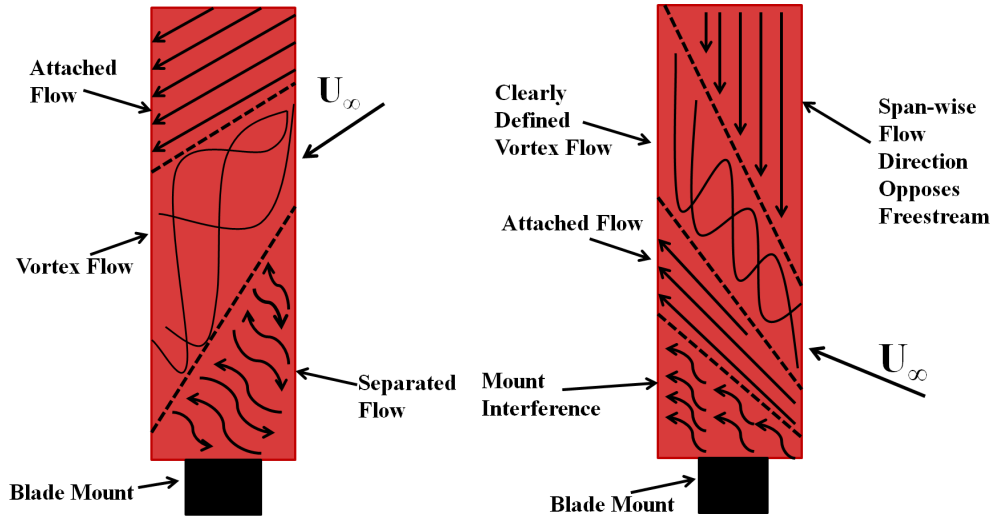
These are correlated with earlier fixed-wing aerodynamic loads and flow visualization studies on the same rotor blade operated in forward and reverse facing yaw in the wind tunnel. The blade is also held fixed at several rotor azimuths and angles of attack to ascertain the rotation effects on the flowfield. The circulation of the reverse flow attached vortex is of the same order of magnitude as the bound circulation of the airfoil section, suggesting that the vortex makes a significant lift contribution.

This section presents SPIV data for a static yawed blade in reverse flow by exploring the effects of reverse flow on rotating rotor blades in the John Harper 2.13m×2.74m low speed wind tunnel. Stereoscopic particle image velocimetry data are used to acquire three dimensional velocity field measurements.

3.6.1 Instrumentation

All experiments were performed in the 2.13m×2.74m John Harper wind tunnel at the Georgia Institute of Technology. The rotor blade used to collect SPIV data for the static experiments is an untwisted, rectangular blade with a NACA 0013 planform. A picture of the rotor blade used in the static experiments is shown in Fig. 2.1. See Raghav et al. [3] for a detailed description of the static yawed blade setup. The rotor used in the rotating experiments is composed of two untwisted, rectangular, NACA 0013 rotor blades (identical to the one used in the static experiments) attached to a teetering rotor hub turned by a 3.73kW motor. A CAD model of the rotor setup and laser sheet is shown in Fig. 3.11, and a close-up picture of the rotor blade and laser arm is shown in Fig. 3.10. Rotor parameters are displayed in Table 3.3.

Tunnel speed was set by gauging the dynamic pressure and ambient pressure and



(a) Topology on Forward-Swept Wing, Reverse Flow (b) Topology on Backward-Swept Wing, Reverse Flow

Figure 3.9: Topology of vortex flow over a fixed wing in reverse flow, with forward and reverse sweep. From Raghav et al. [3]

temperature. Dynamic pressure was measured using a Baratron pressure transducer connected to a Pitot-static probe in the test section. The angular velocity, Ω , of the rotor was measured using a photoelectric sensor.

TPP images were collected using high-definition cameras aligned with the rotor hub plane. Alignment was performed using a laser balance and a digital protractor. A camera was mounted on a heavy tripod two rotor diameters downstream of the rotor and set at 0° inclination using the digital protractor. The laser balance was used to set the height and yaw of the camera so that its lens was directly pointing at the center of the rotor hub. Another camera was mounted outside the tunnel test section at the rotor azimuthal angle of $\Phi = 90^\circ$. This camera was also aligned with the center of the rotor hub using the same method as before. A calibration board was used to correlate pixel length with physical distance in the plane of the rotor.

Illumination for PIV was provided by a Nd:YAG laser with a pulse energy of 200mJ. The laser was double pulsed to produce 532nm visible light. A laser arm was used to deliver the beam to the measurement plane by creating a light sheet with a thickness of 2mm. The flow was seeded with $10\mu\text{m}$ droplets generated using a Laskin-nozzle

aerosol generator. PIV images were captured by a ImagerIntense CCD camera with a 1600×1200 pixel viewing area. The CCD sensor had a scan rate of 16 Hz. The cameras and laser unit were synchronized using a programmable timing unit.

Table 3.3: Rotor Parameters

Parameter	Value	Units
Blade mass total	1.747	kg
Blade span	0.622	meter
Blade chord	0.178	meter
Blade aspect ratio	3.49	
Airfoil	NACA 0013	
Disc radius	0.889	meter
Solidity	0.0895	
Precone	1.6	deg
Motor	3.73	kW
Height	1.298	meter

3.6.2 Flow and Test Conditions

The test cases are summarized in Table 3.4 and described below:

1. The first test collected images of the TPP at $\mu = 0.6, 0.8$ and 1.0 corresponding to $\Omega = 31.4 \text{ rad/s}$ and varying freestream speeds. Images were collected using high definition cameras placed downstream of the rotor at $\Psi = 0^\circ$ and to the side of the rotor at $\Psi = 90^\circ$. This test established flow conditions that could be used for future PIV tests.
2. The second test measured the chordwise velocity field on a static rotor blade in reverse flow using PIV. A Reynolds number of 0.63×10^5 was chosen to match the effective Reynolds number of a subset of the rotating measurements. A test was also performed at $Re = 1.70 \times 10^5$ for comparison to previous flow visualization performed on a static yawed blade. Angles of attack were chosen to match the effective angle of attack of the rotating blade at the same yaw angle.

Table 3.4: Test Matrix For Experiments

Test	Data Acquired	Conditions
1	TPP Orientation	$\mu = 0.6, 0.8, 1.0, \Omega = 31.4rad/s$
2	PIV Static Blade	$\alpha = 191.2^\circ, 192^\circ, 195^\circ$ $\Psi = 30^\circ Re = 0.63 \times 10^5, 1.70 \times 10^5$
3	PIV Rotating Blade	$\alpha = 192^\circ \Psi = 240^\circ, 270^\circ,$ $\mu = 0.8, 1.0 Re = 0.63 \times 10^5$

3. The third test acquired phase locked PIV measurements on a rotating rotor blade at advance ratios of $\mu = 0.8$ corresponding to $\Omega = 20.93rad/s$ and $\mu = 1.0$ corresponding to $\Omega = 15.7rad/s$. Measurements were made at the radial location of $r/R = 0.5$ and phase locked at $\Psi = 240^\circ$ and $\Psi = 270^\circ$ equivalent to $\Psi = 0^\circ$ and $\Psi = 30^\circ$ for the static blade.

3.6.3 Data Acquisition/Processing

TPP orientation was determined by measuring lateral and longitudinal tilt of the rotor disc using TPP images. TPP tilt was measured by using an image processor to calculate the horizontal and vertical pixel position of the far ends of the rotor hub and performing an inverse tan operation.

Davis 7.2 software by LaVision was used to process the PIV data. Particle velocities were calculated from the spatial stereoscopic cross-correlation of the images. A 64×64 pixel interrogation window with 50% overlap and a second interrogation pass with a reduced window size (32×32 pixel) was used to yield a vector spatial resolution of 1.37mm which translates to 0.0008c. Post-processing of the vector images consisted of applying a median filter and light vector smoothing (3×3) for better visual presentation.

3.6.4 Averages flow field results

All of the velocity vector fields presented are fixed in the wind tunnel coordinate system and have not been corrected for the blade pitch angle. The right hand coordinate system for the vector field is established so that the positive y axis is out

of the plane and negative radial (spanwise) velocity indicates a flow directed toward the root of the blade. All dimensions are normalized by the chord length, where $x/c = 0$ corresponds to the geometric leading edge of the blade and $x/c = 1$ is the geometric trailing edge of the blade. The blue regions in the velocity field figures correspond to areas where PIV data were not collected.

Static Blade

The main motivation for performing PIV chordwise velocity measurements on the static blade in reverse flow is so that direct comparisons can be made to measurements taken on the rotating blade. Therefore, as stated in the ‘Flow and Test Conditions’ section, Ψ , α , and Reynolds number were chosen to match conditions present on the rotating blade. One test was also performed to match conditions for the tuft flow visualization performed by Raghav et al. [3] on the same static blade configuration. All static PIV tests were performed at $\Psi = 30^\circ$, which corresponds to the blade being yawed into the flow (see Fig 2.1 for the definition of positive Ψ).

Figure 3.12 - 3.14 illustrates the time averaged velocity vector overlaid on contours of vorticity at $\Psi = 30^\circ$, $\alpha = 191.2^\circ - 195^\circ$, and $Re = 0.63 \times 10^5$ and 1.70×10^5 . The velocity field data taken at $Re = 1.70 \times 10^5$ and $\alpha = 195^\circ$ corroborate the attached vortex seen using tuft visualization by Raghav et al. [3] at the same conditions. All of the velocity fields confirm the existence of an attached vortex in reverse flow over a static yawed blade. Note that the contours of vorticity for each velocity field have different color scales, so the strength of the attached vortex is increasing with α .

The SPIV data collected in these experiments allows for interpretation of the radial component of velocity. Figure 3.15 shows the time averaged velocity vectors overlaid on the time averaged radial velocity component (U_r positive for out of plane). The radial component of velocity is primarily directed into the plane of the paper, indicating a spanwise flow towards the blade root. This result is expected for a blade yawed into the flow and agrees with the tuft flow visualization for a static reverse flow blade presented by Raghav et al. [3]. The radial velocity has a lower magnitude close to the surface of the blade and increases further away from the blade surface. This radial velocity field can be used to analyze the effect of rotation on reverse flow, where it is expected to predominantly affect the radial velocity component due to additional centrifugal effects.

3.7 Exploratory Measurements Under the Rotating Blade

In conjunction with the yawed-blade tests above, a few exploratory tests were performed with the rotor rotating. While an attempt was made to 'match' flow conditions as closely as practical with the rotating blade, the comparison is very rough, as there is no spanwise variation of the relative freestream or the induced angle of attack. Thus these experiments merely attempted to glimpse what the velocimetry would show in the same stations were the yawed fixed blade was held.

Figure 3.16 shows the time averaged velocity vectors overlaid on the time averaged radial velocity component for a rotating rotor blade at $\mu = 0.8$, $\Omega = 20.93\text{rad/s}$, and $r/R = 0.5$ phase locked at $\Psi = 240^\circ$ (equivalent to a static rotor blade at $\Psi = 30^\circ$). The radial velocity has a positive value (corresponding to flow directed from the root to the tip of the blade) near the blade surface due to reactive centrifugal forces that arise due to rotation. The radial velocity becomes negative farther from the blade surface, as the radial stress driving the radial flow does not extend far above the blade surface. A comparison of Fig. 3.15 and Fig. 3.16 demonstrates the effect of rotation on the radial component of velocity in reverse flow. A comparison of Fig. 3.13 and Fig. 3.17 suggests that the additional radial velocity due to rotation delays the separation at the effective leading edge (geometric trailing edge) at similar flow conditions.

With the collective and cyclic pitch settings of $\theta_0 = 6^\circ$ and $\theta_s = -6^\circ$, separation at the effective leading edge was not observed until $\Psi = 270^\circ$ (equivalent to a static blade at $\Psi = 0^\circ$). Fig 3.18 shows an attached vortex on the lower surface of the blade. To clearly visualize the vortex, the freestream velocity ($U_\infty = 14.88\text{m/s}$) was subtracted from the velocity field. The circulation of the vortex (Γ_V) was computed using Stokes theorem and determined to be $0.354\text{m}^2/\text{s}$. The circulation of this vortex was compared to the maximum bound circulation (Γ_a) of the "airfoil" section of the wing. The bound circulation was computed using Eq. 3.5:

$$\Gamma_a = \frac{1}{2}U_\infty c C_{Lmax} \quad (3.5)$$

where c is the chord length and C_{Lmax} is the maximum static coefficient of lift taken from aerodynamic loads measurement data presented by Raghav et al. [3]. The computed bound circulation was $0.392\text{m}^2/\text{s}$, which was slightly higher than the circulation of the vortex at the trailing edge. The fact that the circulation in the

vortex is of the same order of magnitude as the bound circulation could imply that the attached vortex which develops on the lower surface of the blade in reverse flow makes a significant lift contribution.

Following are the time averaged streamlines obtained at $r/R = 0.5$ and $\text{yaw} = 240$ degrees. The figures for cases $\mu = 0.8$ and 1.0 show rotor speed subtracted stream lines and trailing edge vortex.

The last three plots correspond to fixed μ of 0.85 and r/R is changing from 0.4 to 0.5 to 0.6 . The plots are obtained after subtracting the rotor cord wise velocity in X direction and the free stream velocity in Z (direction perpendicular to the illuminated plane). Here we observe that as we go to higher r/R , the vortex strength is decreasing (because the reverse flow is decreasing as μ is constant). The other observation is that the in-plane velocity in the vortex region decreases with increase in r/R due to centrifugal effects.

As mentioned before, these were exploratory measurements. They do show that there are vortical structures to be seen under the rotating blade.

Conclusions from Fixed Wing Experiments

An NACA003 rotor blade was first used as a fixed wing in a wind tunnel, with air loads measured at angle of attack, at various forward and backward sweep angles in both forward and reverse flow at various Reynolds numbers. These measurements suggested the presence of substantial amounts of vortex lift. Lift curves, drag polars, and pitching moments were analyzed from low-pass filtered, multi-axis load cell data. The Polhamus suction analogy for delta wings was adapted for application to a yawed rotor blade, and the predictions from the mathematical model were compared to experimental results. Tuft visualization was performed at various yaw angles and Reynolds numbers to reconcile the aerodynamic loads data. Surface tuft visualization showed dramatically different vortex flow topologies under forward and reverse sweep, and forward-facing versus reverse-facing flow. Vortex bursting appeared to be occurring.

The blade was then returned to a 2-bladed teetering rotor setup. It was initially held fixed at various azimuths to obtain the velocity field under the blade in reverse flow using stereo particle image velocimetry. The rotor was next operated at advance ratios from 0.8 to 1.0 . Velocity measurements have been completed at several locations at 270 degrees azimuth and 240 degrees azimuth. Other azimuths are to be investigated

a well. The rotating rotor velocity field dramatically confirms the formation, growth and bursting of a sharp-edge vortex at the 240 degrees azimuth. The strong velocity along the rotor radius, directed inboard along the core of the vortex at 240 degrees azimuth, is reminiscent of delta wing / strake vortices. It appears to burst, with a sudden growth of the core and decay and spread of the radial velocity.

Pitching moment data under fixed wing conditions confirmed the role of the vortex in moving the center of pressure. In the rotating flow case, the circulation in the sharp-edge vortex is again found to be substantial and of the same order as the overall bound circulation over the airfoil section, and thus bound to cause first-order effects on the pitching moment of the blade. The results have thus conclusively proven the existence of strong vortex lift characteristics in the aerodynamics of a blade in reverse flow. The conclusions are enumerated in summary below:

1. The reverse flow lift curve slopes were higher than the corresponding regular flow lift curve slopes at forward yaw angles. The reverse flow lift curve slopes at backward yaw angles were lower than the reverse and regular flow lift curve slopes at forward yaw angles and did not follow the expected $\cos^2\Psi$ fit. The observed flow behavior of the backward yaw cases also differed significantly from the forward yaw cases. The lift asymmetry between the forward and backward yaw angles could affect trim conditions in very high advance ratio flight. It is important to note that mount interference could have influenced test results for the backward yaw angle cases, which represent a helicopter blade in the rotor azimuth regime $\Psi \geq 270^\circ$.
2. The lift predictions made by the Polhamus delta wing equations showed excellent correlation with experimental results at forward yaw angles of $\Psi \geq 30^\circ$. The Polhamus equations showed fair correlation at $0^\circ \leq \Psi < 30^\circ$, which is to be expected. The ability of the Polhamus equation to accurately predict static loads in the reverse flow regime set the stage to separate out the effects of rotation, from experiments on a rotating blade.
3. Drag polars showed that the regular flow regime produced higher L/D values than the reverse flow regime for the yawed rotor blade. Pitching moment data suggests that the chordwise center of pressure is near $0.75c$ in the reverse flow regime. The larger aerodynamic loads in the reverse flow region (as evidenced by the higher lift curve slopes) coupled with this shifted center of pressure would result in high torsional loads and pitch link loads during flight in the reverse flow regime.

4. Surface tuft flow visualization showed strong evidence of an attached leading edge vortex in the reverse flow regime. The vortex size was strongly dependent on the angle of attack and correlated well to the aerodynamic loads observed at the same yaw angle. The attached vortex contributes to higher blade loading in the reverse flow regime. The position and shape of the attached vortex closely resembled the “reverse-chord dynamic stall” vortex predicted by CFD for the slowed UH-60 rotor test [20]. This suggests that the vortex may not be an artifact of rotation.
5. The flow topology over the forward yaw blade in reverse flow has three main regimes: the vortex, attached and separated flow. The flow topology variation with yaw angle suggests that at greater yaw angle configuration the size of the attached span-wise vortex attains a maximum equilibrium value when compared to the lower yaw angle configuration. This observation is justified by using a vorticity transport analysis of the flow field.

3.7.1 Implications

The fixed wing experiments thus showed that this rotor blade would develop a sharp-edge vortex under reverse flow conditions. The blade aspect ratio is low, and this raises questions about the validity of the conclusions for helicopter blades that have much higher aspect ratio. However, these concerns are not justified, when one considers the nature of the rotor reverse flow problem in detail. For one thing, aspect ratio is not the primary issue here. The same blade could have been built with a much smaller aspect ratio, simply by reducing chord. That would not have changed the conclusion that the sharp-edge vortex would form; it would only have reduced the Reynolds number based on chord. Secondly, consider that in the case of a rotor, the region of reverse flow is generally limited to a part of the blade span. The highest reverse flow dynamic pressure is at the root. The point of zero chordwise relative velocity reaches the tip, at advance ratios less than 1, only at 270 degrees azimuth. So again, the region of reverse flow vortex is limited in practice. Even in full-scale flight, the reverse flow Mach number is small, so that incompressible-regime tests are entirely appropriate. What is the effect of the larger Reynolds number? Probably a tighter vortex, but if the aspect ratio is large, this vortex might again cover most of the blade, as is the case here. Were a small-chord blade to be used in these experiments, the larger-core, lower Reynolds number vortex might have spilled over the chord, and that would be unrealistic. Thus we argue that the choice of experimental parameters is fully justified by the results.

These experiments have thus proved the first part of the hypothesis: That a blade in reverse flow generates a sharp-edge vortex, much like the sharp edge of a delta wing at angle of attack. The experiments done with the blade held at expected rotor blade attitude, show that there is significant circulation in the vortex. Polhamus' suction analogy can be extended to calculate the vortex lift and the shift in center of pressure due to this vortex, and they are both significant. Now we can move to the next step. What will happen when the rotor blade is rotating? What are the special effects of rotation? Given our prior experience with studying the strong radial flow on rotor blade on the retreating blade side, radial flow effects were certainly uppermost in our minds as we ventured into this regime.

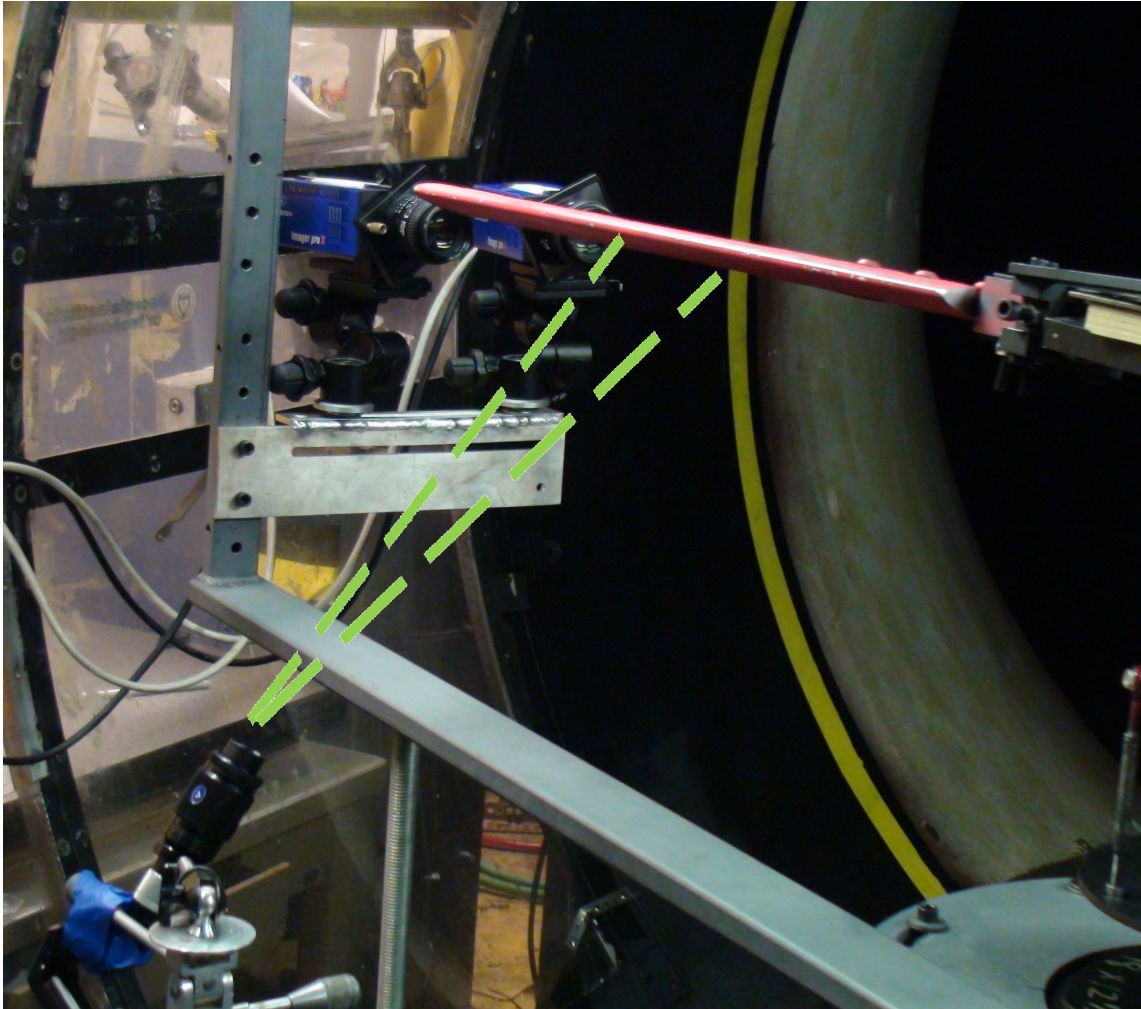


Figure 3.10: Photo of the Stereo PIV setup

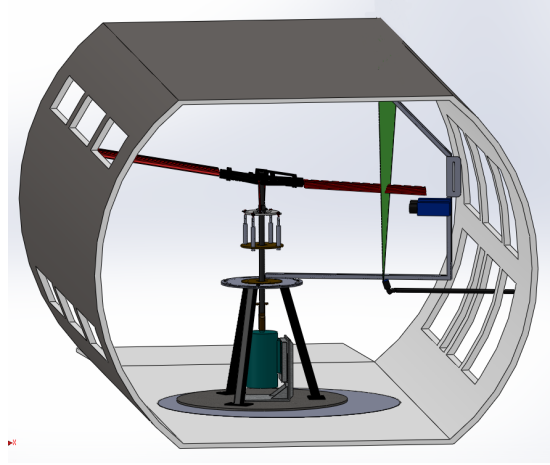
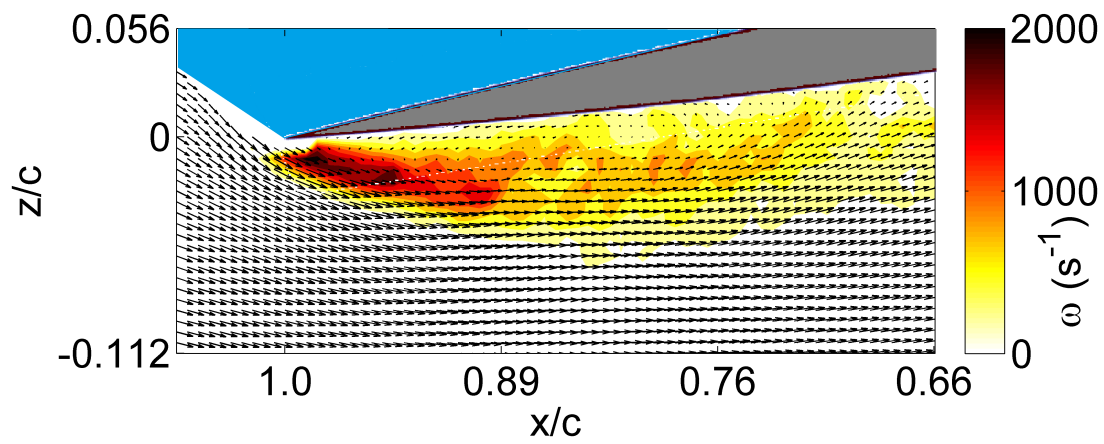


Figure 3.11: Test section as viewed from upstream

Figure 3.12: Static Blade at $\Psi = 30^\circ$, $\alpha = 191.2^\circ$, $Re = 0.63 \times 10^5$

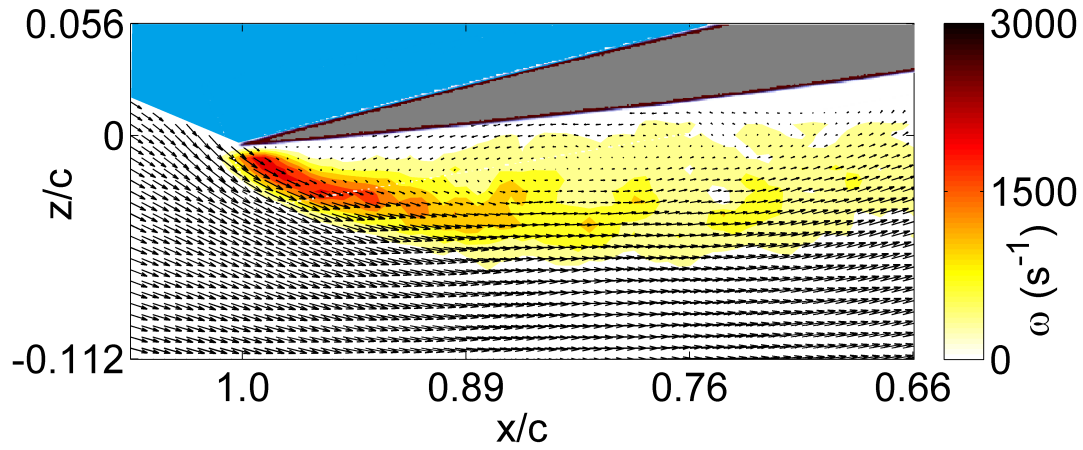


Figure 3.13: Static Blade at $\Psi = 30^\circ$, $\alpha = 191.2^\circ$, $Re = 0.63 \times 10^5$

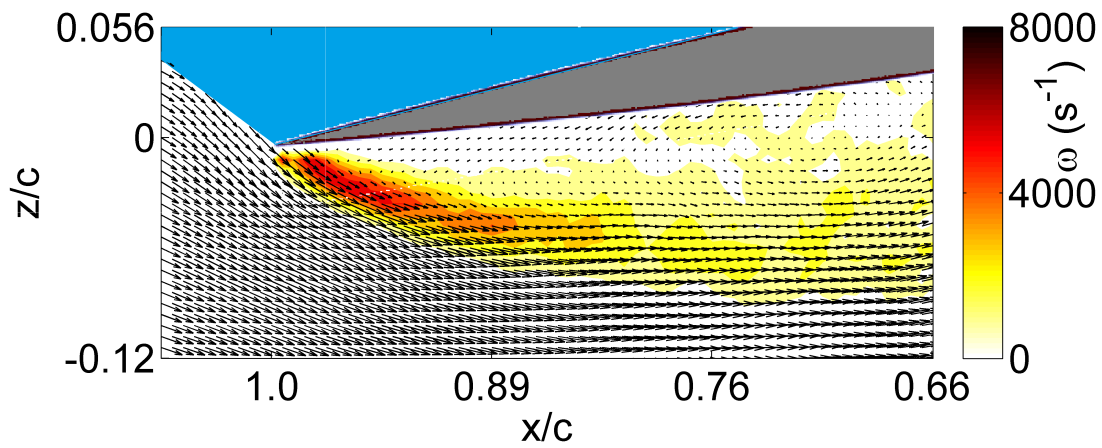


Figure 3.14: Static Blade at $\Psi = 30^\circ$, $\alpha = 195^\circ$, $Re = 1.70 \times 10^5$

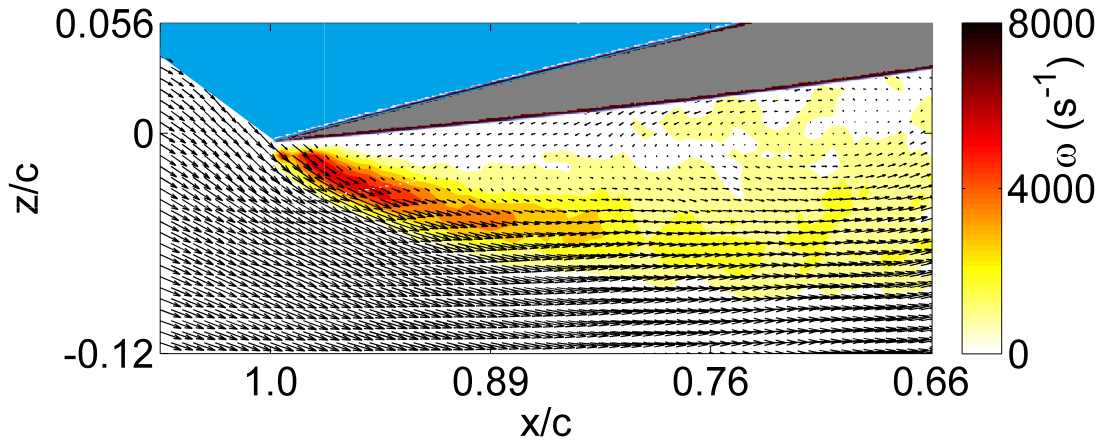


Figure 3.15: Radial flow on static blade at $\Psi = 30^\circ$, $\alpha = 192^\circ$, $Re = 0.63 \times 10^5$

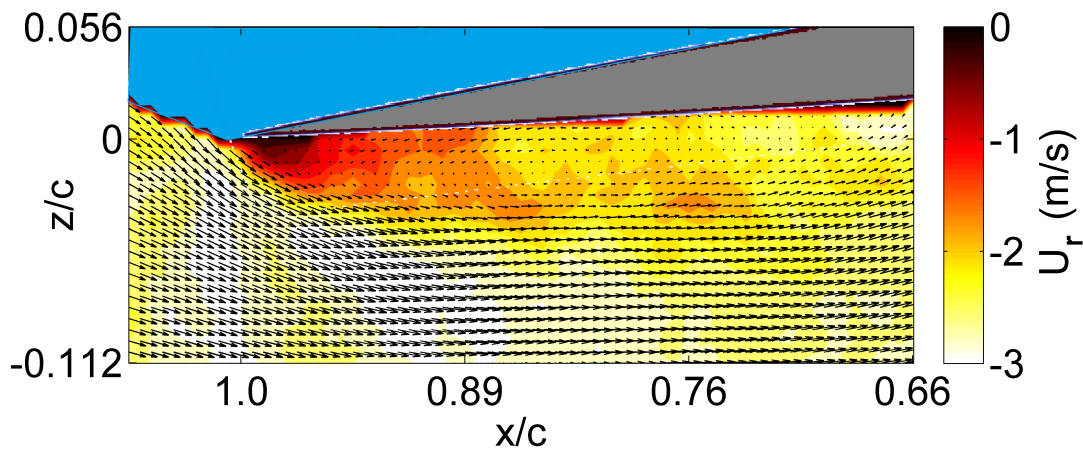


Figure 3.16: Radial flow under rotating blade at $\mu = 0_8$, yaw=240, $r/R=0.5$

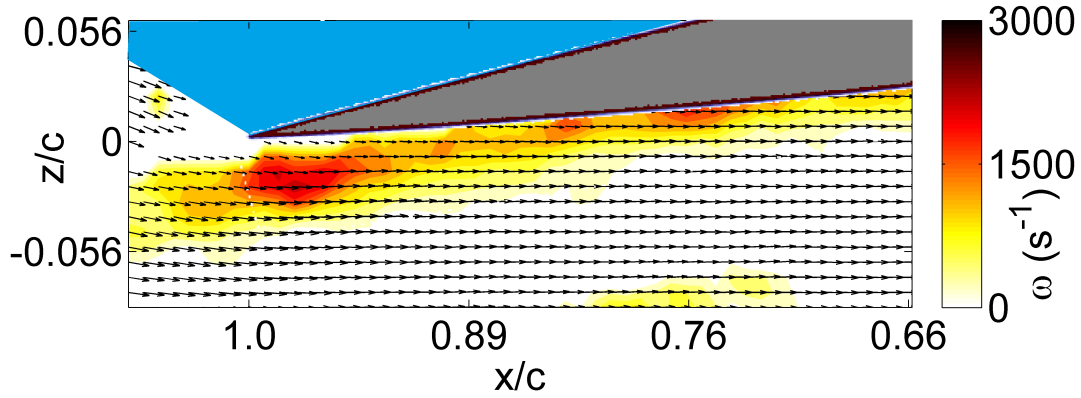


Figure 3.17: Vorticity Contours Under Rotating Blade At $\Psi = 240^\circ$, $\mu = 0.8$, and $\Omega = 20.93 \text{ rad/s}$ which yields $\alpha = 192^\circ$ and $Re = 0.63 \times 10^5$ at $r/R = 0.5$

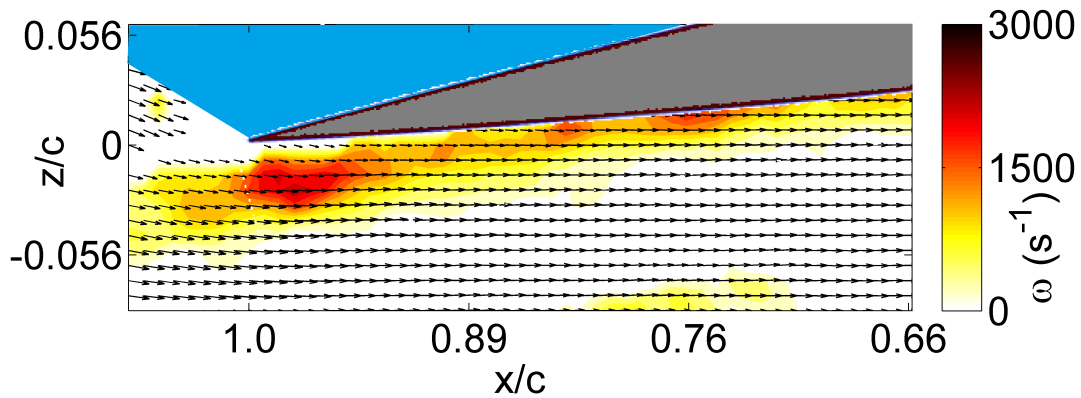


Figure 3.18: Vorticity Contours Under Rotating Blade At $\Psi = 270^\circ$, $\mu = 0.8$, and $\Omega = 20.93 \text{ rad/s}$ which yields $\alpha = 196^\circ$ and $Re = 0.635 \times 10^5$ at $r/R = 0.5$

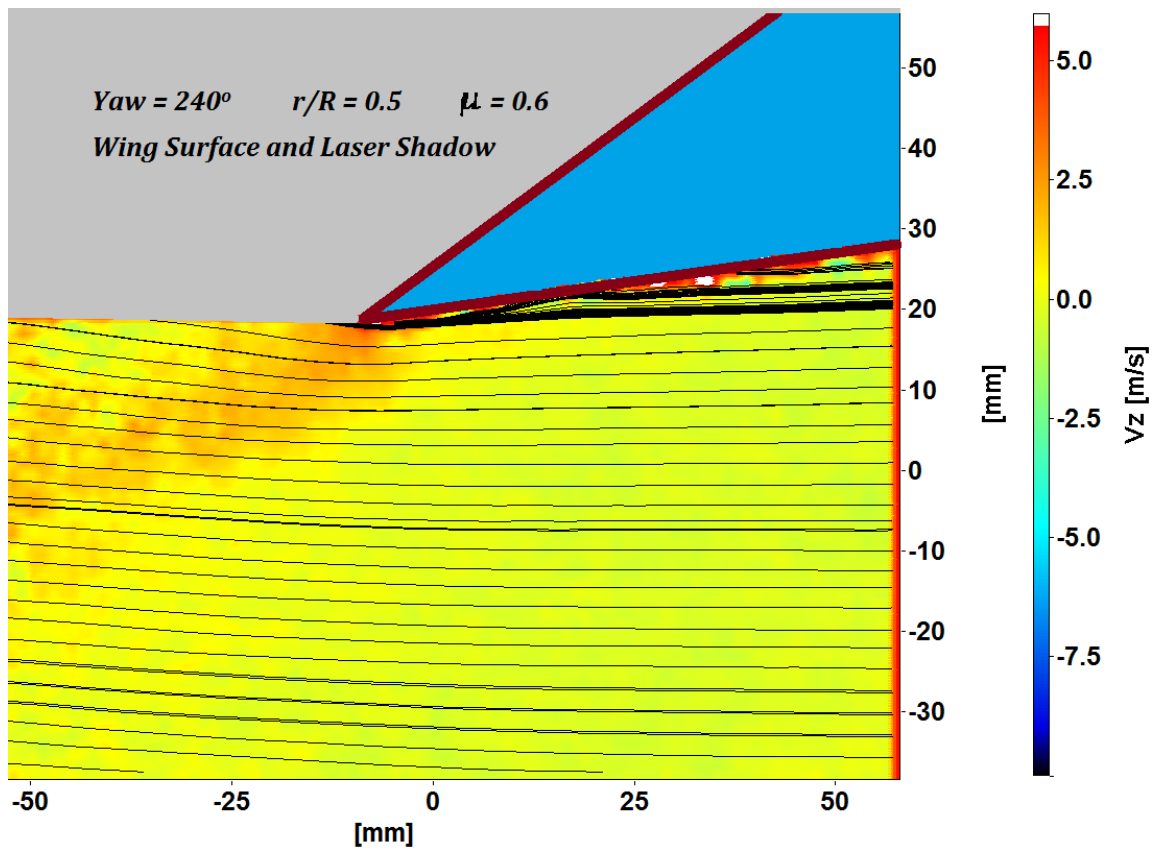


Figure 3.19: Yaw = 240, $r/R = 0.5$, $\mu = 0.6$, Local Reynolds No. = 1.14×10^5

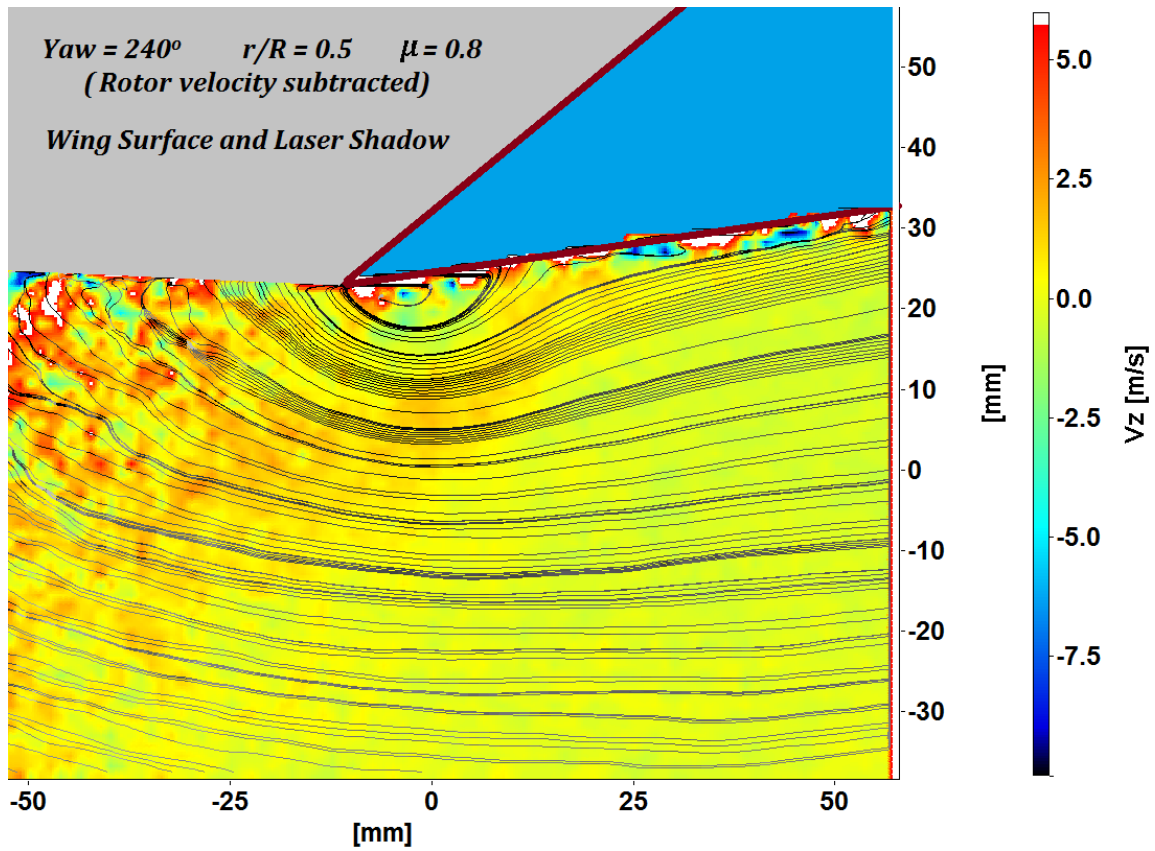


Figure 3.20: Yaw = 240° , $r/R = 0.5$, $\mu = 0.8$, Local Reynolds No. = 1.52×10^5 , Observed approximate circulation at vortex = $0.75 \text{ m}^2/\text{s}$

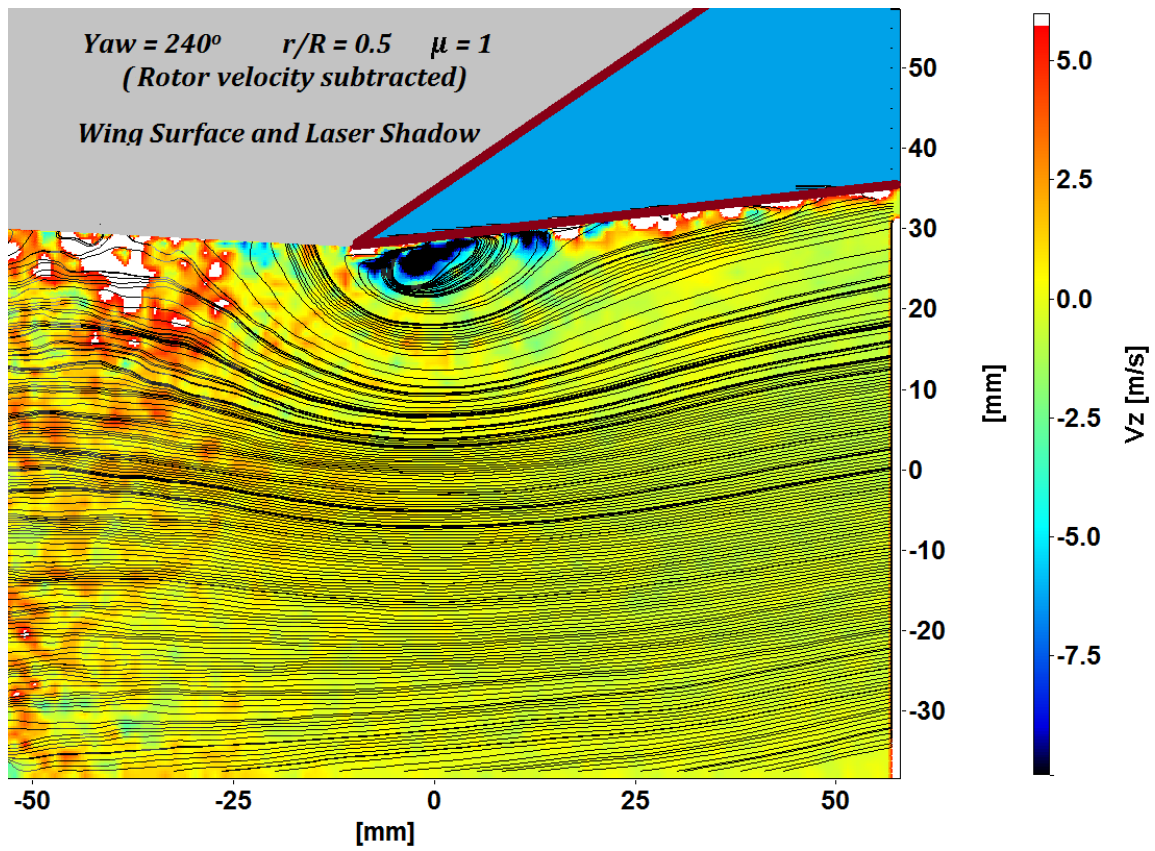
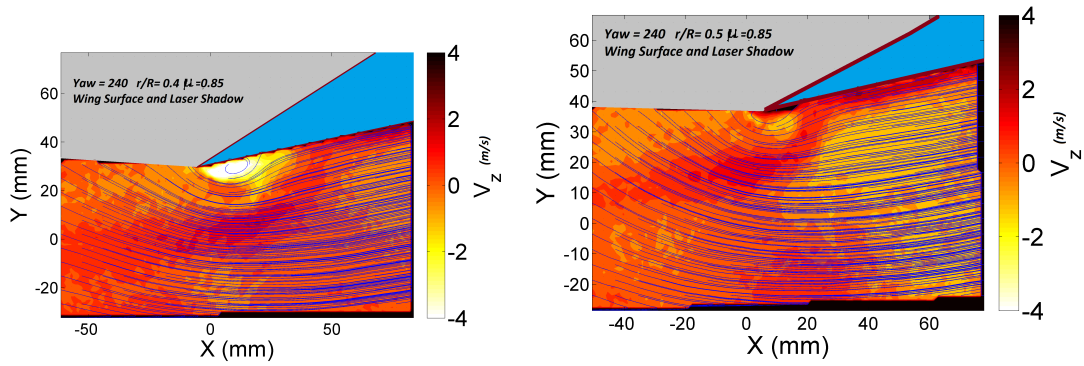
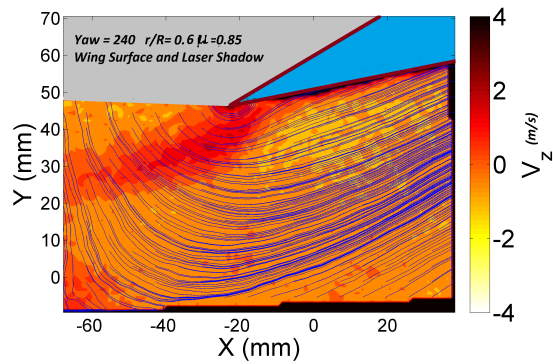


Figure 3.21: Yaw = 240, $r/R = 0.5$, $\mu = 1.0$, Local Reynolds No. = 1.89×10^5 , Observed approximate circulation at vortex = $1.44m^2/s$



(a) Yaw = 240, $r/R = 0.4$, $\mu = 0.85$, Rotor Speed = 200 RPM
 (b) Yaw = 240, $r/R = 0.5$, $\mu = 0.85$, Rotor Speed = 200 RPM



(c) Yaw = 240, $r/R = 0.6$, $\mu = 0.85$, Rotor Speed = 200 RPM

Figure 3.22: Radial variation of velocity field at a fixed advance ratio of 0.85, at 240 degrees azimuth

Chapter 4

Rotor Blade Results

4.1 Averaged flow field data

SPIV data presented here are averaged over 100 instances. All the streamline plots are fixed in the blade reference frame by subtracting the blade velocity from the averaged data. The contour plot in the background of the streamline figures depicts the out-of-plane velocity component (U_r). For clarity, the contribution of the free stream (due to yaw) in the out-of-plane direction has been removed from the U_r contour plot. The following equations show how the velocities in the plots have been modified.

$$U_{X,Blade} = U_{X,Lab} - rx\Omega \quad (4.1)$$

$$U_{r,contour} = U_{r,observed} + U_{freestream}x\text{Sin}(270 - \psi) \quad (4.2)$$

where $U_{freestream}$ is the wind tunnel flow speed. The right hand coordinate system has been used in all plots, so the positive r direction points out of the plot. Positive X direction points towards leading edge of blade. The region of streamline plots masked in blue represents the blade geometry and that masked in gray represents the region where data were not obtained due to laser shadow. The laser sheet, and thus the images, cut the blade perpendicularly in all cases.

4.1.1 Azimuth 240 deg.

At $\psi = 240$, the blade is in a 30-degree forward yaw condition. Figure 4.1 displays streamline plots at different sections along the blade at the $\mu = 0.85$ condition. All the plots (except that at $r/R = 0.7$) have a high strength vortex attached to the blade trailing edge. This closely resembles a forward swept, sharp edged wing at angle of attack. The vortex strength and into-the-plane velocity ($-U_r$) at the core of the vortex decrease with increasing r/R (moving towards the tip). One reason for this behavior is the decrease in reverse flow going from hub to tip due to the increase in tangential speed with r/R . The streamline plot at 0.7 r/R does not show any vortex because of negligible reverse flow at that section.

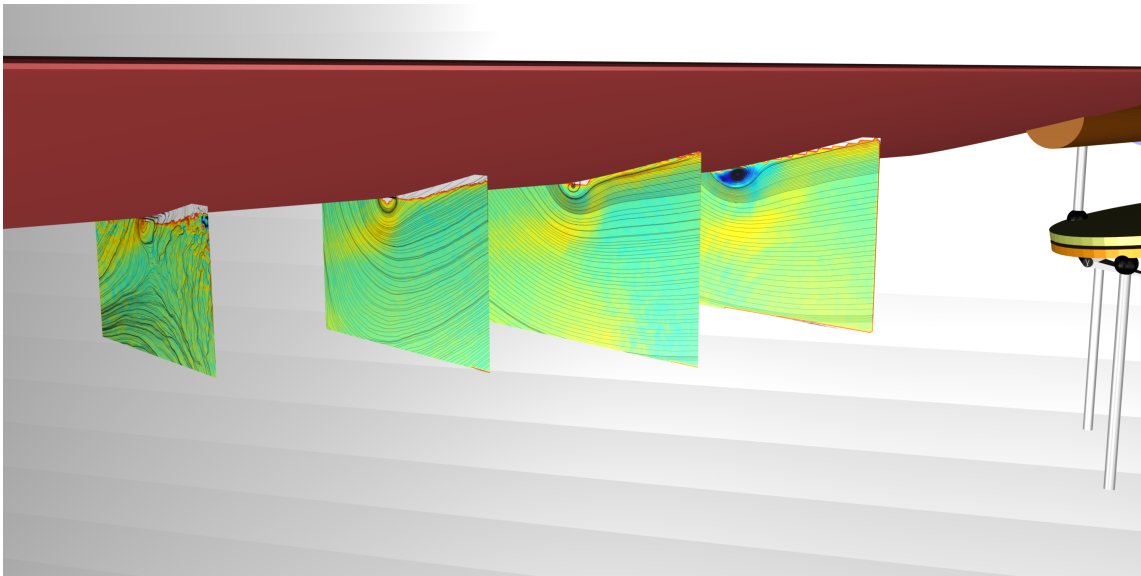


Figure 4.1: Streamline plots from SPIV near the sharp edge of the blade at different r/R at $\psi = 240$ and $\mu = 0.85$.

The increase in vortex strength parallels the rise in reverse flow with increase in μ as apparent from Figure 4.2. There is almost no reverse flow at μ of 0.7 at $r/R = 0.6$. High reverse flow near the root causes a tight, strong vortex. There is no vortex shedding observed at this azimuth.

At azimuth of 270 deg, the blade is at zero yaw. In Figure 4.4 All the sections feature a large vortical structure which is not centered near the trailing edge, unlike the cases at $\psi = 240$ deg. This structure is considerably clearer than what one might expect due to simple recirculation in separated flow. We can postulate that separated flow

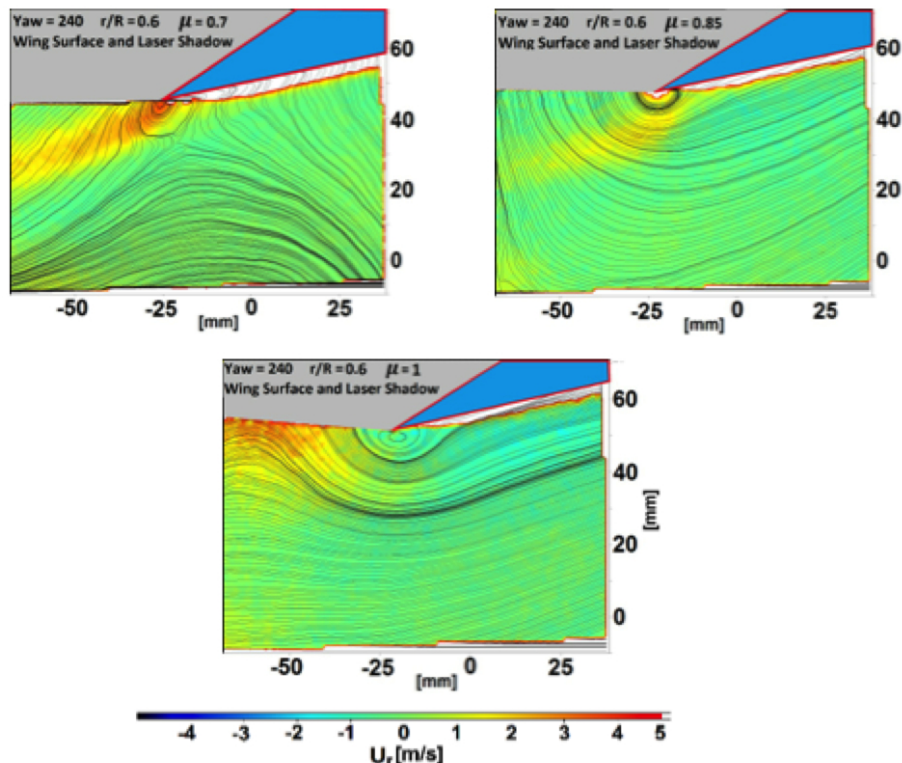


Figure 4.2: Streamline plots at r/R of 0.6 at $\psi = 240$ and $\mu = 0.85$.

does contribute to the strength of the vortex as it hits the vortex tangentially. The vortex shape is more well-defined at sections near the tip while they are not so near the hub. This vortex shape deformation is possibly due to high reverse flow strength in the region. Reverse flow in this case does not cause significant increase in vortex strength like in the case of $\psi = 240$ deg. as the blade is not in a yawed condition.

In Figure 4.4 with increase in μ , the vortex is further away from trailing edge in the flow direction. The streamline plots at μ of 0.7 and 0.85 with the vortex extending well below the blade edge, clearly refute models based on shedding from the blade. At $\mu = 1$, the vortical structure at $r/R = 0.6$ appears to be strong but confined very close to the blade surface. The overall finding of the vortex well below the blade edge suggests that the vortex is created at some ψ less than 270 deg. where the blade was in forward yaw position. The vortex is then convecting with the blade. The other observation is that the maximum negative radial velocity (U_r) is found to be at the location where the vortex touches the bottom of the blade for all cases at this ψ . This

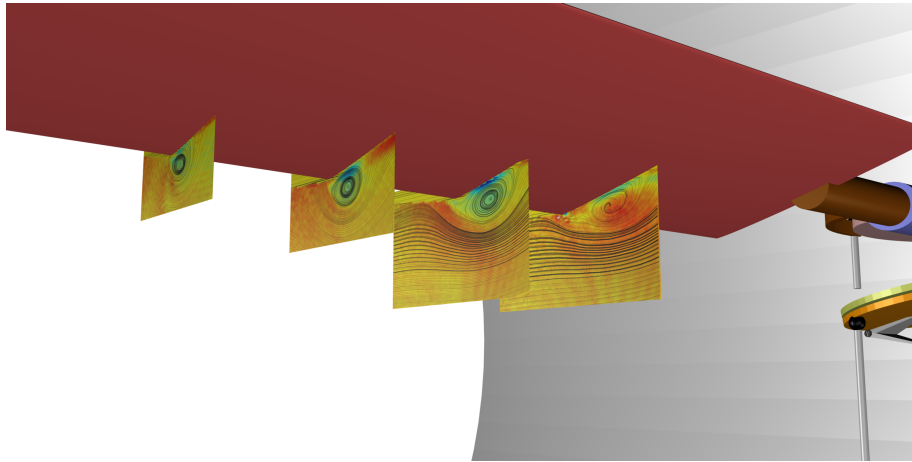


Figure 4.3: Streamline plots from SPIV near the sharp edge of the blade at different r/R at $\psi = 270$ and $\mu = 0.85$.

can be explained by considering the radial static pressure gradient along the radial direction: the vortex being stronger inboard, the static pressure near the surface is expected to be lower, so that there is a favorable gradient directed radially inboard. This would induce a radial velocity directed inboard, at the outer r/R locations, as seen. This postulate requires confirmation from static pressure data.

4.1.2 Azimuth 300 degrees

At azimuth of 300 deg., the blade is in a 30 degree backward- yaw condition. The streamline plots in Figure 4.6 resemble those at $\psi = 270$ deg. in terms of vortex shape, size and trends. Here too the vortex near the hub appears less distinct. Increasing μ leads to a trend similar to that at $\psi = 270$ deg. and the vortex loses its shape with increase in reverse flow (Figure 4.4). But this time, this effect is seen to occur for lower μ values. This indicates that the large vortical structures observed at $\psi = 270$ deg. are still present when the blade comes to $\psi = 300$ deg. However, they are not as strong now and are diffusing energy. In this case too, maximum negative values or U_r are found where the vortex interacts with the blade bottom surface.

4.2 Pressure Coefficient Contours

The velocity field measurements obtained from PIV data were used to find pressure coefficients in the flow field. Reference [52] gives the details of the process used. Figure 4.7 shows a pressure coefficient contour plot for the case of $\psi = 2700$, $r/R = 0.4$ and $\mu = 0.85$. Because the flow here is primarily incompressible and viscous effects are restricted to boundary and vortex core only, the C_p found using Bernoulli equation is not only an upper bound but also a fairly accurate estimate for most of the region.

The high values of negative C_p seen, indicate that the vortex is highly three-dimensional, having grown along its core, and must have been generated at an azimuth well ahead of 270 degrees. The highest negative values are seen near the surface, where the edge of the vortex core touches the blade. Figure 4.8 is the contour plot of C_p at the blade surface along the blade at $\psi = 270$ deg. obtained by interpolating the C_p distribution along blade surface at each section. The interpolation is highly jagged because of the sparse number of planes where SPIV data have been obtained. It shows that the highest negative surface pressures occur around x/c of 0.15 from the TE (x/c of 0.85 measured from the rounded edge of the blade), with this region moving diagonally out to the sharp edge at outboard locations. Again, this is consistent with the idea of the vortex having been formed along the sharp edge at an earlier azimuth, but convecting faster than the blade at the more inboard locations.

Figure 4.9 follows the discussion on pressure loss measured by Couette flow analogy as explained in [52]. It is observed that pressure loss as compared to freestream dynamic pressure is of the order of 10^{-4} . The seemingly low values of pressure losses validate the use of Bernoulli equation for initial best guess and accurate estimate for pressure field. Pressure losses along streamline near to vortex, measured as an artifact of shear stress, attain negative values in the vortex influenced regions and goes to zero as the streamline leaves the vortex. As a next step, the pressure loss may be refined further and can be used as a correction term to accurately predict the static pressures in the entire flow field.

4.3 Interpretation of Results

Figure 1.2 provides a simplistic illustration of the different predictive models seen in the literature. Due to probably oversimplification, we are not associating these with

specific references. The most basic method was to take airfoil data from 2D wind tunnel tests in the region around 180 degrees angle of attack, and correct the data for yaw with a sinusoidal correction, and if needed an aspect ratio correction. At the next level, with experiments revealing evidence of vortices in the flowfield, vortex shedding was postulated; both from the blunt edge when using NACA0012 type airfoils with blunt leading edges, and from the sharp edge as from a thin flat plate held at negative angle of attack. Karman vortex street analogues were also developed. These models have recently been adapted to include unsteady pitching effects, again from airfoil experimental data. Other studies with unswept airfoils have modeled the sharp-edge flow as a diffused, separated shear layer, with the blunt edge shedding vortices. Others have postulated a reverse dynamic stall process, explaining the occurrence of sharp pitching moments as well as strong vortices seen in the flowfield in experiments. At the bottom is our postulate: that the flow around and under a sharp, yawed edge behaves similarly to that around and over a sharp-edge delta wing or other highly swept wing at angle of attack. A strong, coherent, helical sharp-edged vortex is formed. Where this encounters an adverse pressure gradient, as near a hub, it can burst and lift away from the surface. The vortex-induced lift and pitching moment can be computed using Polhamus suction analogy, as well as models for vortex flows at higher angles of attack.

Comparing images from azimuths 240 (30 degrees forward yaw) with those from azimuth 300 (30 degrees backward yaw) reveals some of the effects of rotation and history. Figure 4.10 illustrates the difference in the onset velocity field between the fixed, yawed wing and the rotating wing. The vortex strength increases as one moves along the blade span. The first cause is the variation of freestream velocity and hence dynamic pressure. This effect implies a higher strength near the root in both cases, since the reverse flow dynamic pressure is highest at the root. In analysis, this effect can be easily included to a model based on 2-D airfoil aerodynamics.

The second effect is the \hat{O} integrating \tilde{O} effect along the blade span. This is a nonlinear effect of yaw, and is related to the flow around the leading edge of a delta wing or high swept wing. At any given section of such a wing, the vortex observed is due to vorticity generated by that section as well as the vorticity in the shear layers rolling up over the edge at sections upstream of the one being observed. Thus the attached vortex observed at a section can be thought of as due to \hat{O} integrated \tilde{O} contribution by all the upstream sections. The vortex strength should this increase along the swept (yawed) edge. This effect implies strength growing inboard in the case of the 240 degree (forward swept) case and towards the tip in the 300 degree (backward-swept) case.

In [2] we showed the following points about the nature of the flow field around a rotor blade in the reverse flow region.

1. The reverse-flow rotor blade encounters a significantly different onset velocity field compared to a fixed, yawed wing.
2. There is a systematic difference in dynamic pressure of the inset flow from root to tip, the root encountering the highest reverse flow speed.
3. At 240 degrees azimuth, a strong vortex is generated along the sharp edge, and grows in the inboard direction.
4. The increase in vortex strength directed inboard is due both to the yaw effect, where a helical vortex grows along the edge, and due to the linear increase in onset velocity moving inboard.
5. The radial velocity is directed towards the hub due to the helical vortex and due to the favorable pressure gradient at the surface along the inward radial direction.
6. At 270 degrees azimuth, the vortices seen are those generated at azimuths ahead of 270. The vortex is detached from the blade and is convecting along with the blade. The core shows the effects of a burst vortex.
7. At 300 degrees azimuth, the vortex structure looks similar to that at 270 degrees.
8. From the above, a consistent model of the blade aerodynamics may be developed, based on vortex-flow concepts adapted from delta wings at angle of attack.
9. Models based on 2-D airfoil aerodynamics and steady or unsteady shedding, do not usefully capture the physics of the reverse-flow rotor problem.
10. Static pressure contours in the flow field show the low-pressure region developed close to the surface by vortex interaction, resulting in vortex lift.
11. Static pressure contours on the blade surface at 270 degrees and beyond, show the vortex convected onto the blade, with minimum pressure occurring $0.15c$ from the sharp edge ($0.85c$ from the blunt edge). This supports the model of the vortex detaching from the edge as yaw becomes small, bursting, and having the core edge flow come close to the blade surface.

In continuing work, we explore the static pressure field.

1. The pressure field computed from the velocity field assuming constant stagnation pressure, shows why there is an inboard-directed radial flow at 270 and 300 degrees azimuth.
2. The effect of shear stress on the pressure loss is estimated along a few streamlines. This shows that the static pressure losses are dominant in vortex influence region
3. Accordingly the pressure gradient along the blade surface is slightly lower than the constant stagnation pressure case.
4. Pressure losses that are influenced by shear stress near to vortex is significantly low, thus validating the application of Bernoulli equation for nearly constant stagnation pressure.

4.4 Surface Pressure Contours

SPIV data at 5 radial locations starting from root r/R 0.4 to near tip r/R 0.7 were subjected to an interpolation to satisfy the differential mass conservation equation, and the results were interpolated using a cubic spline. The correspondence with the continuity equation is worst near the vortex core. Figure 2.2(b) shows the orientation. Color bars in Figure 4.11 denote the pressure coefficient C_p normalized by freestream dynamic pressure. The term "LE" refers to the blunt edge of the blade. Near the tip (r/R above 0.85), there is flow acceleration ahead of the sharp edge, with some suction for the first 10% of chord from the sharp edge (the relative velocity is lowest at the tip). Strongly negative C_p at the root is explained by the higher relative reverse speed. This pressure gradient negates centrifugal effects. As μ increases from 0.7 to 1.0, this root to tip pressure gradient rises.

Figure 4.12 shows the situation at 270 degrees azimuth. The blade is perpendicular to the flow, but moving rapidly and with a linear variation of onset velocity from root to tip. History effects must be considered. The very strong negative C_p regions occurring upstream of the sharp edge clearly indicate that a strong vortex is convecting from upstream of the blade rather than being caused by any 'shedding' from the blade as 2D models might predict. The negative C_p near TE at r/R 0.4-0.45 raises the possibility of flow separation or a secondary vortex being formed. The negative C_p observed further downstream is certainly due to a vortex convecting with the rotor. At azimuth 300, (Figure 4.13) the blade in reverse flow behaves like a backward swept wing. Pressure contours show evidence of the vortex at lower r/R . At μ of 1.0 the vortex appears to have convected further downstream and left the image frame. The

upstream flow is inclined towards the tip of rotor, while in the reverse flow region, flow moves towards the root based on the pressure gradient. Being generated from the velocity fields obtained at a few discrete radial stations, these plots are still jagged.

4.5 Vortex core profile

To get beyond slender wing theory at small angle of attack, the effect of flow detachment into first an attached vortex and then a detached vortex, must be considered. The velocity profile across the vortex was measured as shown in Figure 4.14 at 270 degrees azimuth, a clearly 'nonlinear' case in aerodynamics where the vortex core center is significantly away from the surface. The result shows the signature of a burst vortex: the solid-body core profile extends over the full diameter of the vortical flow.

4.6 Blunt Edge Flowfield

At the final stage of the project, we completed SPIV data acquisition around the blunt edge of the blade at 240 and 270 degrees. The results are qualitatively in Figure 4.15 and presented below in Figure 4.16. The phase-resolved, ensemble-averaged flowfield at $r/R = 0.5$ at 240 degrees azimuth is not massively separated. It in fact shows the streamline deflecting upwards around the blunt edge, resulting in a net upward flow turning angle. This is in accordance with expectations, showing a negative lift at this azimuth and r/R location. There was considerable cycle-to-cycle difference in the blunt edge flowfield, and some images did show separation or downward-tilting streamlines. Thus a large fluctuating lift and drag load is expected due to the nature of the flow around the blunt edge. At 270 degrees net streamline curvature is downward, suggesting positive lift generation. Again there was some cycle-to-cycle uncertainty. In all cases there was strong but fluctuating radial flow in the very near wake, showing that the flowfield around the blunt edge is highly 3-D and vortical. Some of this is to be expected. The radial flow is outward everywhere other than in the SEV zone.

4.7 Aspect Ratio Effects

The aspect ratio of the blade used here is small by helicopter rotor standards. It is only 3.49 for the hard-surfaced blade itself, though with root cut-out and hub diameter and the opposite side included, the aspect ratio in airplane terms is well above 8. Still, values for flying helicopters are on the order of 40 or more. How well do the results here capture expected phenomena in full-scale flight? A thought experiment is in order. The wind tunnel used here is large by most standards: a 2.74m test section width being the relevant dimension. The rotor diameter is constrained by wall effect avoidance. The chord Reynolds number of the experiment is low, but not hugely lower than flight conditions because in reverse flow, at least one section of the blade goes through zero relative velocity. So the vortex structures seen here are not very unrepresentative of flight conditions. The full-flight vortex is expected to be significantly tighter and stronger because of higher flow velocities, and hence perhaps occupy less of the chord than is seen in our experiments.

The thought experiment is to increase the aspect ratio of the present experimental blade by simply using a smaller-chord blade. What might happen? The vortex generation process is not expected to change significantly, since it occurs at the sharp edge. The fact that the blunt edge is encountered quicker, will be mitigated by the tighter vortex if we run at flight conditions. So in net effect, the results seen will not be significantly different. Multiple bursts and regeneration of the SEV may occur, but this is not seen on large delta wings which have very long leading edges. So, in net effect, the vortex should not be very different. Nor should the conclusions about surface pressure gradients. Nor about the 3-D flow around the blunt edge.

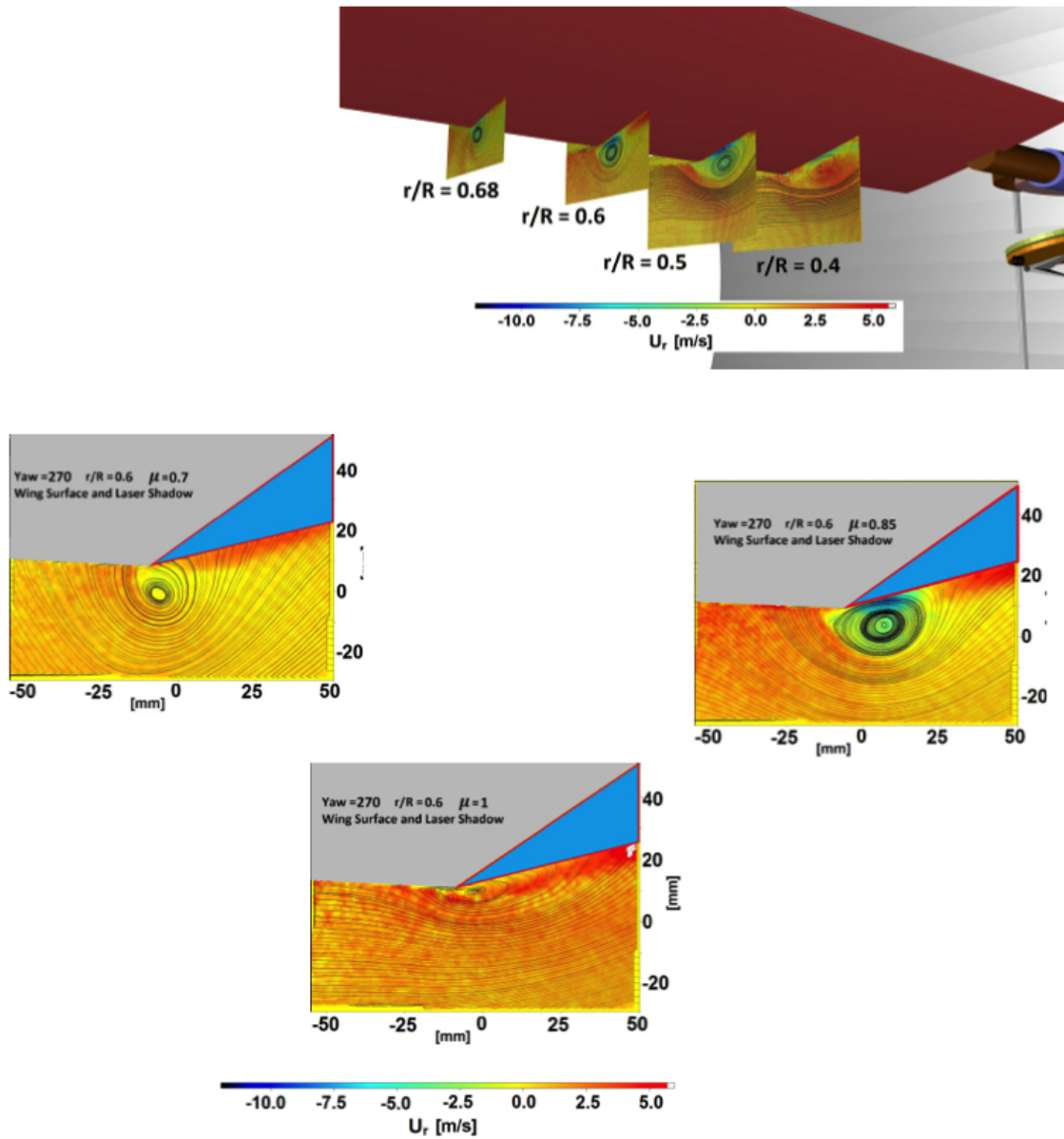


Figure 4.4: Streamline plots at r/R of 0.6 at $\psi = 270$ and $\mu = 0.85$.

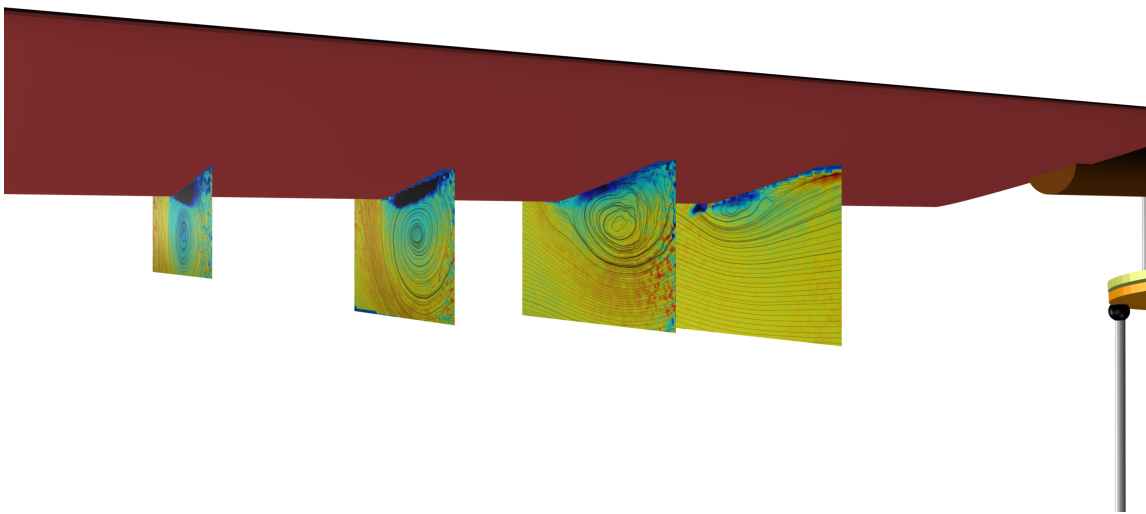


Figure 4.5: Streamline plots from SPIV near the sharp edge of the blade at different r/R at $\psi = 300$ and $\mu = 0.85$.

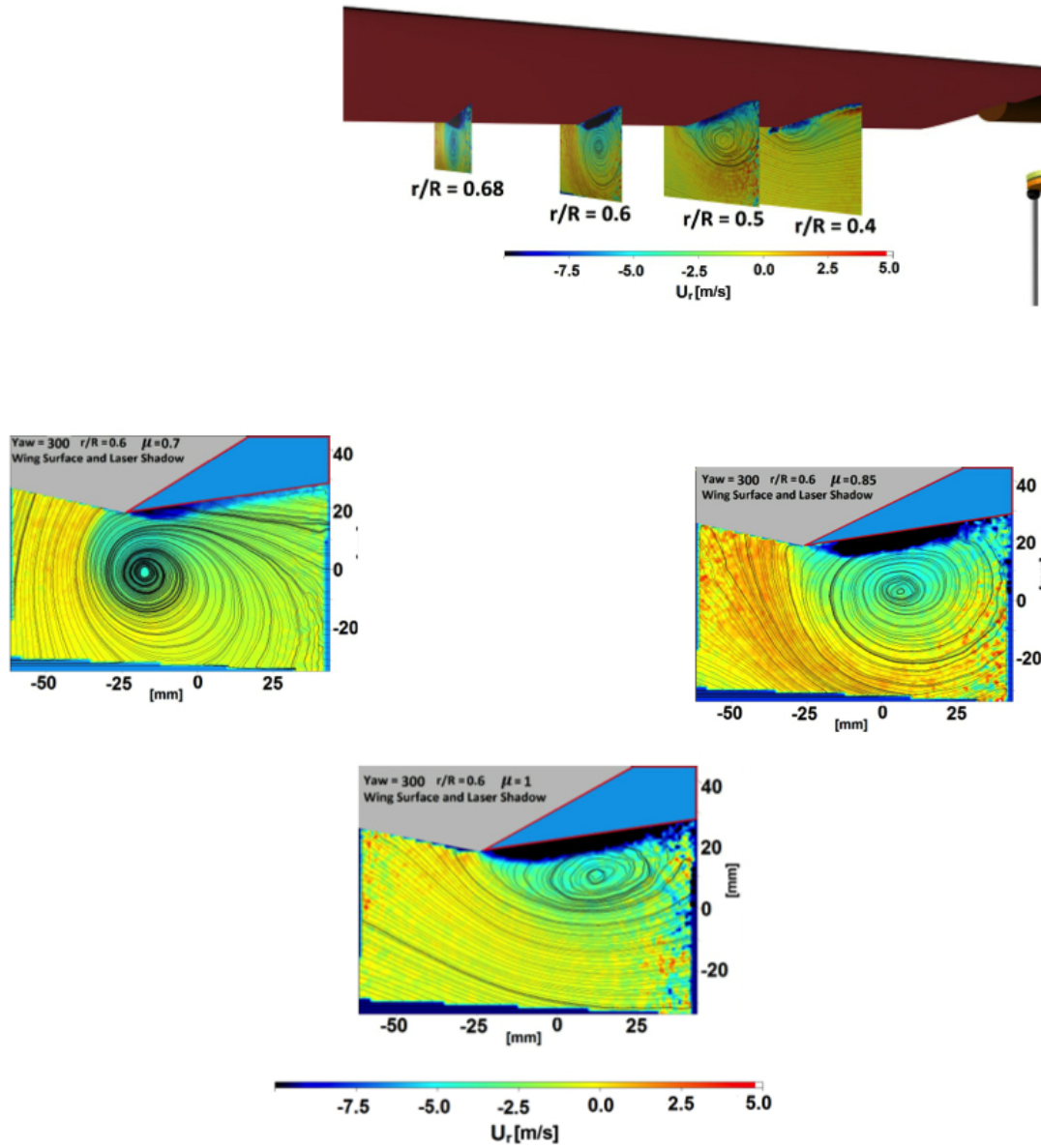


Figure 4.6: Streamline plots at r/R of 0.6 at $\psi = 300$ and $\mu = 0.85$.

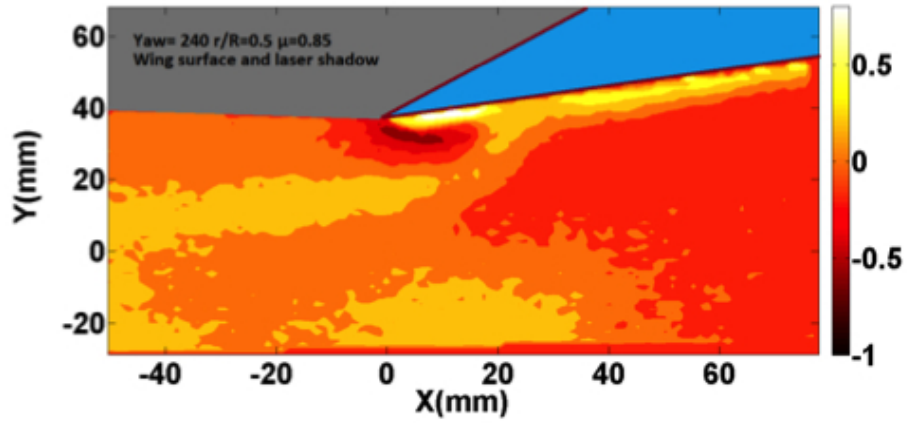


Figure 4.7: Contours of static pressure coefficient in the flow field generated from the SPIV data by assuming constant stagnation pressure. Azimuth 240, $r/R=0.5$, $t_t=0.85$

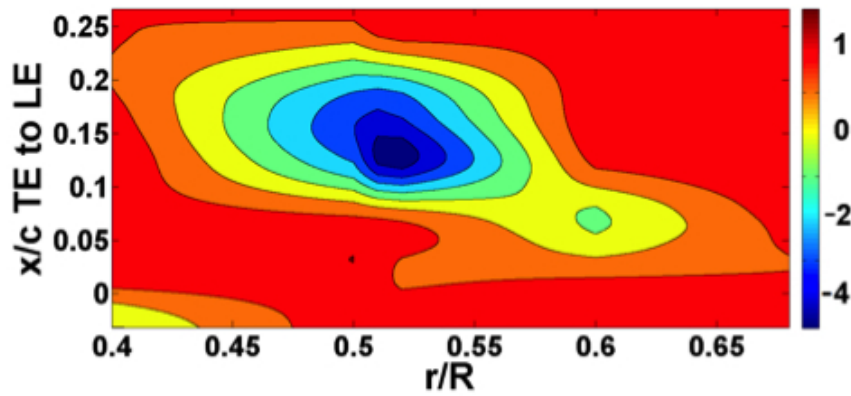


Figure 4.8: Contours of static pressure coefficient on the blade generated from the SPIV data by assuming constant stagnation pressure. Azimuth 270, $t_t=0.85$

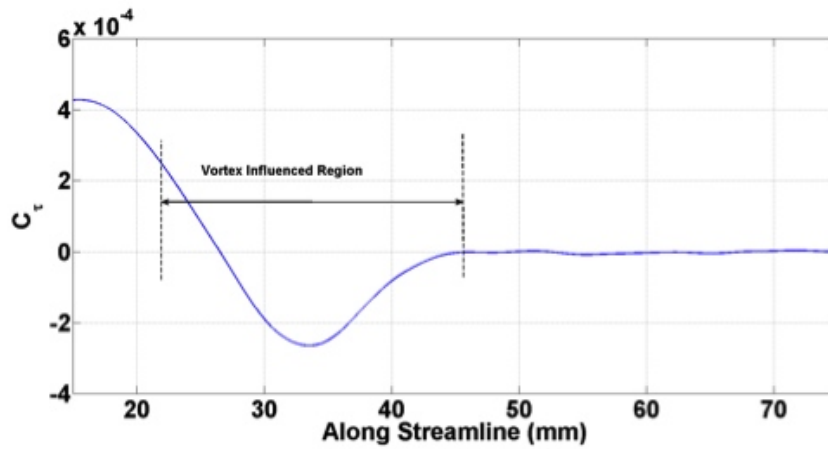


Figure 4.9: Viscous shear stress coefficient along a streamline through the sharp-edge vortex, as a measure of the loss in stagnation pressure.

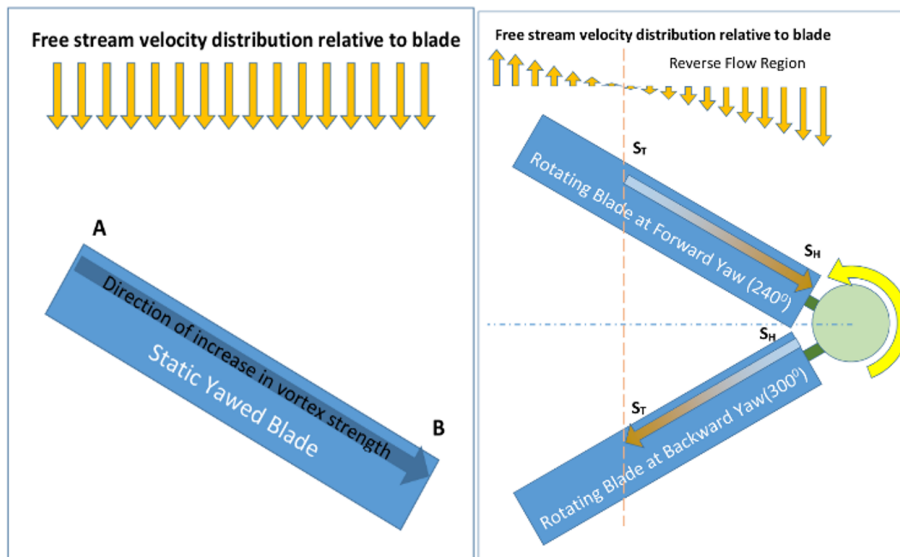


Figure 4.10: Various models for reversed flow on rotor blades.

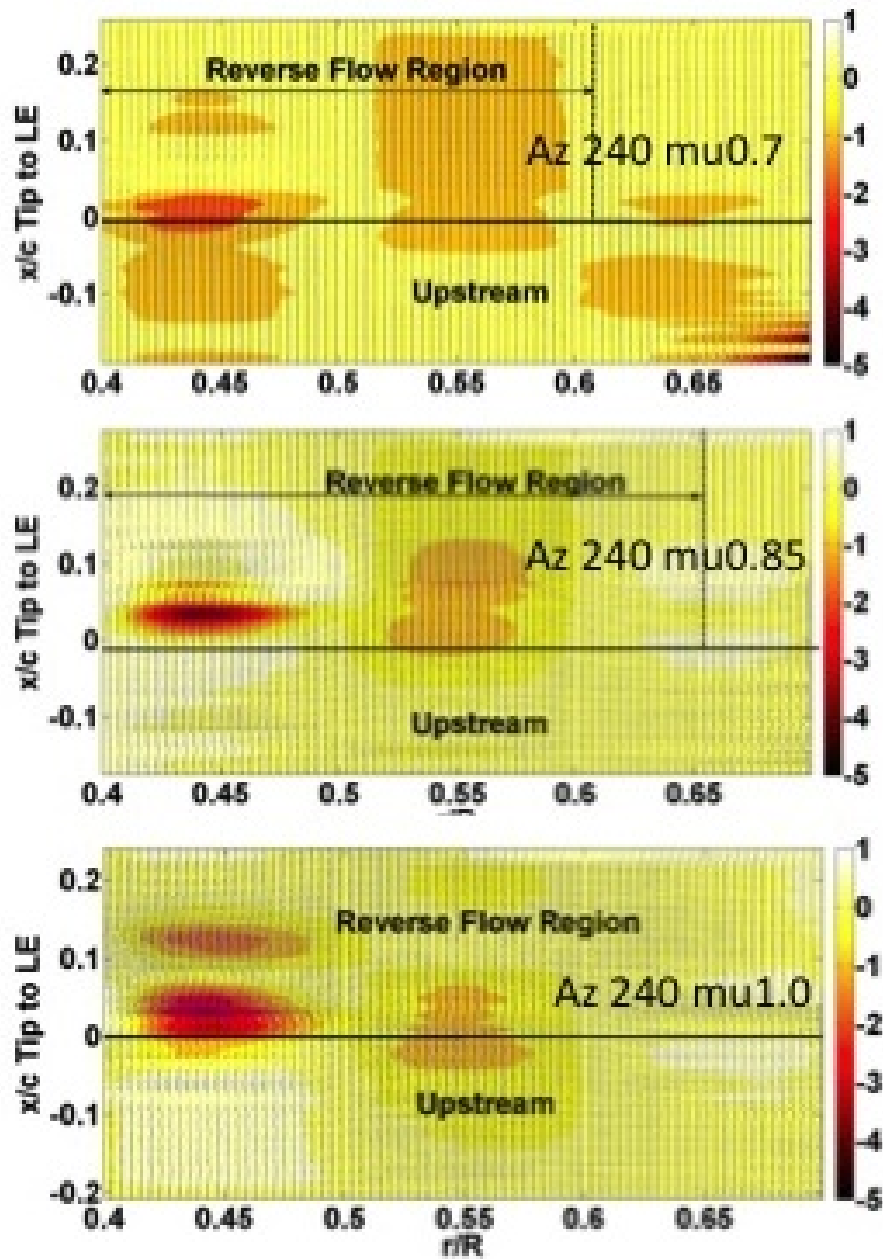


Figure 4.11: Static pressure contours obtained from the interpolated velocity field, at $\psi = 240$ for different advance ratios

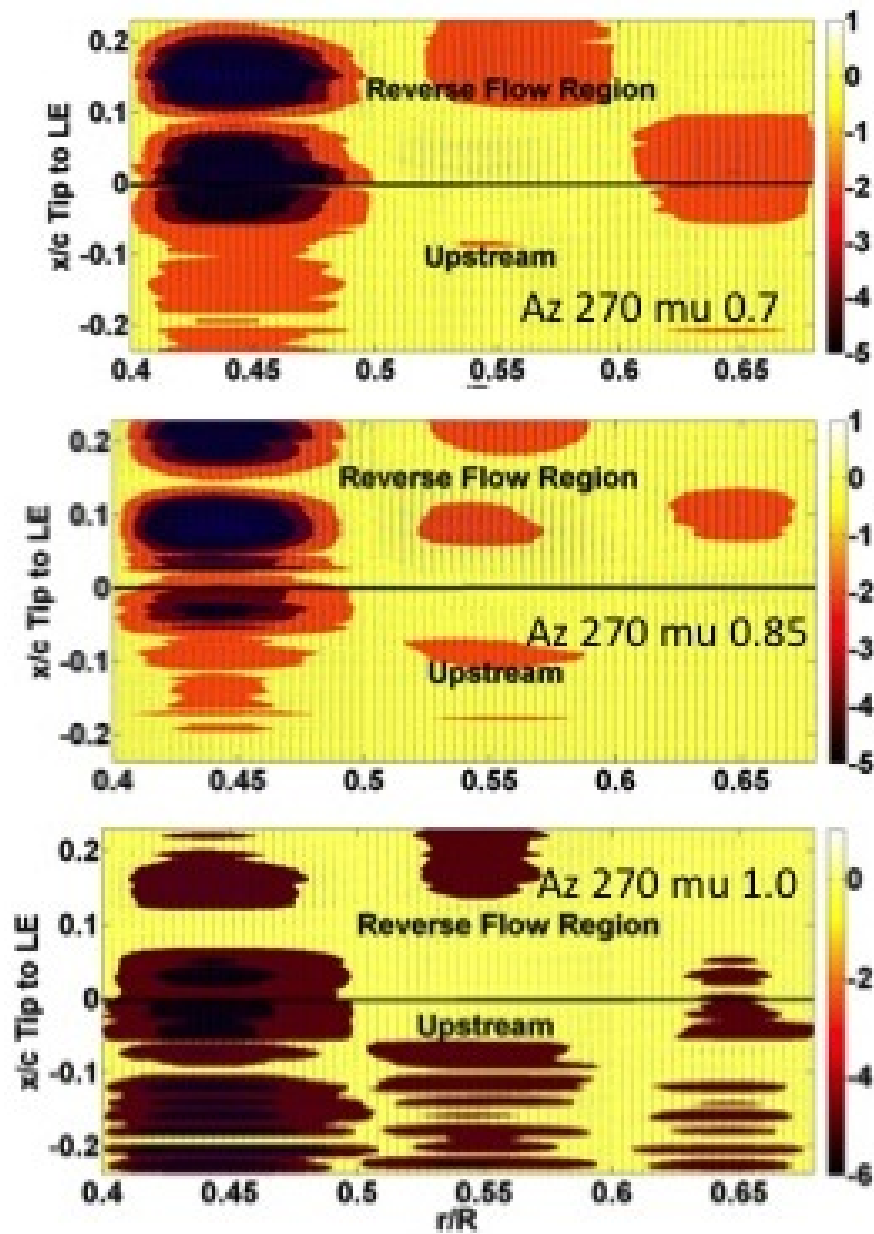


Figure 4.12: Static pressure contours obtained from the interpolated velocity field, at $\psi = 270$ for different advance ratios

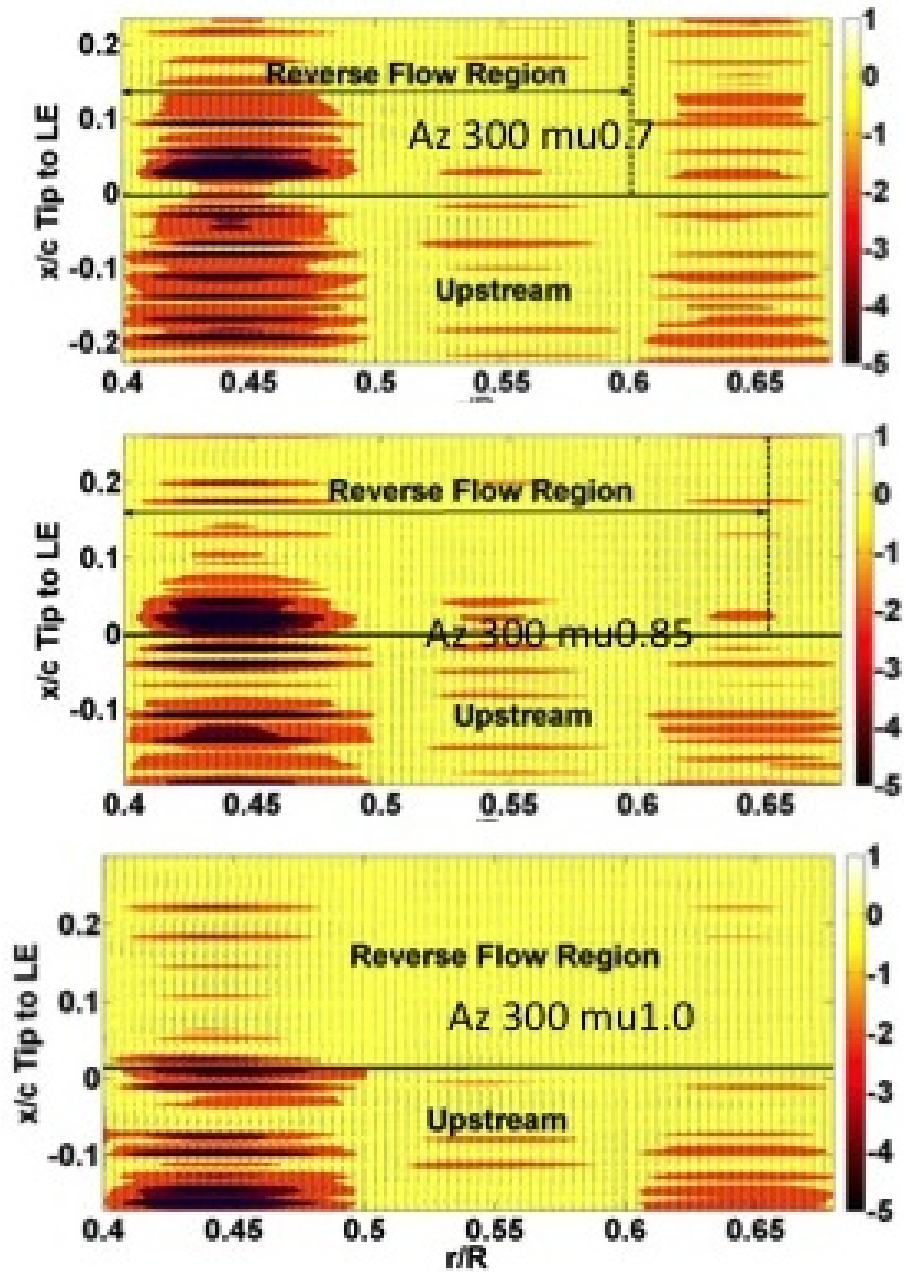


Figure 4.13: Static pressure contours obtained from the interpolated velocity field, at $\psi = 300$ for different advance ratios

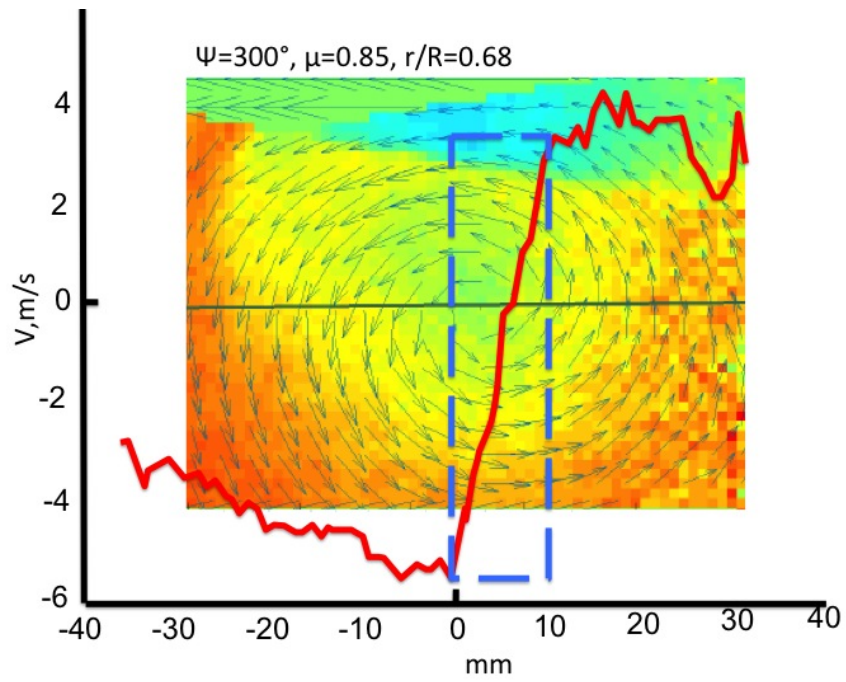


Figure 4.14: Velocity profile across the vortex at Azimuth 270

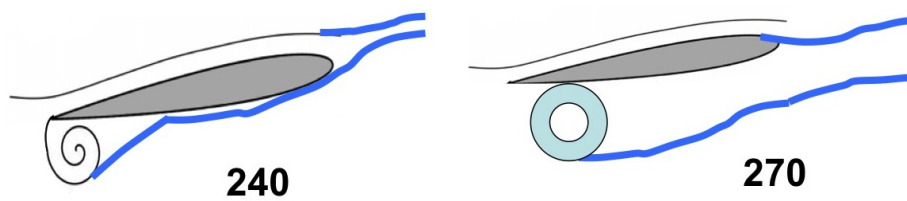


Figure 4.15: Flow Behavior Around the Blunt Edge. Qualitative pictures from initial SPIV data

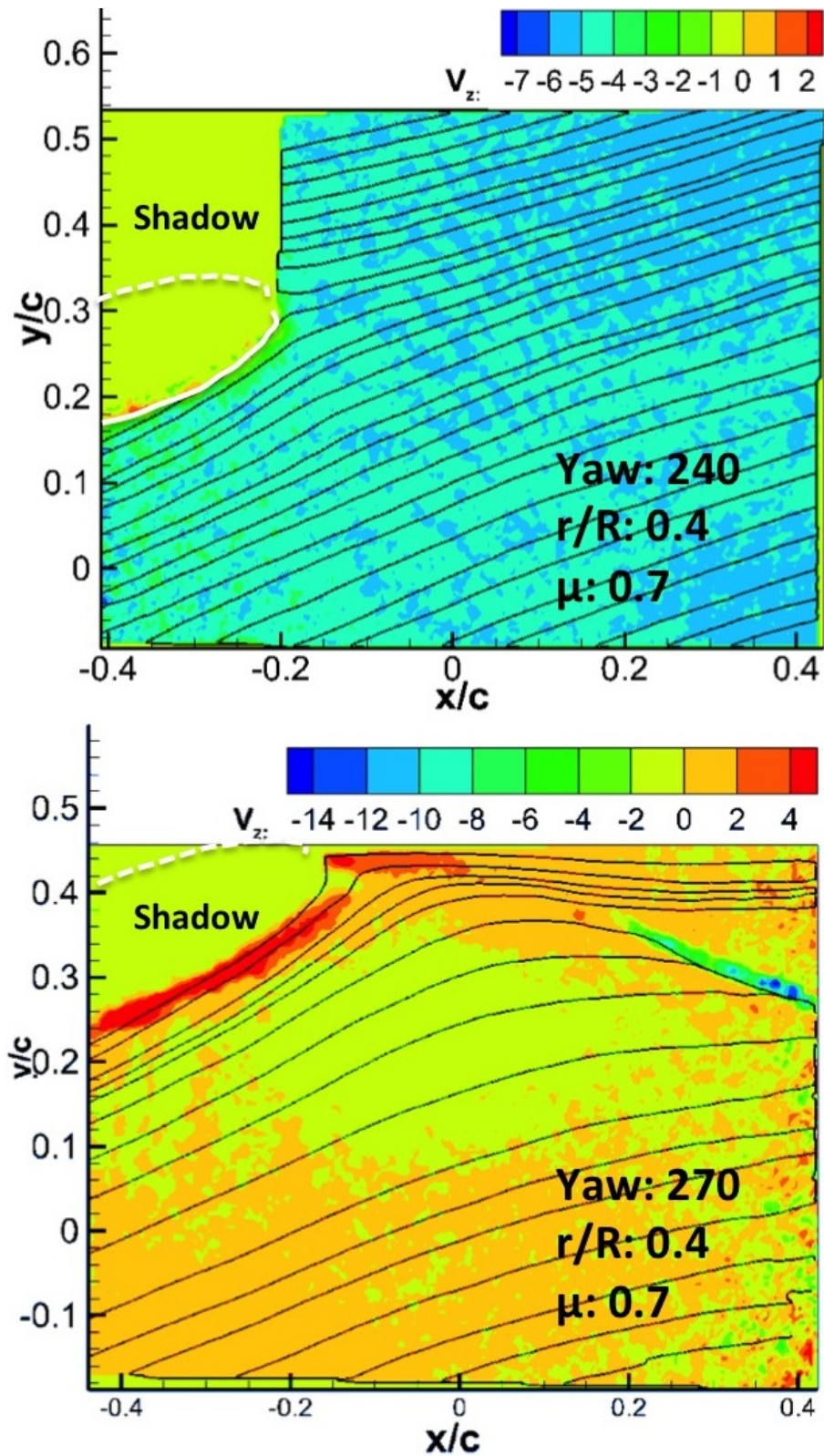


Figure 4.16: Streaklines and radial velocity contours at the Blunt Edge, for $r/R=0.4$, at $\mu = 0.7$ at 240 and 270 deg.

Chapter 5

Conclusions

Below we integrate the findings on the aerodynamics of rotor blades in reversed flow:

1. At high yaw, a fixed wing at angle of attack in reverse flow develops a vortex on the sharp edge.
2. The variation of lift and pitching moment with angle of attack shows substantial vortex lift effect.
3. The lift and pitching moment variation are better-predicted using the Polhamus leading edge suction analogy which allows accounting of the vortex flow effect.
4. Surface tuft behavior shows vortex bursting near the blade root for the forward-yaw reverse flow cases.
5. In the case of a rotating blade, since the blade is usually pitched up on the retreating side, the leeward side in reverse flow is the bottom side of the sharp edge. This is where the sharp edge vortex forms.
6. At 240 degrees azimuth, a strong SEV is seen to grow in the inboard direction.
7. The inboard rise in vortex strength is due both to SEV growth, and linear increase in onset velocity.
8. Between 240 and 270 degrees, the SEV bursts and detaches from the surface as the yaw decreases.
9. The vortex seen at 270 degrees azimuth is generated earlier, detached and convects with the blade.

10. The vortex structure at 300 deg is similar to that at 270 deg.
11. Static pressure contours in the flow field show a low-pressure region close to the surface by vortex interaction, resulting in vortex lift.
12. Vortex velocity profiles at 270 and 300 degrees show an expanded, solid-body-rotation core occupying most of the vortex region under the blade.
13. Surface pressure contours at 270 and beyond, show the minimum pressure occurring 0.15c from the sharp edge.
14. The pressure field computed from the velocity field explains inward radial flow at 270 and 300 deg.
15. Radial flow is outward except in the SEV zone.
16. The flow around the blunt edge is highly 3-D and mostly attached. At 240 deg. streamline curvature shows negative lift generation at $r/R = 0.5$, whereas at 270 deg. and $r/R = 0.5$, there is upward mean lift.
17. There is cycle-to-cycle intermittency in the blunt edge flow, but no evidence of periodic separation.

Bibliography

- [1] Mayo, M., Raghav, V., and Komerath, N., 2015. “Vortex flow hypothesis for a yawed rotor blade in reverse flow”. Proceedings of the Institution of Mechanical Engineers, Part G: Journal of Aerospace Engineering, **229**(3), pp. 543–553.
- [2] Hiremath, N., Shukla, D., Raghav, V., Pirau, S., and Komerath, N., 2015. “Effects of advance ratio and radial location on the vortex structure on a rotating blade in reverse flow”. In Proceedings of the American Helicopter Society Forum, 2015, AHS.
- [3] Raghav, V., and Komerath, N., 2013. “An exploration of radial flow on a rotating blade in retreating blade stall”. Journal of the American Helicopter Society, **58**(2), pp. 1–10.
- [4] Raghav, V., 2014. “Radial flow effects on a retreating rotor blade”. PhD thesis, Georgia Institute of Technology.
- [5] Walsh, D., Weiner, S., Arifian, K., Lawrence, T., Wilson, M., Millott, W., and Blackwell, R., 2011. “High airspeed testing of the sikorsky x2 technologytm demonstrator”. In American Helicopter Society 67th Annual Forum, Virginia Beach, VA.
- [6] Datta, A., Yeo, H., and Norman, T. R., 2013. “Experimental investigation and fundamental understanding of a full-scale slowed rotor at high advance ratios”. Journal of the American Helicopter Society, **58**(2), pp. 1–17.
- [7] Lind, A. H., Lefebvre, J. N., and Jones, A. R., 2013. “Experimental investigation of reverse flow over sharp and blunt trailing edge airfoils”. In AIAA 31st Applied Aerodynamics Conference, AIAA.
- [8] Ewans, J., and Krauss, T., 1973. Model wind tunnel tests of a reverse velocity rotor system. Tech. rep., DTIC Document.

- [9] Bagai, A., 2008. “Aerodynamic design of the x2 technology demonstrator main rotor blade”. In American Helicopter Society 64th Annual Forum, Montreal, Quebec, Canada.
- [10] Ruddell, A., Groth, W., and McCutcheon, R., 1981. Advancing blade concept (abc) technology demonstrator. Tech. rep., DTIC Document.
- [11] Knight, M., and Wenzinger, C. J., 1929. Wind-tunnel tests on a series of wing models through a large angle of attack range. part i: force tests. Report 317, NACA, Government Printing Office, Washington DC.
- [12] Critzos, C. C., Heyson, H. H., and Boswinkle, R. W., 1955. Aerodynamic Characteristics of NACA 0012 Airfoil Section at Angles of Attack from 0 to 180 Degrees. National Advisory Committee for Aeronautics.
- [13] Jacobs, E. N., and Sherman, A., 1937. Airfoil section characteristics as affected by variations of the Reynolds number. National Advisory Committee for Aeronautics.
- [14] Bradley, F. E., 1956. “An expression for rotor blade section loading including reversed flow effects”. Journal of the American Helicopter Society, **1**(4), pp. 32–33.
- [15] Wheatley, J. B., and Hood, M. J., 1936. Full-scale wind-tunnel tests of a pca-2 autogiro rotor. Tech. Rep. TR 515, NACA.
- [16] Charles, B. D., and Tanner, W. H., 1969. Wind tunnel investigation of semirigid full-scale rotors operating at high advance ratios. Tech. rep., DTIC Document.
- [17] MacCloud, J. L., Biggers, J. C., and Stroub, R. H., 1968. An Investigation of Full-Scale Helicopter Rotors at High Advance Ratios and Advancing Tip Mach Numbers. National Aeronautics and Space Administration.
- [18] Harris, F. D., 2008. Rotor performance at high advance ratio: theory versus test. CR 2008–215370, NASA, Ames Research Center, CA., October.
- [19] Quackenbush, T., Wachspress, D., McKillip Jr, R., and Sibia, M., 2011. “Aerodynamic studies of high advance ratio rotor systems”. In Proceedings of the American Helicopter Society Forum, 2011, AHS.
- [20] Potsdam, M., Datta, A., and Jayaraman, B., 2012. “Computational investigation and fundamental understanding of a slowed uh-60a rotor at high advance ratios”. In American Helicopter Society 68th Annual Forum, Fort Worth, TX.

- [21] Datta, A., Sitaraman, J., Chopra, I., and Baeder, J. D., 2006. “Cfd/csd prediction of rotor vibratory loads in high-speed flight”. Journal of aircraft, **43**(6), pp. 1698–1709.
- [22] Flax, A., 2012. “General reverse flow and variational theorems in lifting-surface theory”. Journal of the Aeronautical Sciences (Institute of the Aeronautical Sciences), **19**(6).
- [23] Niemiec, R., Jacobellis, G., and Gandhi, F., 2014. “Reversible airfoils for stopped rotors in high speed flight”. Smart Materials and Structures, **23**(11), p. 115013.
- [24] Carter, J., and Roncz, J., 2001. Airfoil suitable for forward and reverse flow, June 8. US Patent App. 09/877,268.
- [25] Meyer Jr, J. R., and Falabella Jr, G., 1953. An investigation of the experimental aerodynamic loading on a model helicopter rotor blade. Tech. rep., DTIC Document.
- [26] Sweet, G. E., Jenkins, J. L., and Winston, M. M., 1964. Wind-Tunnel Measurements on a Lifting Rotor at High Thrust Coefficients and High Tip-Speed Ratios. National Aeronautics and Space Administration.
- [27] Hislop, G. S., 1958. The Fairey Rotodyne. Fairey Aviation Company.
- [28] Wheatley, J. B., 1936. A study of autogiro rotor-blade oscillations in the plane of the rotor disk. Technical Note 581, NACA.
- [29] Landgrebe, A. J., Moffitt, R. C., and Clark, D. R., 1977. “Aerodynamic technology for advanced rotorcraft—part ii”. Journal of the American Helicopter Society, **22**(3), pp. 2–9.
- [30] Floros, M. W., and Johnson, W., 2009. “Performance analysis of the slowed-rotor compound helicopter configuration”. Journal of the American Helicopter Society, **54**(2).
- [31] Newman, S., 1997. “The compound helicopter configuration and the helicopter speed trap”. Aircraft Engineering and Aerospace Technology, **69**(5), pp. 407–413.
- [32] Warwick, G., 2005. “Groen brothers starts work on high-speed vtol heliplane for darpa”. Flight International, **168**(5015), p. 4.

- [33] Harris, F. D., Tarzanin, F. J., and Fisher, R. K., 1970. “Rotor high speed performance, theory vs. test”. Journal of the American Helicopter Society, **15**(3), pp. 35–44.
- [34] Bagai, A., 2008. “Aerodynamic design of the x2 technology demonstrator main rotor blade”. In American Helicopter Society 64th Annual Forum, Montreal, Quebec, Canada.
- [35] Kottapalli, S., 2012. “Performance and loads correlation of a uh-60a slowed rotor at high advance ratios”. In Proceedings of the American Helicopter Society Future Vertical Lift Aircraft Design Conference.
- [36] Yeo, H., 2012. “Investigation of uh-60a rotor performance and loads at high advance ratios”. Journal of Aircraft, **50**(2), pp. 576–589.
- [37] Polhamus, E. C., 1966. A concept of the vortex lift of sharp-edge delta wings based on a leading-edge-suction analogy. Technical Note TN D-3767, NASA, Langley Research Center, December.
- [38] Polhamus, E. C., 1971. “Predictions of vortex-lift characteristics by a leading-edge suctionanalogy”. Journal of aircraft, **8**(4), pp. 193–199.
- [39] Katz, J., and Plotkin, A., 2001. Low-speed aerodynamics, Vol. 13. Cambridge University Press.
- [40] Jones, R. T., 1946. Properties of low-aspect-ratio pointed wings at speeds below and above the speed of sound. Tech. rep., National Advisory Committee for Aeronautics.
- [41] Lozano, R., Raghav, V., and Komerath, N., 2012. “Aerodynamics of a yawed blade in reverse flow”. In Proceedings of ASME 2012 International Mechanical Engineering Congress Exposition.
- [42] Raghav, V., Mayo, M., Lozano, R., and Komerath, N., 2014. “Evidence of vortex-induced lift on a yawed wing in reverse flow”. Proceedings of the Institution of Mechanical Engineers, Part G: Journal of Aerospace Engineering, **228**(11), pp. 2130–2137.
- [43] Raghav, V., and Komerath, N., 2014. “Velocity measurements on a retreating blade in dynamic stall”. Experiments in Fluids, **55**(2), pp. 1–10.

- [44] Shukla, D., Hiremath, N., Raghav, V., and Komerath, N., 2015. “Dynamic effects in the reverse flow velocity field”. In Proceedings of the ASME-JSME-KSME Joint Fluids Engineering Conference 2015, no. 13545 in AJK2015.
- [45] Shevell, R. S., 1989. Fundamentals of flight, 2nd ed. No. 978-0133390605 in ISBN-13:. Prentice-Hall.
- [46] Johnson, W., 2012. Helicopter theory. Courier Dover Publications.
- [47] Bartlett, G. E., 1955. “Experimental investigation of influence of edge shape on the aerodynamic characteristics of low aspect ratio wings at low speeds”. Journal of the Aeronautical Sciences (Institute of the Aeronautical Sciences), **22**(8), pp. 517–533.
- [48] Lee, M., and Ho, C., 1990. “Lift force of delta wings”. Applied Mechanics Reviews;(United States), **43**(9).
- [49] Campbell, J. F., 1976. “Augmentation of vortex lift by spanwise blowing”. Journal of Aircraft, **13**(9), pp. 727–732.
- [50] Anderson, J. D., 2001. Fundamentals of aerodynamics, Vol. 2. McGraw-Hill New York.
- [51] Batchelor, G. K., 2000. An introduction to fluid dynamics. Cambridge university press.
- [52] Merkl, J., Hiremath, N., Raghav, V., and Komerath, N., 2015. “Extracting static pressure from velocimetry in vortical flows”. In Proceedings of the ASME-JSME-KSME Joint Fluids Engineering Conference 2015 AJK2015-FED, no. 20544 in AJK2015.

Index

- 0.85 advance ratio, 61
- 3-D flow, 69
- 6-DOF load, 18
- 70 percent radius, 61

- acceleration, 67
- advance ratio, 19
- adverse pressure gradient, 35
- aerosol , 20
- airfoil contour, 28
- angle of attack,, 19
- annihilation, 40
- aspect ratio, 19, 69
- attached flow, 36
- attached vortex, 25
- Azimuth 240, 61

- backward swept wing, 67
- backward- yaw, 63
- Barotron pressure transducer, 27
- barotropic, 39
- Bernoulli equation, 64
- beveled edge, 29
- blade lift, 1
- blade root, 35, 36
- blade section, 23
- blade-fixed coordinates, 23
- Blunt Edge Flowfield, 68
- bound circulation, 46
- burst, 65

- calibration matrix, 19

- camera image, 21
- CCD sensor, 43
- center of pressure, 31, 32
- centrifugal effects, 67
- centrifugal forces, 46
- chaotic motion, 33
- chordwise center of pressure movement, 25

- collective pitch, 19
- conical rotation, 33
- convecting, 62
- cosine fit, 29
- Couette flow, 64
- cross-flow equivalence, 28
- curve fit , 23
- cycle-to-cycle difference, 68

- DaVis, 21
- delta wing, 25
- digital protractor, 42
- discrete vortical shear layer structures, 1
- double-cavity, 20
- double-pulses, 20
- Drag polars, 25
- drag polars, 30
- dynamic lift, 1
- Dynamic pressure, 27
- dynamic stall, 1
- dynamic stall research, 26

- early separation, 29
- effective leading edge, 32, 46

- effective trailing edge, 32, 35
- everse-chord dynamic stall, 35
- favorable gradient, 63
- filtered voltage, 19
- flow topology, 35
- forward swept, 61
- forward yaw, 61
- Global velocity field, 37
- helical sharp-edged vortex, 65
- high aspect ratio, 30
- high torque, 19
- hypothesis, 25
- inception of stall, 2
- incompressible, 39
- individual errors, 28
- integrating effect, 65
- interpolation, 64
- interrogation pass, 21
- interrogation window , 21
- John Harper wind tunnel , 18
- Karman vortex street, 65
- laminar , 36
- Langley , 28
- laser balance, 42
- laser sheet, 60
- Laskin-nozzle, 20
- lateral tilt, 23
- LaVision, 20
- leading edge, 33
- lift , 25
- lift curve slope, 29
- lift curve slopes, 25, 29
- linear region, 31
- load cell, 25
- Load cell measurements , 25
- longitudinal cyclic, 19
- longitudinal tilt , 23
- low pass digital filter, 19
- low-turbulence tunnel, 28
- lower surface vortex, 35
- matte black paint, 20
- measurement error, 23
- measurement window, 21
- median filter, 21, 44
- momentum deficit, 33
- motion controller, 19
- mount obstruction, 36
- NACA 0013, 19
- NACA0013, 28
- Nd:YAG laser, 20, 42
- normal aerodynamic force, 31
- optical axes , 21
- Oswald's efficiency factor, 26
- out-of-plane velocity, 60
- Particle image velocimetry, 18
- particle size, 21
- phase locked PIV, 44
- phase locked SPIV, 19
- phase-shifted, 23
- pitch rate, 1, 35
- pitching moment, 1, 25, 31
- Pitot-static probe, 27
- PIV, 64
- pixel resolution, 20
- pixel size, 20
- Polhamus model, 25
- Polhamus suction analogy, 65
- Polhamus suction analogy , 30
- potential theory , 30
- predictive models, 64

- pressure contour , 21
- pressure gradient, 67
- Pressure losses, 64
- programmable timing unit, 43

- radial acceleration, 41
- radial flow, 1
- radial jet layer, 1
- radial locations, 19
- radial pressure gradient, 63
- radial stress, 1, 46
- reattachment, 2
- relative velocity, 18
- ressure coefficient, 64
- retreating blade side, 1
- Reynolds number, 26
- Reynolds numbers., 26
- right hand coordinate system, 60
- root structure, 19
- rotational effect, 26
- rotor, 18
- rounded edge, 29, 64

- scan rate, 43
- Seeding , 20
- separated flow, 33, 37
- setups, 18
- SEV, 69
- sharp trailing edge, 25
- sharp-edged delta wing, 25
- shear layer, 65
- Shevell's method, 26
- signal-to-noise ratio, 21
- sinusoidal fits, 23
- slender wing theory, 68
- span, 19
- span-wise vortex, 25, 35
- spatial cross-correlation, 21
- spatial resolution, 21

- spinning disk, 2
- SPIV, 60
- stall, 1
- stall , 26
- static stall, 1
- static yawed blade, 25
- static yawed wing, 26
- stepper motor, 19
- Stepper motors, 19
- stereo angle, 21
- stereo PIV, 18
- Stereoscopic-PIV instrumentation, 20
- streamline, 61
- streamline curvature, 68
- streamline plot, 62
- suction side, 32
- Surface scattering, 20
- Surface tuft flow visualization, 25

- tangential speed, 23
- teetering rotor, 19
- teetering rotor hub, 18
- Test matrix, 21
- tip vortex , 33
- total error, 28
- TPP, 23
- TPP orientation , 23
- tuft visualizations, 18
- tufts, 32
- tunnel speed, 27

- untwisted rectangular blade, 18, 19
- upward flow turning, 68

- vector magnitudes, 21
- vector smoothing, 44
- velocity field, 20
- velocity vectors, 21
- vertical velocity, 23

vortex breakdown, 35
vortex breakdown region, 35
vortex core, 61
vortex flow, 37
vortex lift, 30
vortex lift theory, 35
vortex shape, 62
vortex strength, 61, 65
vortex-induced lift, 25
vorticity, 65
Vorticity transport, 25

wake influence, 18
wind tunnel study, 25
worst case error, 28

yarn, 32